



Norwegian University of
Science and Technology

Closing the Gap between Reality and CFD Simulations of FFR with Techniques to Quantify and Reduce Uncertainty of Predictions

**Johannes Kløve Kjernlie
Hallvard Moian Nydal**

Master of Science in Mechanical Engineering
Submission date: June 2016
Supervisor: Leif Rune Hellevik, KT

Norwegian University of Science and Technology
Department of Structural Engineering

EPT-M-2016-95

MASTER THESIS
for
Students
Hallvard Moian Nydal & Johannes Kløve Kjernlie
Spring 2016

Closing the Gap between Reality and CFD Simulations of FFR with Techniques to Quantify and Reduce Uncertainty of Predictions

Forbedre numeriske strømningsberegninger for FFR ved bruk av metoder for å kquantifisere og redusere usikkerheten av prediksjoner

Background

Coronary artery disease (CAD) is one of the greatest challenges to global health. The gold standard for diagnosis of CAD is invasive coronary angiography. Annually about 30 000 invasive coronary angiographies are performed in Norway. This procedure inherits a minor although definite risk for the patient (myocardial infarction, stroke, access site bleeding). During the last years, CT coronary angiography (CTA), which is performed without catheterization, is the preferred method for patients with low to intermediate risk for significant coronary artery disease, and are also available at most district hospitals (e.g. Volda, Alesund). With a positive CTA, the patient will be investigated further by invasive procedures at one of the central hospitals (e.g. St. Olav Hospital, Trondheim). A challenge with CTA is the high number of false positives. This means that a significant number of patients will go through invasive coronary angiography, thus introducing unnecessary costs and medical risks for the patients.

Fractional flow reserve (FFR) is a catheterization technique used in the assessment of coronary artery disease during invasive coronary angiography, to measure pressure differences across a coronary artery stenosis (narrowing, usually due to atherosclerosis) to determine the likelihood that the stenosis impedes oxygen delivery to the heart muscle (myocardial ischemia). A method to estimate FFR from CTA would serve as a valuable tool to decrease the number of unnecessary invasive coronary angiographies.

The current method for estimating FFR from CTA involves using computational fluid dynamics. Despite its potential, estimation of FFR using computational fluid dynamics depends on accurate model parameters and boundary conditions, which are challenging to specify.

Objective

In this thesis, the primary objective is to analyze the effect of model parameters and boundary conditions for computational fluid dynamical estimation of FFR. Relevant model parameters and boundary conditions might include inflow/outflow, properties of blood and geometric properties.

The following tasks are to be considered:

1. Quantify uncertainty of estimated FFR from uncertainty in model parameters and boundary conditions.
2. Quantify sensitivity of estimated FFR from uncertainty in model parameters and boundary conditions.
3. Develop methods to detect and decrease uncertainty in FFR estimates.

-- " --

Within 14 days of receiving the written text on the master thesis, the candidate shall submit a research plan for his project to the department.

When the thesis is evaluated, emphasis is put on processing of the results, and that they are presented in tabular and/or graphic form in a clear manner, and that they are analyzed carefully.

The thesis should be formulated as a research report with summary both in English and Norwegian, conclusion, literature references, table of contents etc. During the preparation of the text, the candidate should make an effort to produce a well-structured and easily readable report. In order to ease the evaluation of the thesis, it is important that the cross-references are correct. In the making of the report, strong emphasis should be placed on both a thorough discussion of the results and an orderly presentation.

The candidate is requested to initiate and keep close contact with his/her academic supervisor(s) throughout the working period. The candidate must follow the rules and regulations of NTNU as well as passive directions given by the Department of Energy and Process Engineering.

Risk assessment of the candidate's work shall be carried out according to the department's procedures. The risk assessment must be documented and included as part of the final report. Events related to the candidate's work adversely affecting the health, safety or security, must be documented and included as part of the final report. If the documentation on risk assessment represents a large number of pages, the full version is to be submitted electronically to the supervisor and an excerpt is included in the report.

Pursuant to "Regulations concerning the supplementary provisions to the technology study program/Master of Science" at NTNU §20, the Department reserves the permission to utilize all the results and data for teaching and research purposes as well as in future publications.

The final report is to be submitted digitally in DAIM. An executive summary of the thesis including title, student's name, supervisor's name, year, department name, and NTNU's logo and name, shall be submitted to the department as a separate pdf file. Based on an agreement with the supervisor, the final report and other material and documents may be given to the supervisor in digital format.

- Work to be done in lab (Water power lab, Fluids engineering lab, Thermal engineering lab)
 Field work

Department of Energy and Process Engineering, 13. January 2016



Olav Bolland
Department Head



Leif Rune Hellevik
Academic Supervisor

Closing the Gap between Reality and CFD Simulations of FFR with Techniques to Quantify and Reduce Uncertainty of Predictions

ABSTRACT

Coronary artery disease has been reported the most common cause of death worldwide and is an ever-growing problem for global health. Recently, diagnosis of coronary artery disease from CT angiography (CTA) and computational fluid dynamics (CFD), CT_{FFR} , has emerged as a promising non-invasive alternative to the conventional clinical procedure. The aim of this thesis is to quantify and reduce the uncertainty of CT_{FFR} . In particular, we focus on uncertainties from the interaction between CFD and the coronary physiology. First, we use a lumped-element model to investigate the uncertainty and sensitivity of CT_{FFR} to physiological parameters. Second, we perform an in-depth investigation of the governing physiological model for flow distribution in CT_{FFR} simulations, Murray's law. Third, we propose a new model to reduce the inaccuracies from CTA-invisible coronary arteries. Our results show that uncertainty in physiological parameters has a significant effect on FFR estimates. Moreover, we find that CTA-invisible coronary arteries greatly increase the uncertainty of FFR, but that this effect can be reduced with improved mathematical modeling. Last, we find that CT_{FFR} is highly sensitive to post-stenotic flow outlets, which highlights the clinical importance of post-stenotic CTA image quality.

*Forbedre numeriske strømningsberegninger for FFR ved
bruk av metoder for å kvantifisere og redusere usikkerheten i
prediksjoner*

Sammendrag

Koronarsykdom er verdens farligste sykdom og et økende problem globalt. Den mest anerkjente metoden for diagnostisering av koronarsykdom er invasiv FFR, en metode som både er kostnadskrevende og har en liten men betydelig risiko for komplikasjoner. Estimering av FFR fra ikke-invasiv CT angiografi (CTA) og numerisk fluiddynamikk, CT_{FFR} , har utviklet seg til et spennende alternativ til den konvensjonelle fremgangsmåten. Målet med denne oppgaven er å kvantifisere og redusere usikkerhet i CT_{FFR} . Først undersøker vi usikkerhet og sensitivitet av CT_{FFR} til fysiologiske parametere. Deretter ser vi nærmere på den viktigste modellen for fordeling av blodstrøm i arteriene, Murrays lov. I tillegg undersøker vi effekten av arterier som er usynlige ved CTA og foreslår en ny metode for å redusere effekten av disse arteriene på CT_{FFR} . Resultatene våre viser at usikkerhet i fysiologiske modellparametere har en signifikant effekt på CT_{FFR} . Vi finner også at estimert FFR over stenosar er spesielt sensitiv til poststenotiske utløp i den fluiddynamiske modellen, noe som fremhever viktigheten av poststenotisk bildekvalitet. Til slutt finner vi at arterier som er usynlige ved CTA har en markant effekt på CTA, men at denne effekten kan reduseres ved nytenkende matematisk modellering.

Preface

This master thesis is written as part of a Master of Science degree in Mechanical Engineering at the Norwegian University of Science and Technology. The thesis was conducted throughout Spring 2016 at the Department of Energy and Process Engineering.

Here, we investigate how to close the gap between physiology and fluid dynamics for simulations of CT_{FFR} . The thesis builds on our project theses where we investigated the feasibility of computational fluid dynamics for estimation of FFR from CT angiography. During the project theses, we experienced that our simulations seemed very sensitive to physiologically governed input parameters and boundary conditions. Interestingly, to our knowledge, few studies have investigated this effect. Thus, we decided to dedicate our thesis to the cross-section between CFD and physiology, with an aim to quantify and reduce uncertainties in CT_{FFR} .

Johannes Kløve Kjernlie

Hallvard Moian Nydal

June 10, 2016

Acknowledgments

This project could not have been accomplished without the help of several people. We would like to thank our supervisor, Prof. Leif Rune Hellevik Ph.D., for guidance and letting us be a part of the group at the Division of Biomechanics.

Our thanks go to the Ph.D. candidates at the Divison of Biomechanics, Vinzenz G. Eck, Fredrik E. Fossan and Jacob T. Sturdy for being helpful and motivating.

Our thanks go to Prof. Rune Wiseth, M.D., Ph.D., Anders T. Bråten, M.D. and Arve Jørgensen, M.D., Ph.D. for being understanding and informative, concerning problems of clinical relevance.

Our thanks go to Kristian Valen-Sendstad, Ph.D. and Aslak Bergersen, for an introduction to the world of computational fluid mechanics for biomedical applications.

Our thanks go to our fellow biomechanics students, Daniel Morton, and Stig Marsteng Nilsen, for countless valuable discussions and a good atmosphere in the lab

Our final thanks go to all our family and friends, for being there for us.

Abbreviations

CAD	Coronary artery disease
CDF	Cumulative density function
CFD	Computational fluid dynamics
CT	Computed tomography
CTA	Computed tomography angiography
CT_{FFR}	Computational fractional flow reserve
CVD	Cardiovascular disease
CX	Circumflex
EE	Elementary effects
FFR	Fractional flow reserve
ICA	Invasive coronary angiography
iid	Independent and identically distributed
LAD	Left anterior descending
LVM	Leaky vessel model
MAP	Maximum a posteriori
MC	Monte Carlo
MFF	Myocardial flow fraction
PC	Polynomial Chaos
PDF	Probability density function
RCA	Right coronary artery
RF	Random forest
SA	Sensitivity analysis

TCRI Total coronary resistance index
UQ Uncertainty quantification

Nomenclature

α	Radius of inviscid core, Multi-indices
ε	Noise term
Λ	Split coefficient
μ	Dynamic viscosity, Mean
μ_X^*	Absolute value of mean
ρ	Density, Probability density function
σ	Standard deviation
Φ	Polynomial
Ω	State space
c	Murray's coefficient
d	Elementary effect
F	Cumulative distribution function
f	Black box functional
\mathbf{f}	Source term vector
G	Conductance
L	Length
p	Probability
P	Pressure
Q	Flow rate
R	Resistance
r	Radius, Hastings ratio
S	Sobol sensitivity indices

T	Rosenblatt transformation
\mathbf{u}	Velocity vector
$\binom{n}{k}$	Binomial coefficient indexed by n and k

Contents

1	INTRODUCTION	1
1.1	Coronary Artery Disease (CAD)	2
1.2	Diagnosis of Coronary Artery Disease	3
1.3	Non-Invasive Computational Estimation of FFR from CTA (CT_{FFR})	5
1.4	Thesis	7
2	CT_{FFR} MODEL	9
2.1	Background	10
2.2	CT_{FFR} Model	22
2.3	Summary	31
3	UNCERTAINTY QUANTIFICATION AND SENSITIVITY ANALYSIS	33
3.1	Background	36
3.2	Forward Uncertainty Analysis	42
3.3	Backward Uncertainty Analysis: Bayesian inference	60
3.4	Summary	66
4	APPLICATION OF UNCERTAINTY QUANTIFICATION AND SENSITIVITY ANALYSIS TO CT_{FFR}	67
4.1	Parameter Uncertainty in Single Stenosis	68
4.2	Effect of Uncertainty in Physiological Parameters on CT_{FFR}	75
4.3	Discussion	83

5	UNCERTAINTY IN CT_{FFR} FLOW DISTRIBUTION MODEL	85
5.1	Background	86
5.2	Regression Analysis	88
5.3	Backward Uncertainty Analysis	92
5.4	Discussion	100
6	INVISIBLE ARTERIES	103
6.1	Leaky Vessel Model (LVM)	104
6.2	Quantification of Flow to Invisible Branches	105
6.3	Effect of Invisible Branches on CT_{FFR}	108
6.4	Effect of Leaky Vessel Model on CT_{FFR}	110
6.5	Discussion	112
7	DISCUSSION	115
7.1	Summary	115
7.2	Suggestions for future work	117
	REFERENCES	136

Prediction is very difficult, especially if it's about the future.

Niels Bohr

1

Introduction

Cardiovascular diseases (CVDs) account for > 17 million deaths globally each year and is expected to grow to 23.6 million by 2030 [1]. Of this number, coronary artery disease (CAD) is the largest contributor to CVDs. In 2013, CAD was the most common cause of death globally, resulting in 8.14 million deaths worldwide [2]. In addition to the adverse implications for health, the epidemic of CVDs have a tremendous impact on the economy. In the US, direct medical costs of CVDs are projected to triple, from \$273 billion in 2010 to 818\$ billion in 2030 [3].

Recent advances in computational fluid dynamics (CFD) shows a clear potential to reduce costs and improve patient outcome for diagnosis of CAD [4]. Despite its tremendous potential, diagnosis of CAD from CFD requires an accurate description of the complex relationship between CFD and coronary physiology. In this thesis, we aim to quantify and reduce the uncertainties from

this relationship using the most influential CFD-based diagnostic tool for CAD, CT_{FFR} .

1.1 CORONARY ARTERY DISEASE (CAD)

Arteries that supply blood to the myocardium¹ are termed coronary arteries. The coronary arteries consist of two main branches, the right coronary artery (RCA) and the left coronary artery, which further divides into two branches, the left anterior descending (LAD) and the left circumflex branch (CX), as seen in Figure 1.1.1.

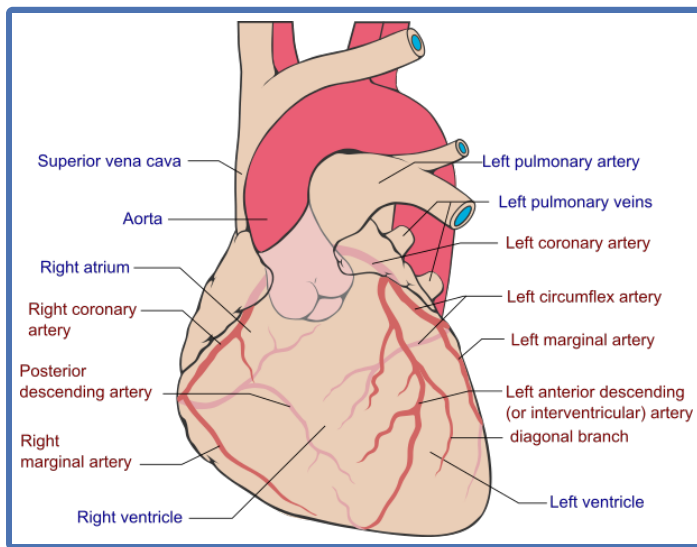


Figure 1.1.1: Anatomy of coronary arteries [5].

Common symptoms of CAD include chest pain, heartburn, and shortness of breath. The most frequent reason for CAD is atherosclerosis, a build-up of plaque in the arteries of the heart. The plaque, composed of calcium, fatty deposits, and inflammatory cells has a hardening and narrowing effect on the coronary arteries. This build-up of plaque in coronary arteries is critical for two reasons. First of all,

¹Myocardium: Muscle tissue of the heart.

the narrowing effect on vessel walls is a direct cause of reduced transport of oxygen-rich blood to the heart. Second, a build-up of plaque increases the chance of the formation of blood clots. These blood clots dramatically enhance the probability of a full or partial coronary block, introducing a major risk of myocardial infarction and death.

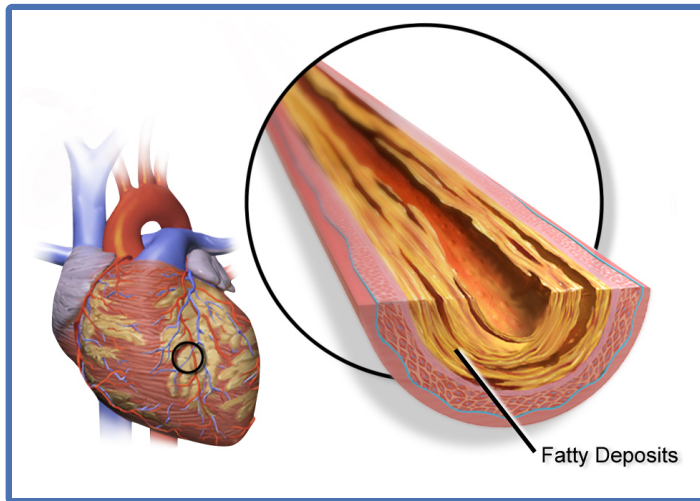


Figure 1.1.2: Atherosclerosis in coronary arteries [6].

1.2 DIAGNOSIS OF CORONARY ARTERY DISEASE

According to doctors at Trondheim University Hospital, the standard clinical route for diagnosis of CAD is an initial screening with non-invasive CT angiography (CTA), followed by invasive coronary angiography (ICA) [personal communication, 9/23, 2015]. In this process, CTA serves as a gateway screening to limit the number of patients that have to go through an ICA.

1.2.1 CORONARY COMPUTED TOMOGRAPHY ANGIOGRAPHY (CTA)

Coronary computed tomography angiography (CTA), is a noninvasive method for visualization of CAD. The method is non-invasive, cheap and offers excellent

negative predictive value ² for the absence of coronary artery disease [7]. Despite this, CTA has a low positive predictive value ³ and therefore results in a high number of false positives [8].

1.2.2 FRACTIONAL FLOW RESERVE (FFR)

FFR is defined as the maximum blood flow to the myocardium in the presence of a stenosis in the supplying coronary artery, divided by the theoretical normal maximum flow [9]. This ratio represents the hyperemic ⁴ flow with and without a single stenosis and can be derived from the ratio of mean distal coronary pressure (P_d) to mean aortic pressure (P_a) recorded simultaneously under conditions of maximum hyperemia. FFR during hyperemic flow can be expressed as

$$FFR = \frac{P_{distal} - P_v}{P_a - P_v} \quad (1.1)$$

where P_a is the mean aortic pressure, P_v is the central venous pressure and P_{distal} is the hyperemic coronary pressure proximal to the stenosis. Assuming a proximal lesion and negligible venous pressure, the equation simplifies to

$$FFR = \frac{P_a - \Delta P}{P_a} \quad (1.2)$$

where ΔP is the pressure gradient along the axis of vessel segment from proximal to distal positions of the stenosis. The full derivation of FFR over a single stenosis can be found in the work of Pijls et al. [10]

1.2.3 INVASIVE CORONARY ANGIOGRAPHY (ICA)

ICA is the gold standard for establishing the presence, location, and severity of CAD [11]. During an ICA, the hemodynamic significance metric of coronary

²Negative predictive value: Proportion of negative results in statistics that are true negative results.

³Positive predictive value: Proportion of positive results in statistics that are true positive results.

⁴Hyperemia: An excess of blood in the vessels supplying an organ or other parts of the body.

stenoses is FFR. To measure FFR, a pressure wire is used to determine the ratio of maximal coronary blood flow through a stenotic artery to the blood flow in the hypothetical case that the artery was normal. In the FAME (Fractional Flow Reserve Versus Angiography for Multivessel Evaluation) trial of 1,005 patients with multivessel coronary artery disease (CAD), FFR-guided revascularization⁵ (i.e., revascularization for lesions with FFR lower than 0.80) was associated with a 28 % lower rate of major adverse cardiac events compared with an angiography-guided strategy [12]. While ICA provides an excellent data for diagnosis and further interventions, the technique is invasive, costly and is associated with a small but definite risk of morbidity and mortality [13].

1.3 NON-INVASIVE COMPUTATIONAL ESTIMATION OF FFR FROM CTA (CT_{FFR})

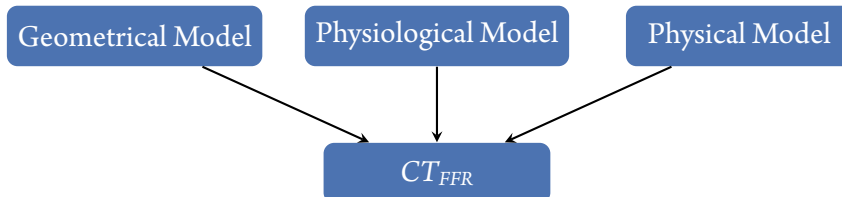


Figure 1.3.1: Computation of CT_{FFR} is a result of a complex interplay between a geometrical model, a physiological model and a physical model.

In the past, CFD for biomedical applications has been limited due to the high complexity of fluid flows in the human body. Today, the field is steadily growing as researchers and clinicians understand its potential and high-performance hardware and software is getting more available [14]. Recently, computational fluid mechanics has enabled estimation of FFR from CTA. The introduction of CFD-guided post-processing of CTA is called CT_{FFR} , and has shown tremendous potential in a number of larger clinical studies including PLATFORM

⁵Revascularization: restoration of the blood circulation of an organ or area.

(Prospective Longitudinal Trial of FFR_{CT} : Outcomes and Resource Impacts) [15], DeFACTO (Determination of Fractional Flow Reserve by Anatomic Computed Tomographic Angiography) [16] and DISCOVER-FLOW (Diagnosis of Ischemia-Causing Stenoses Obtained Via Noninvasive Fractional Flow Reserve) [17] studies.

Computation of CT_{FFR} is a result of an interplay between a CT-derived geometrical model of the coronary arteries, a physical model using a numerical solution of the laws of physics governing fluid dynamics and a physiological model for determination of pressure and flow boundary conditions.

1.3.1 CLINICAL ROUTE

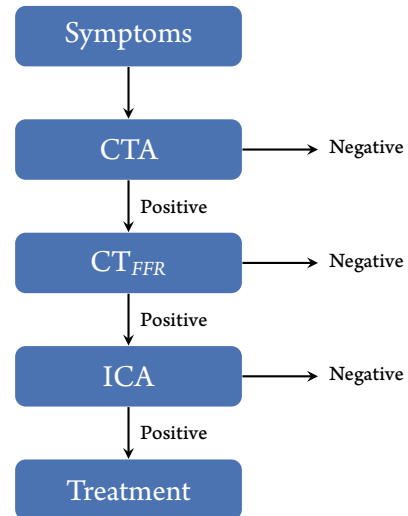


Figure 1.3.2: Clinical path with CT_{FFR} .

CT_{FFR} introduces a new clinical route that can be seen in Figure 1.3.2. This new clinical route has the potential to reduce the number of unnecessary ICA treatments dramatically, hereby reducing costs and medical risks. Currently, CT_{FFR} is receiving major interest, both in academia and industry.

1.4 THESIS

1.4.1 OBJECTIVE

The objective of this thesis is to quantify and reduce the uncertainty of CT_{FFR} with a particular focus on uncertainties from the interaction between CFD and the coronary physiology. In practice, we quantify uncertainty and sensitivity of CT_{FFR} with respect to physiological input parameters. Further, we perform an in-depth investigation of the governing physiological model for flow distribution in CT_{FFR} simulations, Murray's law. Last, we propose a model to reduce the inaccuracies from coronary vessels invisible to CTA.

1.4.2 RELATED WORK

To our knowledge, little work has been done to quantify the uncertainty and sensitivity of CT_{FFR} with respect to physiological input parameters. While some authors have investigated the effect of lumen segmentation on CT_{FFR} including the work by Sankaran et al. [18, 19], physiological parameters have received considerably less interest. The most notable exception is another work by Sankaran et al. [20] that quantified uncertainty and sensitivity of CT_{FFR} with respect to selected lumen segmentation and physiological parameters. Despite this, their work only included a small number of input variables and was restricted to a limited sensitivity analysis.

Numerous authors have investigated flow distribution in arterial networks [12, 17, 21–25]. The most prominent flow distribution model for vascular systems, Murray's law, has received tremendous attention in practical applications of CT_{FFR} [12, 26, 27]. Surprisingly, there has been limited interest in the uncertainty of Murray's law. To our knowledge, no work has investigated the effect of uncertainty in Murray's law on CT_{FFR} .

While the potential influence on invisible coronary arteries has been mentioned in literature [26], there has been remarkably low interest for the effect of CTA-invisible coronary arteries on CT_{FFR} . To our knowledge, this is the first

work that proposes a mathematical model aiming to reduce the effect of CTA-invisible coronary arteries on CT_{FFR} .

1.4.3 OUTLINE

This thesis is organized as follows. In Chapter 2, we perform an in-depth investigation of the theory of flow characteristics of coronary arteries and present a simplified model for CT_{FFR} . In Chapter 3, methods and governing theory for uncertainty quantification and sensitivity analysis is presented.

Uncertainty quantification and sensitivity analysis of the CT_{FFR} model is performed in Chapter 4. Based on this analysis, we do an in-depth investigation of the physiological parameters governing flow distribution in CT_{FFR} models in Chapter 5. Last, Chapter 6 introduces a new class of boundary conditions to model the effect of fluid loss to CTA-invisible coronary arteries, before we sum up our findings and direction for future work in Chapter 7.

1.4.4 LIMITATIONS

The aim of this thesis is to quantify and reduce the uncertainty of CT_{FFR} . Unfortunately, state-of-the-art algorithms for CT_{FFR} are computationally expensive and do not facilitate this type of analysis on a restricted computational budget. Thus, the results in this thesis are based on a simplified model of CT_{FFR} .

All models are wrong, but some are useful.

George E. P. Box

2

CT_{FFR} Model

Computation of CT_{FFR} is derived from an interaction between a geometrical model of the coronary arteries, a physical model for the fluid dynamics of coronary arteries and a physiological model for model parameters. In this chapter, we propose a simplified CT_{FFR} model to quantify uncertainty and investigate ways to reduce the uncertainty in CT_{FFR} models. We build our simplified model on principles from the most prominent works in the field of CT_{FFR} , including recently published work from the groups behind the two most important commercial players, Heartflow, Inc. and Siemens Healthcare [28].

Also, we present the coronary geometry dataset used for the experiments in this thesis. The dataset is based on published data from Kassab et al. [29] and is a result of the construction and analysis of a polymer cast of pig coronary arteries.

2.1 BACKGROUND

First, we present the main building blocks for clinical estimation of CT_{FFR} and the characteristics of fluid dynamics in coronary arteries. Further, we present how coronary blood flow can be modeled using simplified models of arterial hemodynamics.

2.1.1 CT_{FFR} IN THE CLINIC

As specified earlier in this chapter, CT_{FFR} is a result of an interaction between a geometric model, a physical model, and a physiological model. For a more in-depth presentation of CT_{FFR} , we recommend the article *Computational Fluid Dynamics Applied to Cardiac Computed Tomography for Noninvasive Quantification of Fractional Flow Reserve* by Taylor et al. [12].

2.1.1.1 GEOMETRIC MODEL

Computation of CT_{FFR} requires a method to extract a geometric model from CTA data. In clinical applications, segmentation algorithms extract the surface of all major vessels down to the limit imposed by the resolution of CTA. Thus, the segmentation algorithm defines the boundaries of our fluid domain.

Cardiovascular vessel segmentation in general, and coronary artery segmentation in particular has been a major research topic over the last years. This effort has resulted in a tremendous development of both manual, semi-automatic and automatic methods for coronary segmentation [30].

2.1.1.2 PHYSICAL MODEL

From the geometric model obtained from CTA segmentation, coronary flow and pressure can be solved using a physical model. In other words, coronary flow and pressure can be solved using the governing theory of fluid dynamics. A more in-depth presentation of this theory will be given later in this chapter. In contempt of the high rheological¹ and fluid dynamical complexity of blood flow,

¹Rheology: The study of the flow of matter.

results from major studies of CT_{FFR} (PLATFORM[[15](#)], DeFACTO[[16](#)], DISCOVER-FLOW [[17](#)]) show that coronary flow and pressure can be solved with relatively high accuracy using 3D-simulations and tools from modern CFD.

2.1.1.3 PHYSIOLOGICAL MODEL

The physical model of fluid dynamics is insufficient to solve pressure and flow of the coronary system alone. An essential requirement for successful estimation of CT_{FFR} is accurate boundary conditions and parameters that describe the behavior of blood. In general, these parameters are calculated using knowledge and models of the coronary- and systemic physiology [[12](#)]. In practice, a major part of the physiological model is based on data from CTA. Interestingly, anatomical data from CTA contains a wealth of information on physiological parameters, because "form follows function" in the cardiovascular system [[12](#)]. This means that local cardiovascular dimensions are optimized for certain values of flow and pressure, and that scaling laws can be used for specification of physiological parameters.

Also, clinical measurements of FFR is based on pressure measurements during maximum hyperemia. Therefore, an essential requirement for the physiological model is the ability to replicate the flow and pressure characteristics during maximum hyperemia.

2.1.2 FLUID DYNAMICS OF CORONARY ARTERIES

The fluid dynamics of coronary arteries is characterized by a complex relationship between the rheological properties of blood, the coronary geometry and the interaction between blood, heart and artery walls. Here, we describe the essential characteristics of coronary blood flow and how this knowledge can be used to make accurate assumptions for computational modeling.

2.1.2.1 FLOW CHARACTERISTICS

The cardiovascular system typically features low Reynolds number² pulsatile flow due to the pumping action of the heart. For human coronary arteries, experimental results have shown Reynolds numbers on the order of 100 [31] which is well within the laminar flow regime. Despite this, the presence of stenotic areas tends to disturb the blood flow. Evidence from clinical findings, laboratory experiments, and medical imaging methods shows that stenosed coronary arteries feature turbulence in the post-stenotic area which significantly modify the flow characteristics [32]. This means that stenotic flow may facilitate flow separation, recirculation, and reattachment.

One of the reasons for the turbulent behavior of stenosed arteries is the pulsatile nature of blood flow. Despite a relatively modest Womersley number³ in the coronary arteries on the order of 10 [33], pulsatile flow is known to trigger disturbances in flow characteristics. Results from Ferrari et al. [34] indicate that the laminar-turbulent transition in stenosed coronary arteries occurs at a Reynolds number of ≈ 500 which is observed in around 20% of the patients. Giddens et al. [35] showed that the laminar-turbulence transition is dependent on the degree of area reduction of the stenosis, and report laminar-turbulence transition points between a Reynolds number of 500 and 1000 for different stenoses geometries and flow conditions.

2.1.2.2 BLOOD RHEOLOGY

Blood is a heterogeneous multi-phase mixture of cells (red blood cells, white blood cells, and platelets), suspended in a liquid plasma that is an aqueous solution of proteins, organic molecules, and minerals. While the plasma is essentially a Newtonian fluid, the cells show a clear non-Newtonian rheology such as shear thinning, yield stress and viscoelasticity [36]. Moreover, blood is

²Reynolds number: Dimensionless number in fluid dynamics that quantifies the ratio of inertial forces to viscous forces.

³Womersley number: Dimensionless number in biofluid dynamics that quantifies the ratio of transient inertial effects to viscous effects.

recognized as an incompressible fluid [37]. The complexity of blood flow is challenging for mathematical modeling since no single model can capture the whole nature of blood flow in physiological systems.

In general, blood experiences a transition from non-Newtonian to Newtonian with increasing shear rate and fluid velocity. Johnston et al. [38] compared five non-Newtonian models and one Newtonian model on flow characteristics and shear stress in the right coronary arteries. They found that for mid-range velocities of around 0.2 m/s ($Re \approx 300$), the models are virtually indistinguishable, but that non-Newtonian effects becomes more critical at lower velocities. While there is no sharply-defined critical limit for the transition from non-Newtonian to Newtonian flow, there seems to be a general consensus that the shear rate range for which non-Newtonian effects are considered significant is $< 100 \text{ s}^{-1}$ [36]. When the narrowing artery approaches a diameter close to the size of a red blood cell, blood tends to act as a two-phase liquid with a core of red blood cells and a peripheral plasma flow. In this case, blood is more successfully modeled as a power law- or Casson fluid [39].

The viscosity of blood is dependent on a number of factors, including the concentration of red blood cells and temperature. Also, the viscosity of blood has been shown to alter in multiple pathological conditions [40].

2.1.2.3 FLUID-STRUCTURE INTERACTION

The coronary blood system is made up of elastic arteries. However, the magnitude of the dynamic effect of coronary arteries on pressure drop and FFR is unclear. For example, the elasticity of coronary arteries has been shown to have a significant effect on flow velocity and wall shear stress [41]. In contrast, Zeng et al. reported that neglection of vessel compliance resulted in a minor error for cardiovascular flow simulations of the proximal right coronary artery [42]. Similarly, Wellnhofer et al. reported that neglection of elasticity is an acceptable assumption for clinical studies of atherosclerosis [43].

2.1.2.4 STEADY-STATE VS PULSATILE FLOW

A commonly used assumption in simulations of coronary arteries is steady-state flow. Intuitively, this assumption might seem questionable. It is reasonable to assume that steady-state simulations are unable to capture the physiological characteristics of pulsatile blood flow. Despite this, empirical data suggests the assumption of steady-state flow have limited effect on the pressure drop and FFR in coronary arteries. In fact, Huo et al. showed that the steady-state assumption resulted in a pressure drop error of less than $\pm 5\%$ in an *in vitro* model [44].

2.1.2.5 FLOW IN CURVED ARTERIES

The coronary arteries have a significant curvature which introduces complex flow characteristics in the coronary system. The most vital effects of curvature is a shift of axial velocity to the outer wall and the presence of secondary flows [45]. Secondary flows are termed Dean's vortices and are commonly observed in the coronary system [46]. The magnitude of the effect of coronary curvature is unclear. However, results from Wang and Xiaofei [47] indicate that the effect of curvature on energy dissipation in tube flow is limited and that neglecting the curvature is a valid assumption in hemodynamic simulations.

2.1.3 COMPUTATIONAL MODELING OF CORONARY BLOOD FLOW

State-of-the-art algorithms for CT_{FFR} is based on rigorous three-dimensional CFD analysis. In this thesis, methods for uncertainty quantification and sensitivity analysis require a large number of model evaluations. Thus, the full three-dimensional procedure would be infeasible with our current computational resources. For this reason, we investigate methods to quantify and reduce the uncertainty of CT_{FFR} using simplified models.

2.1.3.1 SIMPLIFIED MODELS FOR CORONARY BLOOD FLOW

The fluid dynamics of coronary arteries is governed by the Navier-Stokes equations for incompressible flow

$$\rho \frac{D\mathbf{u}}{Dt} = \rho \mathbf{f} - \nabla p + \mu \nabla^2 \mathbf{u} \quad (2.1)$$

$$\nabla \cdot \mathbf{u} = 0 \quad (2.2)$$

where Equation 2.1 represents the conservation of momentum and Equation 2.2 represents the conservation of mass. Here, \mathbf{u} is the velocity vector, \mathbf{f} is a force term, μ is the dynamics viscosity, ρ is the density of the fluid and the term

$$\frac{D\mathbf{u}}{Dt} = \frac{\partial \mathbf{u}}{\partial t} + \mathbf{u} \cdot \nabla \mathbf{u} \quad (2.3)$$

is the material derivative of the velocity vector.

In a CFD analysis of the coronary arteries, the three-dimensional incompressible Navier-Stokes equation are solved for the entire fluid domain. The transient and turbulent nature of blood flow require that the Navier-Stokes equations are solved with a resolution similar to the smallest scale of turbulence, the Kolmogorov scale [48]. Unfortunately, this is an infeasible requirement in most practical applications of CFD. In practice, CFD analysis relies on turbulence models to model transitional and turbulent flow with reasonable accuracy.

In this work, the computational demand of three-dimensional uncertainty quantification and sensitivity analysis is challenging with our current computational resources. Therefore, we approximate the fluid-dynamical behavior of coronary arteries by using a reduced-order model. The aim of this approach is to construct a reduced-order model with low computational cost and sufficient accuracy to give a good approximation of the behavior of full three-dimensional CT_{FFR} models.

The fluid dynamics of the reduced-order CT_{FFR} model in this thesis is based on a zero-dimensional or lumped-parameter hemodynamical model.

Lumped-parameter models assume a uniform distribution of the fundamental variables within any particular compartment (vessel or part of a vessel) of the model at any instant in time. In contrast, higher-dimensional models recognize the variation of these parameters in space. For example, one-dimensional models are based on the integration of fundamental variables along the centerlines of the vessels.

Reduced-order models have a long history in the field of biomechanics. Several authors report that 1D models offer excellent accuracy with considerably less cost than the equivalent 3D models [49, 50]. However, 1D reduced-order models have been shown to yield unrealistic results in pathological regions like aneurysms and stenoses and are often connected to lumped-parameter stenosis models or empirical corrections to improve performance in critical vessel segments [51]. The reason for this behavior is that the derivation of one-dimensional models is usually based on the assumption of small variations in the cross-sectional vessel area, something that is not necessarily true in the presence of stenosis [51]. Also, lumped-parameter models are frequently used for boundary conditions in 1D-3D models of the arterial system. For example, the Windkessel model⁴ is a frequent choice for outflow boundary conditions in hemodynamic simulations [52]. To construct a complete model, several lumped-element models can be connected using electric circuit analogy. Electric circuit analogy will be explained further in the next section.

2.1.3.2 ELECTRIC ANALOGY OF CORONARY SYSTEM

One of the simplest ways to describe blood flow in the coronary arterial system and connect lumped-parameter models of different vessel compartments is through electric circuit analogy. For this reason, the electric circuit analogy will be frequently used in this thesis.

Flow in human arteries is subject to resistive forces. In electrical analogy, the

⁴Windkessel model: a model that describes the hemodynamics of the arterial system in terms of resistance and compliance.

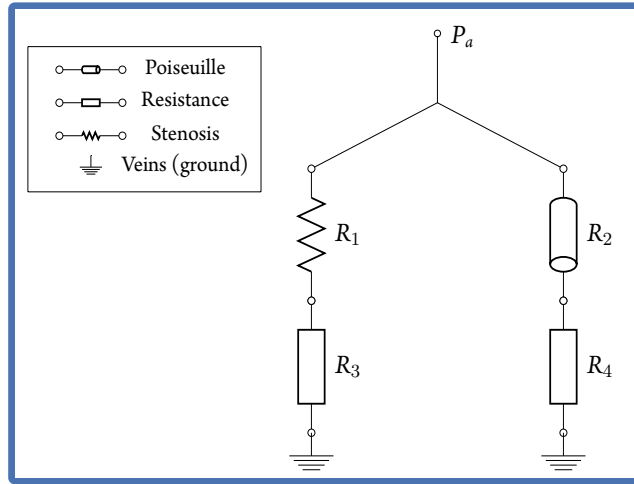


Figure 2.1.1: Example of electric circuit analogy of human coronary arterial system where P_a is the arterial pressure, R_1 is a non-linear stenosis resistance, R_2 is a linear Poiseuille resistance and R_3/R_4 are terminal resistances that models the resistance of the microvascular and venous system. The ground symbols represents the central venous pressure that is assumed to be 0 mmHg.

resistance R of an artery is given by the following relation

$$QR = \Delta P, \quad (2.4)$$

where ΔP is the pressure drop over the vessel, and Q is the volumetric flow rate. Note that the resistance R is not necessarily a constant and can be a function of P and Q .

For a healthy vessel, assuming that blood obeys Poiseuille's law, the resistance can be written as [53]

$$R = \frac{8\pi\mu L}{\nu} = \text{constant}, \quad (2.5)$$

where μ is the dynamic viscosity, ν is the kinematic viscosity and L is the vessel length.

For a stenosed vessel, the linear relationship between flow rate and pressure in Equation 2.5 breaks down. In contrast, stenosed vessels are shown to experience

a quadratic relationship between flow rate and pressure [54, 55]

$$P = QR_1 + Q^2R_2, \quad (2.6)$$

where R_1 and R_2 are empirical resistance coefficients.

The electrical analogy simplifies the analysis of branching vascular systems. In practice, the cardiovascular system can be modelled as a network of resistors in series and parallel. For n resistors in series, the total resistance is given by

$$R_{tot} = \sum_n R_n. \quad (2.7)$$

For resistors in parallel, the total resistance is given by

$$R_{tot} = \left(\sum_n R_n^{-1} \right)^{-1}. \quad (2.8)$$

By introducing the conductance G , defined as the reciprocal of the resistance

$$G = \frac{1}{R}, \quad (2.9)$$

we get the following relation for vessels in parallel

$$G_{tot} = \sum_n G_n. \quad (2.10)$$

A commonly used assumption in cardiovascular simulations is that the central venous pressure⁵ is equal to 0 mmHg. With this assumption, we simplify the relationship between arterial blood pressure P_a and total vascular resistance R_{tot} , so that the cardiac output Q_{co} is given by

$$Q_{co} = \frac{P_a}{R_{tot}} \quad (2.11)$$

⁵Central venous pressure: Blood pressure in the venae cavae, near the right atrium of the heart.

An example of an electrical analogy of a simplified vascular system can be seen in Figure 2.1.1.

2.1.3.3 HUO MODEL

As previously seen in this chapter, the linear relationship between flow rate and pressure drop according to Poiseuille's law breaks down in the presence of stenosis. To calculate this effect, Huo et al. [44] propose an analytical model for the pressure drop over an axisymmetric stenosis. This model is derived from conservation of energy, which considers convective and diffusive energy losses as well as energy loss due to sudden constriction and expansion in lumen area. Despite its simplicity, the model has shown to provide a good fit with *in vitro* and *in vivo* experimental measurements for a single stenosis.

The Huo model is based on the Bernoulli equation. Since gravity is negligible in the coronary circulation, the general Bernoulli equation can be written as

$$\Delta P = \Delta P_{convective} + \Delta P_{constriction} + \Delta P_{diffusive} + \Delta P_{expansion} \quad (2.12)$$

where the pressure drop over a stenosis is given by the superposition of pressure drops from convection, constriction, diffusion and expansion.

The pressure drop due to convection, $\Delta P_{convective}$ is defined from the following equation

$$\Delta P_{convective} = \frac{\rho Q^2}{2} \left(\frac{1}{A_{outlet}^2} - \frac{1}{A_{inlet}^2} \right). \quad (2.13)$$

If the flow transition from a proximal normal vessel to a stenosis is well-bound and follows the streamlines, the energy loss due to a sudden constriction is relatively small (loss coefficient $<< 0.1$ generally) and negligible so that $\Delta P_{constriction} \approx 0$.

$\Delta P_{diffusive}$ is result of the entrance effect and the viscosity in the fully developed region. For the entrance region of a stenosis, we define a dimensionless radius of

the inviscid core⁶, α , that can be calculated from

$$\frac{\pi\mu L_{stenosis}}{4\rho Q} = \frac{1}{4} \int_a^1 \frac{(1-\alpha)(6+\alpha)(1+4\alpha+9\alpha^2+4\alpha^3)}{5\alpha(3+2\alpha)(3+2\alpha+\alpha^2)^2}, \quad (2.14)$$

where $L_{stenosis}$ is the length of the stenosis.

If $\alpha \geq 0.05$, which is the case for most clinical stenoses, $\Delta P_{diffusive}$ can be expressed as

$$\begin{aligned} \Delta P_{diffusive}^{a \geq 0.05} &= \frac{\rho Q^2}{2A_{stenosis}^2} \frac{96}{5} \int_a^1 \frac{(1+4\alpha+9\alpha^2+4\alpha^3)}{\alpha(3+2\alpha)(3+2\alpha+\alpha^2)^2} d\alpha \\ &\quad + \int_0^{L-L_{stenosis}} \frac{8\pi\mu}{A^2} Q dx, \end{aligned} \quad (2.15)$$

and $\Delta P_{expansion}$ as

$$\begin{aligned} \Delta P_{expansion}^{a \geq 0.05} &= \frac{\rho Q^2}{2} \left\{ \left(\frac{1}{A_{stenosis}} - \frac{1}{A_{distal}} \right)^2 \right. \\ &\quad + \left[2 \left(\frac{1}{A_{stenosis}} - \frac{1}{A_{distal}} \right) \right. \\ &\quad \cdot \left(\frac{1}{A_{stenosis}} - \frac{1}{3A_{distal}} \right) \\ &\quad \left. \left. - \left(\frac{1}{A_{stenosis}} - \frac{1}{A_{distal}} \right)^2 \right] (1-\alpha)^2 \right\}. \end{aligned} \quad (2.16)$$

If $\alpha < 0.05$, the entrance length can be found from the following equation,

$$\frac{\pi\mu L_{entrance}}{4\rho Q} = \frac{1}{4} \int_{0.05}^1 \frac{(1-\alpha)(6+\alpha)(1+4\alpha+9\alpha^2+4\alpha^3)}{5\alpha(3+2\alpha)(3+2\alpha+\alpha^2)^2}. \quad (2.17)$$

⁶Inviscid core: Region of a fluid flow that is assumed to have no viscosity.

Consequently, $\Delta P_{diffusive}$ can be expressed as

$$\begin{aligned}\Delta P_{diffusive}^{\alpha < 0.05} = & \frac{\rho Q^2}{2A_{stenosis}^2} \frac{96}{5} \int_{0.05}^1 \frac{(1 + 4\alpha + 9\alpha^2 + 4\alpha^3)}{\alpha(3 + 2\alpha)(3 + 2\alpha + \alpha^2)^2} d\alpha \\ & + \int_0^{L-L_{entrance}} \frac{8\pi\mu}{A^2} Q dx,\end{aligned}\quad (2.18)$$

and $\Delta P_{expansion}$ as

$$\begin{aligned}\Delta P_{expansion}^{\alpha < 0.05} = & \rho Q^2 \left(\frac{1}{A_{stenosis}} - \frac{1}{A_{distal}} \right) \\ & \cdot \left(\frac{1}{A_{stenosis}} - \frac{1}{3} \frac{1}{A_{distal}} \right).\end{aligned}\quad (2.19)$$

2.1.4 GEOMETRIC DATA

To investigate morphometrical relationships and simulate CT_{FFR} in physiologically relevant coronary geometry, we use a dataset of pig coronary morphometry from Kassab et al. [29]. In this work, the order, length, diameter and connectivity were measured for the RCA, LAD, and CX. Measurements of the coronary morphometry were done by constructing and analyzing a polymer cast of the coronary arteries. To our knowledge, this is the only published dataset that does a complete mapping of the main branches of the coronary system down to a diameter of $\approx 0.1\text{ mm}$. In contrast, the resolution of CTA does only facilitate reconstruction of coronary arteries down to a diameter of $\approx 1\text{ mm}$ [personal communication, 9/23, 2015]. Therefore, the dataset opens up the opportunity to investigate the effect of coronary arteries both visible and invisible to CTA.

An investigation from Sahni et al. found that the coronary circulation show minor differences between pigs and humans [56]. Thus, it should be fair to assume that the morphometrical characteristics in branching patterns of pig coronary arteries should be relevant for the human coronary circulation.

2.1.4.1 GEOMETRIC UNCERTAINTY

The main objective of this thesis is to investigate methods to quantify and reduce the uncertainty of CT_{FFR} . Thus, for most simulations, we are not interested in the geometric uncertainty of the morphological dataset.

In simulations which consider the geometric uncertainty, we base the uncertainty on reported values from CTA segmentation. Results from Mazinani et al. [57] report uncertainties of up to $\pm 30\%$ in predictions of coronary artery diameters. However, this work was published in 2011 and is expected to show a higher uncertainty than today's state-of-the-art algorithms. For example, Sankaran and Taylor [?] reports a diameter uncertainty of $\pm 0.3mm$ and a length uncertainty of $\pm 1mm$ in a recent study. In our thesis, we assume a normally distributed diameter uncertainty with a standard deviation $\sigma = 15\%$, which is more consistent with the work done by Sankaran and Taylor. It is important to note that this number is highly uncertain, and is only meant to give an impression of the influence of geometric uncertainty for CT_{FFR} .

2.2 CT_{FFR} MODEL

In this section, we propose a lumped-parameter network model of the coronary system. First, we describe the building blocks of our model, before we describe the procedure to obtain an estimate of flow, pressure and FFR in the coronary system. Also, we describe the relevant uncertainty in the physiological parameters used in this model.

2.2.1 LUMPED-PARAMETER NETWORK MODEL

Here, we describe how our lumped-parameter network model is constructed. A schematic representation of our lumped-parameter network model can be seen in Figure 2.2.1.

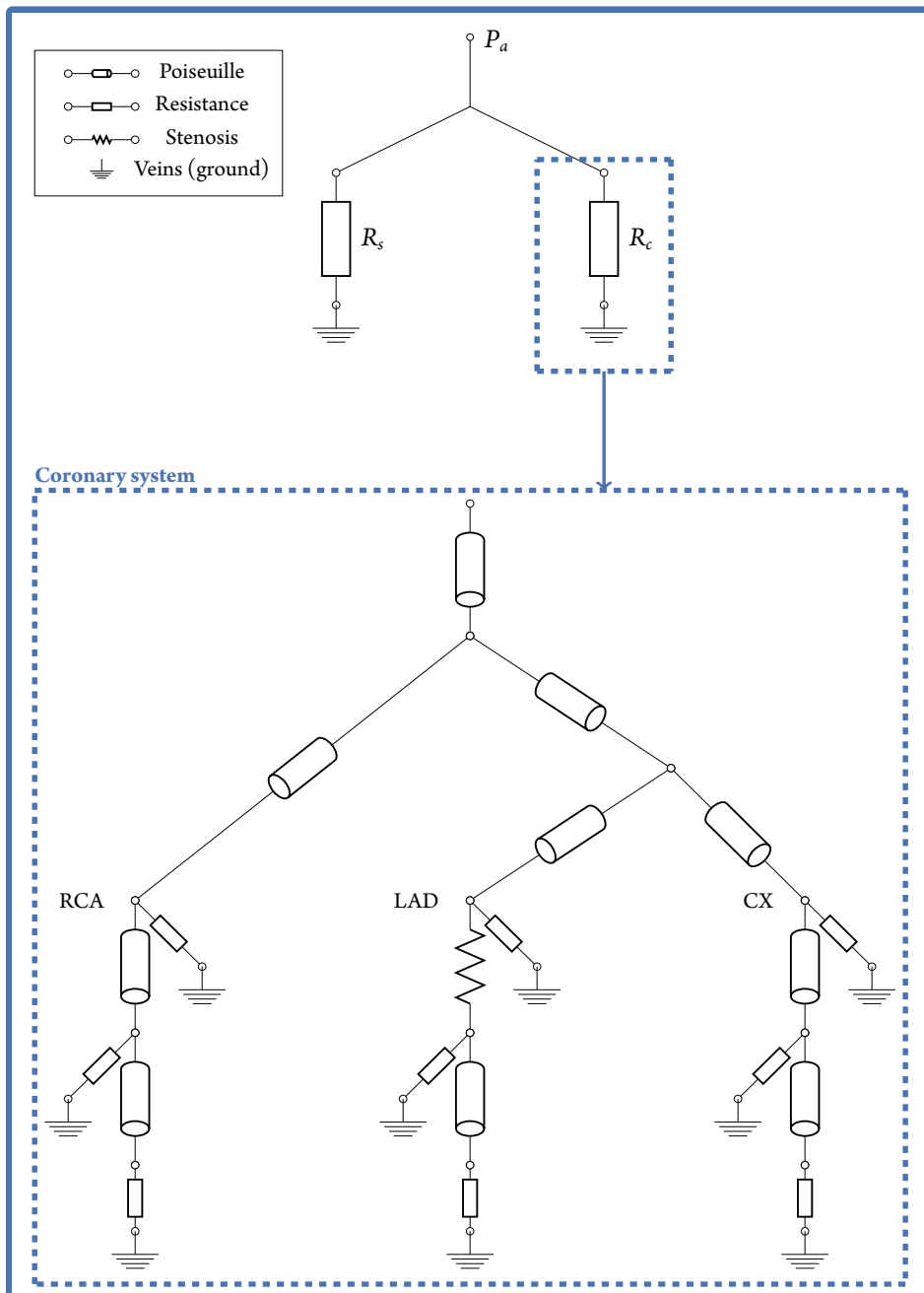


Figure 2.2.1: Figure showing the CT_{FFR} model where P_a is arterial blood pressure, R_s is the systemic resistance and R_c is the total resistance of the coronary system. Further, the coronary system is divided into three branches that represents the RCA, LAD and CX. A non-linear stenosis resistance can be seen in the LAD.

2.2.1.1 LUMPED-PARAMETER ELEMENTS

In this work, we model the pressure over stenosed vessel segments using the validated lumped-parameter stenosis model by Huo et al. [44]. For healthy vessels segments, we model the pressure drop using Poiseuille's law [53], a model that have been shown to yield acceptable results in several studies [58, 59]. These models are based on the assumptions of solid walls, steady-state flow, Newtonian fluid, incompressible flow and straight arteries. Furthermore, the healthy vessel segments are based on the assumption of laminar flow. The validity of these assumptions was described in Section 2.1.3.1. The lumped-parameter models are connected using electric circuit analogy, which was introduced in Section 2.1.3.2.

2.2.1.2 BOUNDARY CONDITIONS

The pressure and flow in our fluid domain are governed by the network of Poiseuille- and Huo elements. Also, our CT_{FFR} model requires specification of a relationship between flow and pressure at the boundaries of our fluid domain. This can be specified by a fixed value for pressure and flow at the outlets or inlets, or by using a mathematical relationship between pressure and flow.

For the inflow to our arterial system, we use fixed values for flow and/or pressure, in a procedure that will be explained in-depth in Section 2.2.2. For terminal vessels, we model the micro-vascular and venous system using linear resistances which is equivalent to a steady-state solution of the Windkessel model.

The most promising way to establish vascular resistances in terminal vessels for estimation of CT_{FFR} is optimal design principles. There seems to be a widespread consensus that branching morphology in biological systems is subject to optimization principles justified by evolutionary morphogenetic arguments based on natural selection [21–23]. The most prominent and influential branching model based on optimization principles is Murray's law. Murray's law is derived from the minimization of energy consumption of flow systems in living organisms [22, 23].

Formally, Murray's law is given by

$$q_i \propto r_i^c, \quad (2.20)$$

where c is a constant, q_i is the flow rate and r_i is the vessel radius. According to Murray's original work, the metabolic energy consumption is proportional to r^2 , while the mechanical energy consumption for laminar flow is proportional to r^4 , giving an optimization constant $c = 3$ [22, 23]. The resistance of a terminal vessel is given by

$$R_i \propto r_i^{-c}, \quad (2.21)$$

and is used to specify the relative values of terminal resistances. The absolute values are then determined such that the overall pressure drop corresponds to the specified boundary conditions for flow and pressure as described in Section 2.2.2.

2.2.2 SOLUTION PROCEDURE

Similar to Itu et al. [27] and Taylor et al. [12], the computation of CT_{FFR} in this work is based on a two-step algorithm. First, the boundary conditions are determined in the resting state. Second, we determine the boundary conditions in the hyperemic state. Once the hyperemic boundary conditions have been established, an estimate of pressure, flow and FFR can be obtained for different positions in the coronary system.

2.2.2.1 RESTING CONDITIONS

The first step of the solution procedure is to calculate proper boundary conditions in the resting state. We assume that the values of cardiac output Q_{co} and myocardial flow fraction (MFF) Λ_{myo} is known in the resting state. MFF represents the fraction of total aortic flow to the coronary system. Therefore, myocardial flow is given by $Q_{myo} = \Lambda_{myo} Q_{co}$. Further, we assume that the arterial blood pressure P_a is known in the resting state. Assuming a central venous

pressure of 0 mmHg, calculation of total cardiovascular resistance R_{tot} , total coronary vascular resistance R_{cor} and systemic vascular resistance R_{sys} is straightforward and results in

$$R_{tot} = \frac{P_a}{Q_{co}}, \quad (2.22)$$

$$R_{cor} = \frac{P_a}{Q_{myo}}, \quad (2.23)$$

$$R_{sys} = \frac{P_a}{Q_{co} - Q_{myo}}. \quad (2.24)$$

As described in Section 2.2.1.2, the relative resistances are given by Murray's law. Thus, the resistance of outlet i is given by

$$R_i = \left(G_{micro} \frac{r_i^c}{\sum_k r_k^c} \right)^{-1}, \quad (2.25)$$

where k are the number of vascular outlets and $G_{micro} = \frac{1}{R_{micro}}$ is the total microvascular conductance.

For a linear system of healthy vessel segments, the calculation of the total microvascular conductance G_{micro} is a straightforward procedure that can be done using basic circuit theory. In contrast, stenosed vessel segments introduce non-linearities that significantly complicates our solution procedure. In this work, we introduce a flow split variable so that for each branching junction the flow in the daughter vessels Q_{d_1} and Q_{d_2} is given by the flow in the mother vessel Q_m and the flow split variable Λ

$$Q_{d_1} = \Lambda Q_m, \quad (2.26)$$

$$Q_{d_2} = (1 - \Lambda) Q_m, \quad (2.27)$$

where $0 \leq \Lambda \leq 1$.

Thus, the system is solved by finding the total microvascular conductance G_{micro} and the split coefficients Λ_k where k is the number of branching junctions.

The problem is similar to finding the roots of

$$g(\boldsymbol{\Lambda}, G_{micro}) = \mathbf{0}, \quad (2.28)$$

where $\boldsymbol{\Lambda} = [\Lambda_1, \dots, \Lambda_k]$ and the function g is defined as

$$g(\boldsymbol{\Lambda}, G_{micro}) = \mathbf{P}_o(\boldsymbol{\Lambda}, G_{micro}) - \mathbf{Q}_o(\boldsymbol{\Lambda}, G_{micro}) \cdot \mathbf{R}_o(G_{micro}) \quad (2.29)$$

where \mathbf{P}_o , \mathbf{Q}_o and \mathbf{R}_o are the vectors of outlet pressures, outlet flows and outlet resistances, respectively. Once the total microvascular conductance is calculated, the calculation of the absolute value of terminal resistances are trivial.

2.2.2.2 HYPEREMIC CONDITIONS

The next step is to model the hyperemic response. In the clinic, a hyperemic response is triggered by intravenous or intracoronary injection of the vasodilatory drug adenosine and leads to an increase in coronary flow velocity by a factor of 4.5 in normal, healthy subjects [60]. Similarly to the work of Taylor et al. [12] and Ito et al. [27], we model the effect of adenosine by reducing the resting terminal resistances by a factor commonly referred to as the Total Coronary Resistance Index (TCRI). TCRI is defined as the ratio of hyperemic to normal coronary resistance. Thus, the hyperemic outlet resistance $R_{h,i}$ for a terminal outlet i is given by

$$R_{h,i} = R_i \cdot \text{TCRI}. \quad (2.30)$$

We model the effect of adenosine by an approach similar to the work of Itu et al. [27]. This involves holding the total cardiac output constant and using the arterial pressure P_a as a free variable. Thus, we want to find the roots of

$$h(\boldsymbol{\Lambda}, P_a) = \mathbf{0}, \quad (2.31)$$

where the function h is defined as

$$h(\boldsymbol{\Lambda}, P_a) = \mathbf{P}_o(\boldsymbol{\Lambda}, P_a) - \mathbf{Q}_o(\boldsymbol{\Lambda}, P_a) \cdot \mathbf{R}_h. \quad (2.32)$$

and \mathbf{R}_h is a vector of the hyperemic terminal resistances.

The presented hyperemic model is equivalent to model coronary inflow Q_{cor} during hyperemia as a function of the coronary resistance R_{cor} . Using this method, the model is in good agreement with empirical results that finds a strong correlation between coronary flow reserve⁷ and FFR [61].

2.2.2.3 NON-LINEAR MULTIDIMENSIONAL ROOT FINDING

Finding the roots of Equation 2.28 and Equation 2.31 for diseased coronary arteries involves a complex non-linear multidimensional root finding problem. The problem is complicated by the fact that non-linear lumped elements prohibit an analytical solution of the Jacobian⁸.

To solve this problem, we use the HYBRD algorithm from *Scipy* [62] and MINPACK [63]. The HYBRD algorithm is based on a modified version of Powell's hybrid method. This method is based on a sophisticated hybrid of Newton's method and the gradient descent method. Here, the Jacobian is calculated by a forward-difference approximation. To lower the number of required function evaluations, HYBRD uses a relaxation technique to update the Jacobian and do not require a complete recalculation of the finite difference approximation at every solution step [63].

2.2.3 UNCERTAINTY OF PHYSIOLOGICAL PARAMETERS

Physiological parameters for CT_{FFR} can be derived with different methods where the most straight-forward way is by using population-based statistics. Another method to establish physiological parameters for CT_{FFR} is by using information from CTA. Anatomical data from CTA contains a wealth of information since

⁷Coronary flow reserve: ratio of hyperemic to resting flow rate

⁸Jacobian: Matrix of first-order partial derivatives of a vector-valued function.

"form follows function" in physiological systems [64]. In the vascular system, allometric⁹ scaling laws are critical for enabling the physiological system to deliver blood at an appropriate flow rate and pressure [12]. Last, physiological parameters for CT_{FFR} can be estimated by supplementary clinical data.

Here we present relevant data to establish the uncertainty in physiological parameters for CT_{FFR} . The relevant physiological parameters for our CT_{FFR} model are cardiac output, mean arterial pressure, MFF, flow distribution parameters, microvascular vasodilatory response, blood viscosity and blood density.

2.2.3.1 CARDIAC OUTPUT

Experimental results have found a cardiac output of between $4 - 8 \text{ L/min}$ in healthy adults [65]. Here, we model the uncertainty in cardiac output as a uniform random variable with a lower value of 4 L/min and an upper value of 8 L/min .

2.2.3.2 MEAN ARTERIAL PRESSURE

In a study by Sesso et al. of 11 150 male physicians with no history of cardiovascular disease, the mean arterial pressure (MAP) was found to be $93.0 \pm 7.6 (\text{mean} \pm \text{SD}) \text{ mmHg}$ [66]. Thus, we model mean arterial pressure as a normal distributed random variable with mean $\mu = 93.0 \text{ mmHg}$ and a standard deviation $\sigma = 7.6 \text{ mmHg}$.

2.2.3.3 MYOCARDIAL FLOW FRACTION (MFF)

The heart consumes over 75 % of the oxygen delivered to it at rest, and thus no significant oxygen reserve exists [67]. Therefore, the heart has limited ability to increase oxygen extraction during conditions of decreased inflow. There is limited evidence of altered MFF in coronary artery disease [67]. Results from Pijls et al. show a myocardial blood flow between $4 - 5 \%$ of total cardiac output

⁹Allometry: Allometry describes how the characteristics of living organisms change with size.

[68]. Therefore, we model the uncertainty in the MFF as a uniformly distributed random variable with a lower value of 4 % and an upper value of 5 %.

2.2.3.4 FLOW DISTRIBUTION

As discussed earlier in this chapter, the flow distribution to terminal vessels is governed by Murray's law. Despite the solid scientific evidence, there is a wide discrepancy in the reported values of Murray's coefficient. In this thesis, we model Murray's coefficient c as a uniform random variable with a lower value of 2.4 and an upper value of 3. An in-depth discussion of Murray's law and relevant values of Murray's coefficient is presented in Chapter 5.

2.2.3.5 MICROVASCULAR VASODILATORY RESPONSE

The most widely used metric for microvascular vasodilatory response is TCRI, which is defined as the ratio of hyperemic to normal coronary resistance. A mean value of $\text{TCRI} = 0.22$ has been obtained during various studies. It is reported to increases from 0.22, for a heart rate less than 75bpm, to 0.26, for a heart rate of 100bpm, and to 0.28 for a heart rate of 120bpm in healthy subjects or subjects with mild coronary artery disease [69]. In this thesis, we assume a physiological range of $0.15 - 0.3$. This is in good agreement with Sankaran and Taylor [20] who inferred a lower and upper 95% confidence bound of TCRI that corresponds to 65% and 130% of the mean ($\text{TCRI} = 0.22$) in patients without microvascular disease¹⁰.

2.2.3.6 BLOOD VISCOSITY

Similarly to Sankaran and Taylor [?], we model the blood visosity as a function of hematocrit¹¹ (Hct) and the viscosity of plasma μ_p ($0.0011 \text{ Pa} \cdot \text{s}$)

$$\mu = \frac{\mu_p}{(1 - Hct)^{2.5}}. \quad (2.33)$$

¹⁰Microvascular disease: Disease that affects the tiny arteries of the arterial system.

¹¹Hematocrit: Volume percentage of red blood cells in blood.

Values of hematocrit have been reported as 0.45 ± 0.08 (mean \pm SD) [70]. Thus, we model the uncertainty of blood viscosity through a normally distributed random variable for hematocrit.

2.2.3.7 BLOOD DENSITY

Hinghofer-Szalkay and Greenleaf found the blood density to be in the range of $1043 - 1057 \text{ kg/m}^3$ [71]. Here, we model the uncertainty of the blood density as a uniformly distributed random variable with a lower value of 1043 kg/m^3 and an upper value of 1057 kg/m^3 .

2.3 SUMMARY

In this chapter, we propose a lumped-parameter CT_{FFR} model to investigate methods to quantify and reduce uncertainty in CT_{FFR} models. The simplified model is based on principles from the most prominent work in the field of CT_{FFR} . First, we present the governing theory for zero-dimensional fluid-dynamical models, also called lumped-parameter models. Second, the lumped-parameter models are used as building blocks to construct a complete model of the coronary vasculature using principles from electric circuit analogy. Finally, the model is completed using a physiological model to calculate boundary conditions and simulate the effect of maximal hyperemia.

Also, we present the coronary geometry dataset used for the experiments in this thesis. The dataset is based on published data from Kassab et al. [29] and is a result of the construction and analysis of a polymer cast of pig coronary arteries.

If you can't explain it simply, you don't understand it well enough.

Albert Einstein

3

Uncertainty Quantification and Sensitivity Analysis

In this chapter, the governing theory of uncertainty quantification (UQ) and sensitivity analysis (SA) is presented. For a more in-depth investigation of uncertainty quantification and sensitivity analysis, we refer to the work of R.C Smith, *Uncertainty Quantification: Theory, Implementation, and Applications* [72].

3.0.1 UNCERTAINTY QUANTIFICATION (UQ)

Uncertainty quantification is the science of quantitative characterization of uncertainty and is used to characterize uncertainties and give reliable predictions for practical problems. UQ tries to find how likely some outcomes are in a system where some aspects of the system are not exactly known.

In this thesis, we distinguish between two broad types of uncertainty

quantification problems. The first type is forward propagation of uncertainty, where the uncertainty of input parameters is propagated to determine the overall uncertainty of our model. The second is backward propagation of uncertainty where the uncertainty of input parameters are inferred from the observed model output.

3.0.1.1 FORWARD PROPAGATION OF UNCERTAINTY

In forward propagation uncertainty, we want to quantify a response Y (e. g. FFR) of a computational science problem. We take in uncertain input parameters \mathbf{Z} and compute the problem by a functional black box f (forward model)

$$Y = f(\mathbf{Z}), \quad (3.1)$$

where random variables are represented by upper case letters. Here, \mathbf{Z} is a vector of model parameters and may include material or geometric model parameters like blood density or aortic diameters. Note that Y is represented as a single variable, but can also be a vector of outputs [73, 74].

The literature contains a wide variety of methods for forward propagation of uncertainty [75]. In general, the choice method depends on the computational effort, accuracy and the characteristics of the problem. For example, approximate models, often called metamodels, have been shown to drastically reduce the computational effort in computer-aided engineering applications [76]. In this work, we utilize a combination of Monte Carlo (MC) simulations and metamodeling techniques, e.g. generalized polynomial chaos (PC) and random forest (RF) for forward propagation of uncertainty.

3.0.1.2 BACKWARD PROPAGATION OF UNCERTAINTY

In backward propagation uncertainty, we want to infer probability distributions of uncertain input parameters \mathbf{Z} , from an observed model output y_{obs} subject to

noise ε

$$y_{obs} + \varepsilon = f(\mathbf{Z}). \quad (3.2)$$

where the uncertain input parameters could be both unobserved and observed. The general problem of determining input parameters from the observed model output is called an inverse problem and could be of both deterministic and probabilistic nature [77].

In general, backward propagation is a more difficult problem than forward propagation and several ways to approach this problem exists. In this thesis, we rely on the Bayesian approach for backward propagation of uncertainty that establishes a convenient probabilistic framework for inverse problems. In particular, modern Bayesian inference offers convenient tools to infer distributions of unobserved model parameters, often called hidden or latent variables [78].

3.0.2 SENSITIVITY ANALYSIS (SA)

Sensitivity Analysis (SA) is used to quantify how the uncertainty in the output of a model can be apportioned to different sources of uncertainty in the model input [79]. In practice, SA is used to determine which input parameters are important and which input parameters are less important to the overall response of our system.

SA methods are divided into local and global methods, depending on the range of input values considered. Local SA aims to quantify the local impact of input parameters and is based on the computation of the gradient of the output with respect to its input parameters around a nominal input value [80]. Typically, local SA is performed by perturbing one input variable at a time, while holding the other input variables constant, a procedure that is analogous to the partial derivative.

Global SA aims to quantify the sensitivity of model output with respect to

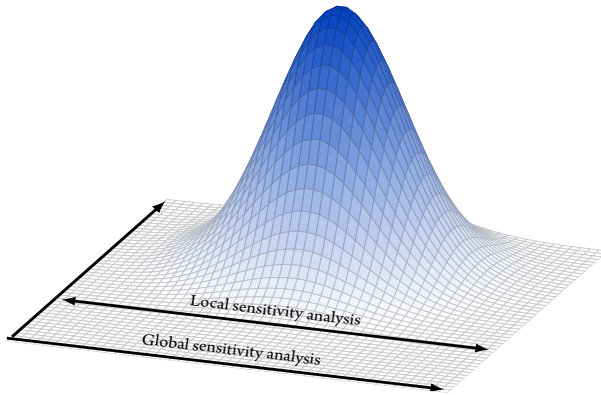


Figure 3.0.1: Schematic figure showing the difference between local and global sensitivity analysis for a function of two input variables (represented by the horizontal axes). In local sensitivity analysis, the sensitivity of the output to one input variable is quantified while holding the other input variable constant. In contrast, global sensitivity analysis quantifies the sensitivity of the output with respect to the input variables over the whole input space.

model inputs over the whole input space. Global SA methods were developed to overcome the limitations of local methods (locality, linearity, and normality assumptions) and has attracted major interest among numerical modelers [81]. A particularly important class of global SA methods is called variance-based SA. Variance-based SA decomposes the variance of the model output into fractions that can be attributed to a specific input variable or sets of inputs [81].

3.1 BACKGROUND

Consider the model described earlier in this chapter where we want to quantify the response Y

$$Y = f(\mathbf{Z}), \quad (3.3)$$

which is determined by the functional black box f and the input parameters \mathbf{Z} , where \mathbf{Z} and Y are random variables. In this section, we define the basic statistical

tools and notation used to describe and model random variables throughout this thesis.

3.1.1 PROBABILITY DISTRIBUTION FUNCTIONS

A probability distribution function is a function which is used to describe a particular probability distribution. In this thesis, the term probability distribution function might refer to a probability density function (PDF) or a cumulative distribution function (CDF)

The PDF ρ_Y for a random variable Y is given by

$$p[a \leq Y \leq b] = \int_a^b \rho_Y(y) dy, \quad (3.4)$$

where $p[a \leq Y \leq b]$ is the probability of Y being in $[a, b]$ and ρ_Y is a non-negative Lebesgue-integrable function [82]. Further, the CDF F_Y is given by

$$F_Y(y) = p(Y \leq y) = \beta, \quad (3.5)$$

where Y is a real-valued random variable. In addition to the PDF and CDF, the inverse CDF

$$F_Y^{-1}(\beta) = y, \quad (3.6)$$

is frequently used through this thesis. The inverse CDF is also referred to as the percent point function or the quantile function in the literature [83].

3.1.2 MOMENTS

Some important characteristics of the random variable Y are the expected value and variance, also known as the first and second moment. The expected value is given as

$$\mu_Y = \mathbb{E}[Y] = \int_{\Omega_Y} y\rho_Y(y) dy, \quad (3.7)$$

and the variance is

$$\sigma_Y^2 = \mathbb{V}[Y] = \int_{\Omega_Y} (y - \mathbb{E}[Y])^2 \rho_Y dy, \quad (3.8)$$

where Ω_Y is the output space and ρ_Y is the PDF associated with the output Y . The expected value or mean μ_Y can be regarded as the most likely value of the random variable Y or the "center" of Y . The standard deviation σ_Y , is the square root of the variance and it is a measure of the spread or dispersion of Y around μ_Y [84].

3.1.3 PREDICTION INTERVALS

A prediction interval is an estimate of an interval, in which future observations will fall in with a certain probability, given what has already been observed. The prediction interval is given by

$$I = [F_Y^{-1}(\underline{\alpha}), F_Y^{-1}(\bar{\alpha})], \quad (3.9)$$

where the value of $\underline{\alpha}$ and $\bar{\alpha}$ depends on the choice of interval. The most common choice is to center the interval on the median, such that the probability of a future observation to lie below or above the integral is the same. This gives that $\underline{\alpha} = \beta/2$ and $\bar{\alpha} = 1 - \beta/2$, and is called a central prediction interval. Examples of other intervals are shortest-length intervals and highest-density regions [85].

Prediction intervals are often confused with confidence intervals, which are intervals associated with a population parameter instead of future observations.

3.1.4 SENSITIVITY INDICES

In SA, we want to identify the effect of uncertain inputs $Z_i, i = 1, 2, \dots, D$ on the model response Y , either by itself or through interaction with other inputs and find the expected reduction in the uncertainty of Y if an uncertain input parameter Z_i were to be known. To quantify this, we use the global, variance-based sensitivity indices introduced by Sobol [86].

The first-order Sobol sensitivity index, also called the main sensitivity index,

gives the direct effect of an uncertain input Z_i on the output Y . It shows the expected reduction in $\mathbb{V}[Y]$ that would happen if Z_i would be its unknown true value and is defined by

$$S_i = \frac{\mathbb{V}[\mathbb{E}[Y | Z_i]]}{\mathbb{V}[Y]}, \quad (3.10)$$

where $\mathbb{E}[Y | Z_i]$ is the estimated value of Y conditioned on Z_i . The main sensitivity index is useful for determining the effect of the various inputs on the output, and also for deciding which input parameters should be assessed more carefully. The second-order sensitivity indices shows the part of $\mathbb{V}[Y]$ that results from the interaction between two uncertain input parameters, Z_i and Z_j , and is given by

$$S_{ij} = \frac{\mathbb{V}[\mathbb{E}[Y | Z_i, Z_j]]}{\mathbb{V}[Y]}. \quad (3.11)$$

The total sensitivity index was introduced by Homma and Saltelli [87] to be able to consider all interaction effects without having to estimate all higher-order sensitivity indices. The total sensitivity index is the sum of all first and higher order effects where Z_i is involved [87]. It is defined by

$$S_{T,i} = \frac{\mathbb{V}[Y] - \mathbb{V}[\mathbb{E}[Y | Z_{-i}]]}{\mathbb{V}[Y]} = 1 - \frac{\mathbb{V}[\mathbb{E}[Y | Z_{-i}]]}{\mathbb{V}[Y]}, \quad (3.12)$$

where Z_{-i} is the set of all uncertain inputs except Z_i . The total sensitivity index is a metric measure of the part of $\mathbb{V}[Y]$ caused by both the direct effect of Z_i and all interaction effects of input Z_i . The accumulation of all higher order interactions is given by $S_{T,i} - S_i$, where a difference of zero indicates that no interactions is present. Since the uncertainty in the input values are not important when $S_{T,i}$ has a value close to zero, $S_{T,i}$ is useful to determine which input parameters can be given a fixed value within their uncertainty domain [74].

3.1.5 MODELLING RANDOM VARIABLES: ROSENBLATT TRANSFORMATION

When doing numerical methods for UQ, it is necessary to create N pseudo-random realizations $\{\mathbf{z}^{(s)}\}_{s=1}^N$ from the probability density function $\rho_{\mathbf{Z}}$. Each $\mathbf{z}^{(s)} \in \{\mathbf{z}^{(s)}\}_{s=1}^N$ is multivariate with the number of dimensions $D > 1$, where the number of dimensions signify the number of input variables. Finding realizations from $\rho_{\mathbf{Z}}$ can be difficult, especially for large D s. In UQ, it is common to make the assumption that each dimension in \mathbf{Z} consists of stochastically independent components, which allows for a joint sampling scheme to be reduced to a series of univariate samplings. This assumption significantly simplifies the generation of samples $\mathbf{z}^{(s)}$ [73].

Alas, the assumption of independence is not always valid in practice, and modeling of stochastically dependent variables are often necessary for proper UQ. In this thesis, we use the open-source toolbox Chaospy, which has strong support for stochastic dependence [73].

All random samples in Chaospy are created using Rosenblatt transformations $T_{\mathbf{Z}}$. A random variable \mathbf{U} that is generated uniformly on a unit hypercube $[0, 1]^D$, can then be transformed into $\mathbf{Z} = T_{\mathbf{Z}}^{-1}(\mathbf{U})$, which behaves as if it was drawn from the density $\rho_{\mathbf{Z}}$. It is not difficult to generate pseudo-random samples from a uniform distribution, and the Rosenblatt transformation can then be used to generate samples from arbitrary densities [73].

The Rosenblatt transformation can be derived by considering the density decomposition of a multivariate random variable \mathbf{Z}

$$\rho_{\mathbf{Z}}(\mathbf{z}) = \prod_{d=0}^{D-1} \rho_{Z'_d}(z'_d), \quad (3.13)$$

where

$$Z'_d = Z_d | Z_0, \dots, Z_{d-1} \text{ and } z'_d = z_d | z_0, \dots, z_{d-1}, \quad (3.14)$$

which means that Z_d and z_d is dependent on every component with a lower

index. The forward Rosenblatt transformation can now be defined as

$$T_{\mathbf{Z}}(\mathbf{z}) = (F_{Z'_0}(z'_0), \dots, F_{Z'_{d-1}}(z'_{d-1})), \quad (3.15)$$

where $F_{Z'_d}$ is the cumulative distribution function:

$$F_{Z'_d}(z'_d) = \int_{-\infty}^{z_d} \rho_{Z'_d}(r|z_0, \dots, z_{d-1}) dr. \quad (3.16)$$

The inverse Rosenblatt transformation can be found in a similar way since the transformation is bijective¹ [73].

Practical use of the Rosenblatt transformation requires identification of the inverse Rosenblatt transformation $T_{\mathbf{Z}}^{-1}$. Since $T_{\mathbf{Z}}$ is often a non-linear function without a closed-form formula, analytical calculation of $T_{\mathbf{Z}}^{-1}$ could be intractable. Thus, we apply numerical methods to find $T_{\mathbf{Z}}^{-1}$. For further interest, we recommend the Chaospy article by Feinberg et al. [73].

3.1.6 APPROXIMATE MODELS

An option to reduce the computational cost of uncertainty quantification and sensitivity analysis is to use approximate models or metamodels. Consider the model described earlier in this chapter where we want to quantify the response Y

$$Y = f(\mathbf{Z}). \quad (3.17)$$

and we define an approximate model f_a so that $f_a \approx f$. The model error E_m of this approximation is given by

$$E_m = \frac{1}{N} \sum_{s=1}^N (\hat{y}^{(s)} - y^{(s)})^2 \quad (3.18)$$

where \hat{y} is the output of the approximate model f_a , y is the output of the native model f and N is the number of samples evaluated.

¹Bijective function ($y = f(x)$): one-to-one correspondence between x and y .

Similarly, the sensitivity error E_s is given by

$$E_p = \frac{1}{J} \sum_{j=1}^D \left((\hat{S}_j - S_j)^2 + (\hat{S}_{T,j} - S_{T,j})^2 \right) \quad (3.19)$$

where \hat{S} is the Sobol indices from the approximate model f_a , S is the Sobol indices from the native model f and D is number of uncertain input parameters.

3.2 FORWARD UNCERTAINTY ANALYSIS

As described earlier in this chapter, forward uncertainty analysis is the analysis of the uncertainty in our model output, given uncertain input parameters. Here, we outline the methods for forward uncertainty analysis used in this thesis. These methods include the MC method, two metamodels for UQ and SA, generalized PC and RF, and a method for local qualitative SA, the elementary effects (EE) method.

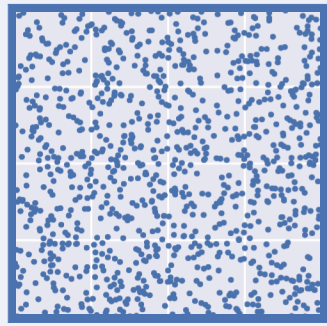
3.2.1 MONTE CARLO (MC) METHOD

The MC method is the most common way to find the mentioned uncertainty and sensitivity measures due to its simplicity and applicability to a broad range of problems. The MC method starts by using a sample method to draw a set of samples for the inputs, $\{\mathbf{z}^{(s)}\}_{s=1}^N$. The samples are drawn from an input space Ω_Z defined by the joint probability density function of the inputs, ρ_Z . A set of outputs $\{y^{(s)}\}_{s=1}^N$ is found by evaluating the deterministic model $f(\mathbf{z})$ for each sample in $\{\mathbf{z}^{(s)}\}_{s=1}^N$. All of the uncertainty measures and sensitivity indices mentioned can then be found directly from $\{y^{(s)}\}_{s=1}^N$.

Sampling schemes

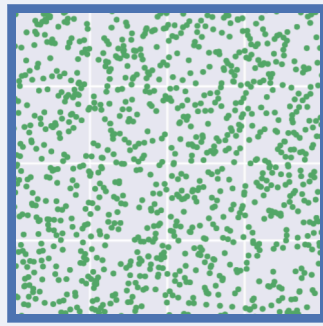
Pseudo-random sampling

Pseudo-random sampling is based on sequences of pseudo-random numbers. These sequences are widely available in modern packages for data analysis.



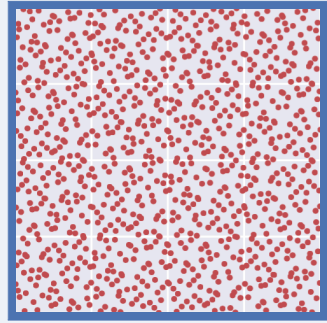
Latin Hypercube sampling

A Latin square is a square grid containing sample positions, where there is only one sample in each row and each column. Latin hypercube is the generalization of this for an arbitrary number of dimensions [88].



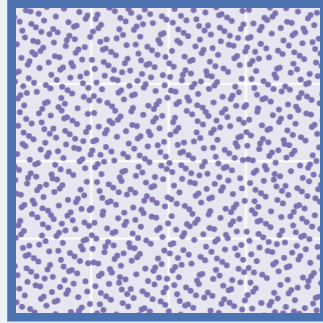
Sobol sampling

Sobol sequences use a base of two to form successively finer uniform partitions of the unit interval, before the coordinates are reordered in each dimension [89].



Halton sampling

The Halton sequence is constructed in accordance with a deterministic method which has bases consisting of coprime numbers [90].



Random sampling with the Monte Carlo method gives an asymptotic approximation error of σ_Y/\sqrt{N} [91]. This shows that the convergence rate is independent of the number of dimensions D , but might require very large N s for the asymptotic error estimate to be valid. Thus, it could be challenging or infeasible to find accurate estimates for computationally expensive models. It is possible to improve the convergence rate by using alternative sampling schemes. Examples of alternative sampling schemes are displayed in the text box above, and include Latin hypercube sampling [88] and quasi-random sampling methods [92]. These schemes improve sampling by preventing clustering of samples and ensure that the samples cover the entire input space [92].

Quasi-random sampling, also known as quasi-MC schemes, include methods such as Sobol and Halton sequences. The quasi-MC method consists of choosing samples $\{\mathbf{z}^{(s)}\}_{s=1}^N$ from a low-discrepancy sequence instead of a pseudo-random sequence. This is done to improve the coverage over the sample space, which makes it possible to reach a given accuracy with fewer samples [73].

3.2.1.1 MONTE CARLO: UNCERTAINTY QUANTIFICATION

From the evaluations of Y the expected value and variance can be estimated as

$$\mathbb{E}[Y] \approx \mathbb{E}_{MC}[Y] = \frac{1}{N} \sum_{s=1}^N y^{(s)}, \quad (3.20)$$

and

$$\mathbb{V}[Y] \approx \mathbb{V}_{MC}[Y] = \frac{1}{N-1} \sum_{s=1}^N (y^{(s)} - \mathbb{E}_{MC}[Y])^2. \quad (3.21)$$

3.2.1.2 MONTE CARLO: SENSITIVITY ANALYSIS

Using the MC method for estimating the main and total sensitivity indices requires a total number of $2DN^2$ evaluations. To reduce this number, Saltelli devised an alternative MC method that reduces the total number of evaluations

to $N(D + 2)$ [74, 93].

In Saltelli's efficient numerical procedure for estimating the main and total sensitivity indices, the first step is to create two independent sampling matrices, **A** and **B**. **A** consist of N samples $\mathbf{z}^{(s)} = [z_1^{(s)}, z_2^{(s)}, \dots, z_D^{(s)}]$, and **B** consist of $\mathbf{z}'^{(s)} = [z'_1^{(s)}, z'_2^{(s)}, \dots, z'_D^{(s)}]$. The second step is to use **A** and **B** to create a number of D matrices $\mathbf{C}_i, i = 1, 2, \dots, D$. In \mathbf{C}_i , all columns are taken from **B** except the i -th column, which comes from **A**. The third step involves calculating the model evaluations for each row in all of the sample matrices

$$y_A^{(s)} = f(\mathbf{A}^{(s)}), \quad y_B^{(s)} = f(\mathbf{B}^{(s)}), \quad y_{C_i}^{(s)} = f(\mathbf{C}_i^{(s)}) \quad (3.22)$$

where s denotes the s^{th} row in the matrices. The main sensitivity indices from Eq. 3.10 are then estimated as

$$S_i \approx \frac{U_i - \mathbb{E}_{MC}[Y]^2}{\mathbb{V}_{MC}[Y]}, \quad (3.23)$$

where

$$U_i = \frac{1}{N-1} \sum_{s=1}^N y_A^{(s)} y_{C_i}^{(s)}, \quad (3.24)$$

and the expected value and variance is estimated as

$$\mathbb{E}_{MC}[Y]^2 = \frac{1}{N} \sum_{s=1}^N y_A^{(s)} y_B^{(s)} \quad (3.25)$$

$$\mathbb{V}_{MC}[Y] = \frac{1}{N-1} \sum_{s=1}^N (y_B^{(s)})^2 - \mathbb{E}_{MC}[Y]^2. \quad (3.26)$$

For the total sensitivity indices in Eq. 3.12 we get

$$S_{T,i} \approx \frac{U'_i - \mathbb{E}_{MC}[Y]^2}{\mathbb{V}_{MC}[Y]}, \quad (3.27)$$

where

$$U'_i = \frac{1}{N-1} \sum_{s=1}^N y_B^{(s)} y_{C_i}^{(s)}, \quad (3.28)$$

and

$$\mathbb{E}_{MC}[Y]^2 = \left(\frac{1}{N} \sum_{s=1}^N y_A^{(s)} \right)^2, \quad (3.29)$$

$$\mathbb{V}_{MC}[Y] = \frac{1}{N-1} \sum_{s=1}^N (y_A^{(s)})^2 - \mathbb{E}_{MC}[Y]^2. \quad (3.30)$$

3.2.2 POLYNOMIAL CHAOS METHOD

The PC method is a metamodel method that can be used to approximate uncertainty and sensitivity measures. The PC method is based on Wiener's theory of homogeneous chaos [94], which gives optimal convergence for Gaussian stochastic processes. A generalized PC method has been developed later, which gives optimal convergence for more general stochastic processes as well. For simplicity, we will refer to the generalized PC method as the PC method throughout this thesis [95].

In the PC method, the model response Y is expanded into a series of orthogonal polynomials that are functions of the inputs \mathbf{Z} [96], where the orthogonal polynomials are basis functions which cover the output space. The method results in a polynomial chaos expansion that is an analytic expression which can be used to obtain the uncertainty and sensitivity measures with great simplicity [74].

The PC expansion is expressed in terms of the orthogonal polynomials and expansion coefficients. For functions with a small or moderate number of input parameters, the expansion coefficients can be calculated with a much lower number of samples compared with the MC method [80, 97]. This makes the PC method an excellent alternative to the MC method for many cases. In this thesis,

we use the PC implementation in the Chaospy toolkit [73].

3.2.2.1 POLYNOMIAL CHAOS EXPANSIONS

In the original PC method, Wiener represented a stochastic process through a spectral expansion using orthogonal polynomials as

$$Y = \sum_{j=0}^{\infty} c_j He_j(\mathbf{Z}), \quad (3.31)$$

where He_j is the Hermite polynomial of order j and c_j is the corresponding deterministic coefficient, which is calculated from a limited number of model simulations [95].

In the PC method, the polynomial of choice is based on the corresponding random variable, which builds on the principle that random processes can be approximated fairly good using orthogonal basis functions given by the Askey scheme (Table 3.2.1) in terms of the corresponding random variable. Inputs and outputs of the system under consideration are represented with series approximations using standard random variables. This results in computationally efficient methods for measuring uncertainty propagation in complex numerical models. The representation of the output is made up of the same random variables that are used to represent the input, which makes it possible to express the output in the form of a series expansion consisting of orthogonal polynomials in terms of the corresponding multi-dimensional stochastic variable. Thus, the expression of the output Y is given as

$$Y \approx f_{PC}(\mathbf{Z}) = \sum_{j=0}^{\infty} c_j \Phi_j(\mathbf{Z}), \quad (3.32)$$

where \mathbf{Z} is the multi-dimensional stochastic variable. Each dimension in Z consist of components that are independent and identically distributed (iid) and $\Phi_j(\mathbf{Z})$ is the generalized Askey-Wiener polynomial chaos of order j [95, 96].

For simplicity, it is common to truncate the series to a finite number of terms.

The expression of the output Y can then be rewritten to

$$Y \approx f_{PC}(\mathbf{Z}) = \sum_{j=0}^{N_p-1} c_j \Phi_j(\mathbf{Z}), \quad (3.33)$$

where $N_p = \binom{D+p}{p}$. Here D is the number of random variables and p is the maximum order of the polynomial basis functions [95].

The idea behind the pairing of the polynomial basis functions and the random variables is that the orthogonal polynomials of the Askey scheme have the weighting function in their orthogonality relation identical to the probability density function of the distribution of the corresponding stochastic variable [95, 96]. The correspondence between the random variables and polynomial basis functions is given in Table 3.2.1.

Askey scheme			
	Distribution of Z	gPC basis polynomials	Support
Continuous	Gaussian	Hermite	$(-\infty, \infty)$
	Gamma	Laguerre	$[0, \infty)$
	Beta	Jacobi	$[a, b]$
	Uniform	Legendre	$[a, b]$
Discrete	Poisson	Charlier	$0, 1, 2, \dots$
	Binomial	Krawtchouk	$0, 1, \dots, N$
	Negative binomial	Meixner	$0, 1, 2, \dots$
	Hypergeometric	Hahn	$0, 1, \dots, N$

Table 3.2.1: Correspondence between random variables and polynomial basis functions [84]

3.2.2.2 CALCULATION OF EXPANSION COEFFICIENTS

The PC expansion coefficients can be calculated either intrusively or non-intrusively. For calculations using intrusive methods, it is necessary to incorporate information about the underlying forward model f in the estimation of the expansion coefficients while non-intrusive methods only require the

information off for the computational procedures [73].

Intrusive calculation of the coefficients can be performed using the Galerkin projection method, where each state variable is projected onto the polynomial chaos basis. Finding the coefficients with an intrusive method can be nontrivial or even impossible for complex and nonlinear problem statements. However, it is important to keep in mind the accuracy of the different methods and that the Galerkin projection method ensures optimal accuracy. Nevertheless, for a complex system for which well-established deterministic codes exist, non-intrusive methods are most common [84, 95]. In this thesis, we use the Chaospy toolbox [73] which is well-supported for non-intrusive methods. Hence, we focus on non-intrusive methods for the rest of this thesis. For readers with a further interest in the Galerkin projection method, we recommend Xio's book *Numerical Methods for Stochastic Computations: A Spectral Method Approach* [84].

There are two commonly used approaches to estimate the PC expansion coefficients non-intrusively: pseudospectral projection and stochastic collocation. The former method uses the orthogonality of the polynomials and requires a numerical integration scheme where specific input samples have to be used while the latter solves a linear system that comes from a statistical regression formulation [73, 74]. A more thorough review of both methods will be given in the next paragraphs.

3.2.2.3 PSEUDOSPECTRAL PROJECTION

In the pseudospectral projection approach, also called spectral or discrete projection, each expansion coefficient c_j is found by projecting the solution onto the space spanned by the orthogonal polynomials with the inner product. With use of the orthogonality property

$$\int_{\Omega_z} \Phi_i \Phi_j \rho_z \, dz = \delta_{ij} H_i, \quad (3.34)$$

where δ_{ij} is the Kronecker delta and H_i is the normalization factor for the polynomial Φ_i , we can set up an expression for the expansion coefficients

$$c_j = \frac{1}{H_j} \int_{\Omega_Z} f(\mathbf{z}) \Phi_j(\mathbf{z}) \rho_{\mathbf{Z}}(\mathbf{z}) d\mathbf{z}. \quad (3.35)$$

A numerical integration scheme can now be used to approximate the integral. Since the integrands are smooth polynomials, they can be approximated fairly accurately with tensor or sparse grid quadrature [74]. The approximated expression for c_j is then

$$c_j \approx \frac{1}{H_j} \sum_{j=1}^N f(\mathbf{z}^{(s)}) \Phi_j(\mathbf{z}^{(s)}) w_s, \quad (3.36)$$

where w_s are weights and $\mathbf{z}^{(s)}$ are nodes in a quadrature scheme. In tensored quadrature methods, the number of samples is $N = (N_{1D})^D$, where N_{1D} is the number of nodes in the one-dimensional quadrature rule. Thus, the number of samples, N , will become very large for large D s, and it can therefore be problematic to use this method for higher-dimensional problems. Luckily, this problem can be solved with sparse grid quadrature. Sparse grid quadratures are constructed from one-dimensional quadrature rule using Smolyak's algorithm [98]. When using the same one-dimensional quadrature rule, N for the sparse quadrature is less than for the tensored quadrature. Unfortunately, an additional approximation error is also introduced [73, 74].

3.2.2.4 STOCHASTIC COLLOCATION METHOD

The stochastic collocation method, also referred to as the point collocation- or regression method, minimizes a normed difference between the polynomial chaos expansion and the model evaluations at a set of collocation nodes. This can

be expressed as the solution of

$$\arg \min_c \left\| f(\mathbf{Z}) - \sum_{j=0}^{N_p-1} \mathbf{c}_j \Phi_j(\mathbf{Z}) \right\|, \quad (3.37)$$

where any norm L^q given by $\|(\cdot)\|_q = (\sum(\cdot)^q)^{\frac{1}{q}}$ can be used. For a L^2 -norm we will get the following linear least squared problem

$$\mathbf{A}\mathbf{c} = \mathbf{y}, \quad (3.38)$$

where

$$\mathbf{A} = \Phi_j(\mathbf{z}^{(s)}), \quad 0 \leq j \leq N_p - 1, \quad 1 \leq s \leq N \quad (3.39)$$

$$\mathbf{c} = \mathbf{c}_j, \quad 0 \leq j \leq N_p - 1 \quad (3.40)$$

$$\mathbf{y} = f(\mathbf{z}^{(s)}), \quad 1 \leq s \leq N. \quad (3.41)$$

It is necessary that the number of samples, N , is equal or greater than the number of expansion coefficients N_p . To obtain a good least squares optimazation it is recommended to use at least $N = 2N_p$ [74], which will give you an overdetermined system where the best approximation for \mathbf{c} is given by

$$\mathbf{c} = (\mathbf{A}^T \mathbf{A})^{-1} \mathbf{A}^T \mathbf{y}. \quad (3.42)$$

Any sampling scheme that covers the entire input domain can be used to obtain the samples. This leads to a required number of samples that is less than what would be needed for the pseudospectral approach, especially for higher-dimensional problems [74].

3.2.2.5 POLYNOMIAL CHAOS: UNCERTAINTY QUANTIFICATION

From a polynomial chaos expansion, the statistical moments can be found directly by use of the orthogonality property in Eq. 3.34 and the zero-mean

property

$$\mathbb{E}[\Phi_j] = \int_{\Omega_z} \Phi_j(\mathbf{z}) \rho_{\mathbf{Z}}(\mathbf{z}) dZ_i = \begin{cases} 0, & j \neq 0 \\ 1, & j = 0 \end{cases} \quad (3.43)$$

From the definitions of the statistical moments in section 3.1.2 we get that the expected value is given by

$$\mathbb{E}[\mathbf{Y}] \approx \mathbb{E}_{PC}[\mathbf{Y}] = \int_{\Omega_z} \sum_{j=0}^{N_p-1} c_j \Phi_j(\mathbf{z}) \rho_{\mathbf{Z}} d\mathbf{z} = c_0, \quad (3.44)$$

and the variance is given by

$$\begin{aligned} \mathbb{V}[Y] \approx \mathbb{V}_{PC}[Y] &= \mathbb{E} [(f_{PC}(\mathbf{Z}) - \mathbb{E}_{PC}[\mathbf{Y}])^2] \\ &= \int_{\Omega_z} (f_{PC}(\mathbf{z}) - c_0)^2 \rho_{\mathbf{Z}}(\mathbf{z}) d\mathbf{z} \\ &= \int_{\Omega_z} \left(\sum_{j=0}^{N_p-1} c_j \Phi_j(\mathbf{z}) \right)^2 \rho_{\mathbf{Z}}(\mathbf{z}) d\mathbf{z} - c_0^2 \\ &= \sum_{j=0}^{N_p-1} c_j^2 \int_{\Omega_z} \Phi_j^2(\mathbf{z}) \rho_{\mathbf{Z}}(\mathbf{z}) d\mathbf{z} - c_0^2 \\ &= \sum_{j=0}^{N_p-1} c_j^2 H_j - c_0^2 = \sum_{j=1}^{N_p-1} c_j^2 H_j. \end{aligned} \quad (3.45)$$

3.2.2.6 POLYNOMIAL CHAOS: SENSITIVITY ANALYSIS

The main and total sensitivity indices can be found directly using the PC expansion. For this purpose, it is beneficial to introduce the multi-indices $\alpha = (\alpha_1, \dots, \alpha_D)$, which can be used to construct Φ from univariate polynomials

$\Phi(Z_i)$ with tensor products

$$\Phi_{\alpha}(\mathbf{Z}) = \prod_{i=1}^D \Phi_{\alpha_i}(Z_i), \quad (3.46)$$

where Φ_{α_i} is the univariate polynomial of order α_i . This relation can be used to express the truncated polynomial chaos expansion of an output as

$$Y \approx f_{PC}(\mathbf{Z}) \sum_{\alpha \in \mathcal{A}} c_{\alpha} \Phi_{\alpha}(\mathbf{Z}), \quad (3.47)$$

where \mathcal{A} is the set of $N_p = \binom{D+p}{p}$ multi-indices α for all polynomials with a maximal order p [74, 80].

Using α , the variance expressed in section 3.2.2.5, be expressed as

$$\mathbb{V}[Y] \approx \mathbb{V}_{PC}[Y] = \sum_{\alpha \in \mathcal{A}} \mathbb{V}[c_{\alpha} \Phi_{\alpha}(\mathbf{Z})] = \sum_{\alpha \in \mathcal{A}} c_{\alpha}^2 H_{\alpha}. \quad (3.48)$$

By using $\mathbb{V}[Y]$, the main sensitivity index can be approximated by

$$S_i \approx \frac{1}{\mathbb{V}_{PC}[Y]} \sum_{\alpha \in \mathcal{A}_i} \mathbb{V}[c_{\alpha} \Phi_{\alpha}], \quad (3.49)$$

where

$$\mathcal{A}_i = \{\alpha \mid \alpha_i > 0 \wedge \alpha_j = 0 \forall j \neq i\}, \quad (3.50)$$

and the total sensitivity index can be approximated as

$$S_{T,i} \approx \frac{1}{\mathbb{V}_{PC}[Y]} \sum_{\alpha \in \mathcal{A}_{T,i}} \mathbb{V}[c_{\alpha} \Phi_{\alpha}], \quad (3.51)$$

where

$$\mathcal{A}_{T,i} = \{\alpha \mid \alpha_i > 0\}. \quad (3.52)$$

3.2.3 RANDOM FOREST (RF) METAMODEL

As described earlier in this chapter, UQ and SA can be performed using metamodels. The main reason for using metamodels, also referred to as emulators or surrogate models, is to speed up the computational procedure. Despite this, several of the most popular metamodels for UQ and SA show poor scalability to high-dimensional problems [99].

With a steady-growing complexity of computational models, an interesting question for future research is the investigation of methods for SA with sufficient accuracy and computational efficiency in high-dimensional input spaces. One way to achieve this is to utilize metamodels with good predictive capabilities in high-dimensional spaces. Provided that the computational performance of the metamodel is much higher than the original model, variance-based sensitivity analysis can be performed on the metamodel using the method described by Saltelli et al. [93]. Thus, Sobol indices in high-dimensional spaces can be obtained using a three-step method

1. Sample from the original model.
2. Train the metamodel using the obtained samples.
3. Calculate the Sobol indices using Monte Carlo sampling from the trained metamodel.

In this thesis, we use the term Generalized Metamodel Sensitivity Analysis (GMSA) to describe the three-step method for SA outlined in this paragraph.

An interesting class of metamodels for GMSA is machine learning algorithms. Machine learning is a subfield of computer science, which aims to construct algorithms that can learn from and make predictions on data. Several authors have investigated the feasibility of machine learning metamodels for GMSA. For example, results from Li et al. show that an artificial neural network² metamodel can give a good approximation of parameter sensitivity [100]. Further,

²Neural network: Neural networks are a family of machine learning models inspired by biological neural networks.

Sathyaranayananurth et al. [101] investigated several machine learning metamodels and found that the metamodels gave accurate approximations of parameter sensitivity, provided that proper care is taken to avoid issues like overfitting³. In this work, we use GMSA based on the random forest algorithm to approximate Sobol indices. This is similar to the approach by Storlie et al. [102] that utilized GMSA to estimate variance-based sensitivity for a broad range of nonparametric regression procedures, including RF. Their result showed that a RF metamodel was able to give good qualitative sensitivity indices, but with some inaccuracies in their absolute values.

3.2.3.1 RANDOM FOREST (RF)

RF is a notion of the general method of random decision forests, which are an ensemble learning method for classification and regression [103, 104]. An ensemble method is a method that uses several learning algorithms to obtain better predictive performance than a constituent learning algorithm [105]. The random decision forest method has its name from the fact that it constructs multiple decision trees. For regression, the decision trees are built at training time, and prediction is given by an ensemble average of the trees. A more detailed description of the RF algorithm is provided in *Random forests* by Breiman [106]. An advantage of the random decision forests is that it corrects for decision trees habit of overfitting to their training set. It is also known to give accurate prediction with a minimum of required tuning [107]. The main steps in the RF algorithm are outlined in the text box below.

³Overfitting: A statistical model is overfitted when it describes random noise instead of the underlying relationship.

Random Forest Algorithm

- A training set is created by taking a subset of the entire dataset.
- Several decision trees are created by clustering of data into groups and subgroups.
- At each split of a decision tree, variables are chosen at random to determine the relationship between data points (Note that due to the random choice of variables, all decision trees will be different).
- A cross-validation procedure is used to find which decision trees gives the highest predictive performance.
- The output of the algorithm will be an ensemble average of the chosen decision trees.

3.2.3.2 RANDOM FOREST: UNCERTAINTY QUANTIFICATION AND SENSITIVITY ANALYSIS

In this work, we use GMSA to approximate the Sobol indices from the RF metamodel. The choice of a RF metamodel is based on two important characteristics. First, the RF algorithm is recognized by its ability to yield accurate prediction with small sample sizes and high-dimensional feature spaces [108]. Second, a recognized feature of the RF algorithm is the high computational efficiency during prediction [109]. Despite this, limited research exists on the connection between metamodel predictive accuracy and accuracy of the estimated Sobol indices. Therefore, the RF-based GMSA method is benchmarked against conventional methods on lower-dimensional problems in Chapter 4.

3.2.4 ELEMENTARY EFFECT (EE) SCREENING

Screening methods provide an alternative to variance-based methods for sensitivity analysis for models with high-dimensional input spaces or models whose computational expense prohibits construction of Sobol indices. The goal of screening methods is to rank input parameters according to their importance, but unlike variance-based methods, they are typically unable to provide a quantitative measure of the relative input sensitivities. An in-depth presentation of screening methods and EE screening can be found in *Uncertainty Quantification: Theory, Implementation, and Applications* by R. Smith [72].

Screening methods are in the class of One Factor at a Time (OAT) methods. OAT methods quantify the variation in output as inputs are varied individually. While OAT methods provide a local measure of the input sensitivity, EE screening averages over local derivative approximations to provide a pseudo-global sensitivity measure.

3.2.4.1 THE ORIGINAL EE METHOD

The philosophy of the original EE method by Morris et al. [110] was to determine which input factors may be considered to be (a) negligible, (b) linear and additive, or (c) non-linear. Consider a mathematical model f with p input factors

$$y = f(\mathbf{z}), \quad (3.53)$$

where $\mathbf{z} = [z_1, z_2, \dots, z_p]$ and each input parameters are uniformly distributed and scaled to the interval $[0, 1]$. The concept of Morris screening is to average local sensitivity approximations called elementary effects d_i

$$\begin{aligned} d_i(\mathbf{z}) &= \frac{f(z_1, \dots, z_{i-1}, z_i + \Delta, z_{i+1}, \dots, z_p) - f(\mathbf{z})}{\Delta} \\ &= \frac{f(z + \Delta e_i) - f(\mathbf{z})}{\Delta}, \end{aligned} \quad (3.54)$$

where Δ is the step size. Thus, the computation of elementary effects are based on a linearization of the model. The elementary effects $d_i(z)$ quantifies the approximate sensitivity behavior at the point \mathbf{z} . To provide a pseudo-global sensitivity measure, one approximate the mean and variance of r sampled elementary effects for each input variable

$$\mu_i^* = \frac{1}{r} \sum_{j=1}^r |d_i^j(\mathbf{z})| \quad (3.55)$$

$$\sigma_i^2 = \frac{1}{r-1} \sum_{j=1}^r (d_i^j(\mathbf{z}) - \mu_i)^2 \quad (3.56)$$

$$\mu_i = \frac{1}{r} \sum_{j=1}^r d_i^j(\mathbf{z}) \quad (3.57)$$

For distributions with elementary effects of both positive and negative values, μ_i^* is a preferred metric over μ_i . μ_i^* quantifies the individual effect of the input on the output while σ_i quantifies the combined effects of non-linearities and interactions with other inputs [72].

For efficient computation of the elementary effects, the input space is partitioned into l -levels, which restricts the input to a D -dimensional grid and a total of l^D grid values. The step size is chosen from the set

$$\Delta \in \left\{ \frac{1}{l-1}, \frac{2}{l-1}, \dots, 1 - \frac{1}{l-1} \right\}, \quad (3.58)$$

where the number of l levels is assumed to be greater than 3. An example of a partitioned input space with 5 l -levels and two trajectories are seen in Figure 3.2.1.

The goal for the choice of the parameters l and Δ is to get the best possible coverage over the input space. Campolongo et al. [111] suggested the following

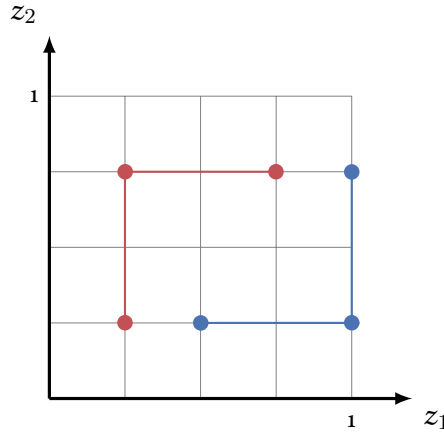


Figure 3.2.1: Five-level grid ($l = 5$) for $\mathbf{z} = [z_1, z_2]$ with $\Delta = \frac{1}{2}$ and two trajectories (blue and red).

relationship

$$\Delta = \frac{l}{2(l-1)}, \quad (3.59)$$

where a certain symmetric coverage of the input space is ensured.

3.2.4.2 THE EXTENDED EE METHOD

The original EE method is based on random sampling of trajectories in the input space. To keep the computational cost at a minimum, we want to minimize the number of trajectories. Using random sampling, this could lead to non-optimal coverage of the input space. Several improved sampling strategies have been proposed in the literature. For example, Campolongo et al. [111] proposed an improved sampling strategy which aims at improving the coverage of the input space without increasing the number of necessary function evaluations. For convenience, we sample the trajectories using the original version of the EE method. Thus, it is reasonable to believe that improved sampling strategies for the EE method will give a faster convergence than seen in this work.

Also, the original EE method was proposed for uniformly distributed random

variables on a normalized interval between 0 and 1. To extend the method to non-uniformly distributed random variables, we map the EE trajectories from the unit-cube to the sample space using the inverse cumulative distribution function and the inverse Rosenblatt-transform described in Section 3.1.5

3.3 BACKWARD UNCERTAINTY ANALYSIS: BAYESIAN INFERENCE

As described earlier in this chapter, backward propagation of uncertainty is used to infer probability distributions of uncertain input parameters given observed model output. For backward uncertainty problems, Bayesian inference offers a convenient probabilistic framework to infer the probability distributions of uncertain input variables.

Bayesian inference is a method in statistics where uncertainty is expressed in terms of probability. In a Bayesian inference problem, we start by formulating an appropriate model for the situation of interest with some unknown parameters $\boldsymbol{\theta}$. For each of the unknown parameters, a prior probability distribution $p(\boldsymbol{\theta})$ which expresses our initial beliefs is formulated. Given some data \mathbf{X} , Bayes' theorem is used to update the probability of our hypothesis and is expressed by

$$p(\boldsymbol{\theta}|\mathbf{X}) = \frac{p(\mathbf{X}|\boldsymbol{\theta})p(\boldsymbol{\theta})}{p(\mathbf{X})}. \quad (3.60)$$

Bayes' theorem enables us to evaluate the posterior distribution $p(\boldsymbol{\theta}|\mathbf{X})$ which is the uncertainty of $\boldsymbol{\theta}$ after we have observed \mathbf{X} . Thus, the posterior distribution takes into account both the data and our prior distribution [112].

The quantity $p(\mathbf{X}|\boldsymbol{\theta})$ on the right side of Bayes' theorem is called the *likelihood function*. The likelihood function expresses how probable the observed data is for a given setting of the function parameters $\boldsymbol{\theta}$. Thus, Bayes' theorem states that

$$\text{posterior} \propto \text{likelihood} \cdot \text{prior}, \quad (3.61)$$

where the posterior is a function of \mathbf{X} and $\boldsymbol{\theta}$. The denominator $p(\mathbf{X})$ in Equation 3.60 is called the normalization constant and ensures that the posterior

distribution is a valid probability distribution and integrates to one. The normalization constant can be expressed in terms of the prior distribution and the likelihood function, and is given by the integral

$$p(\mathbf{X}) = \int p(\mathbf{X}|\boldsymbol{\theta})p(\boldsymbol{\theta}) d\boldsymbol{\theta}. \quad (3.62)$$

Bayesian analysis has an advantage over classical frequency analysis when it comes to small sets of data. This is because Bayesian inference preserves the uncertainty that reflects the instability of statistical inference, which happens when we introduce a prior distribution and return probabilities as we require more data [112]. Also, Bayesian analysis offers convenient tools to infer distributions of unobserved model parameters, often called hidden or latent variables [78].

3.3.1 PRIOR DISTRIBUTIONS

The outcome in Bayesian regression is strongly influenced by the choice of the prior distribution. Accordingly, an appropriate prior function is critical, and it is the most debated and discussed aspect of Bayesian methods [113].

Prior distributions can be divided into two classes: subjective- and objective priors. Subjective priors allow the prior distribution to influence the posterior distribution and might be used when the assessor has prior knowledge about the shape and/or location of the posterior distribution. On the other hand, an objective prior ensure that the posterior distributions are only influenced by the data. Thus, an objective prior is often the preferred choice for science and research applications.

According to Gelman et al. [114], a uniform distribution with large bounds is often a good choice for an objective prior. Unfortunately, these priors should be applied with caution since uniform objective priors with large bounds can give unrealistic prior probabilities to non-intuitive points. Thus, some authors suggest that a normal random variable with large variance or an exponential with a tail in the positive or negative direction might be a better choice in many cases [112].

Nonetheless, a uniform prior with large bounds might seem like a reasonable objective prior since it assigns equal probability to all values. However, a uniform prior is not a perfect objective prior. The reason for this is that a uniform prior is not necessarily transformational invariant [112]. Common choices to get around this problem is to use Jeffreys [115] or reference priors [116], which are transformation invariant objective priors. For multidimensional parameters, reference priors are the preferred choice in literature. The idea behind reference priors is to formalize what we mean by objective priors. We say that as we create data observations, a reference prior is a distribution that maximizes a measure of distance or divergence between the prior and the posterior. Reference priors allow the data to have maximum effect on the posterior estimates. Any divergence measures can be chosen. In this thesis, we use the Kullback-Liebler divergence [117] to calculate the divergence between the prior and posterior of our parameters θ . It should also be mentioned that even significantly wrong prior distributions will eventually give correct posteriors as the sample size increases, as long as the areas of non-zero probabilities are the same [112].

3.3.2 BAYESIAN HIERARCHICAL MODELING

A Bayesian hierarchical model is a statistical multi-level model which is used to infer parameters of the posterior distributions using Bayesian inference. The hierarchical model has observable outcomes modeled conditionally on certain parameters, where the parameters themselves are given a probabilistic specification in terms of other parameters, called hyperparameters. A hyperparameter is given by a probability distribution, normally referred to as a hyperprior. To find the posterior distribution, the hierarchical model is constructed of all sub-levels and Bayes rule is used to account for the present uncertainty and integrate the sub-levels with the observed data. For more information about hierarchical models we recommend reading chapter 5 in Gelman's book *Bayesian Data Analysis* [118].

3.3.3 MARKOV CHAIN MONTE CARLO (MCMC)

The key difficulty with Bayes' formula is that in general, no closed-form solution of the posterior is available, except in particularly trivial cases. Thus, to infer the probability distribution of uncertain input parameters, we have to rely on approximate solutions of the posteriors. For Bayesian inference with intractable posteriors, the MCMC method is extremely valuable. The reason for this is that we can construct a reversible Markov chain with an equilibrium distribution equal to the target posterior distribution [119]. We explain the practical meaning of this statement in the following paragraphs. MCMC is a large field of research, and we will only give a short introduction in this chapter. For further interest, we recommend the work by Geyer, *Introduction to Markov Chain Monte Carlo* [119].

3.3.3.1 MARKOV CHAINS

A Markov chain is a specific type of stochastic process, which is an ordered collection of random variables. A stochastic process is given by

$$\{Z_k : k \in K\}, \quad (3.63)$$

where K is the state space. The Markov chain is a sequence of random quantities Z_k , each obtaining values in the state space K , with the following dependence condition on each state Z_k

$$\begin{aligned} p(Z_{k+1} = z_{k+1} | Z_k = z_k, Z_{k-1} = z_{k-1}, \dots, Z_0 = z_0) \\ = p(Z_{k+1} = z_{k+1} | Z_k = z_k). \end{aligned} \quad (3.64)$$

This condition says that the future state only depends on the current state, such that all past states are irrelevant. The "memorylessness" of a Markov chain is called the Markov property.

The joint distribution of a Markov chain is determined by the initial distribution which is the marginal distribution of Z_1 and the transition probability distribution which is the conditional distribution of Z_{k+1} given Z_k .

Under certain requirements, the Markov chain will converge to an equilibrium distribution. The essence of Bayesian MCMC is to construct a Markov chain which fulfills these requirements and converges to the target posterior distribution. These requirements will be explained in the section below.

3.3.3.2 REQUIREMENTS

The first requirement for the Markov chain is stationarity. A Markov chain is stationary if it is a stationary stochastic process, where a stochastic process is stationary if for any positive integer m the distribution of the m -tuple $(Z_{k+1}, \dots, Z_{k+m})$ is independent of k . In a Markov chain we know that the conditional distribution of $(Z_{k+2}, \dots, Z_{k+m})$ given Z_{k+1} is independent of k . Thus, the Markov chain is stationary if and only if the marginal distribution of Z_k is independent of k . If the Markov chain specified by an initial distribution and a transition probability is stationary, we say that the initial distribution is stationary, invariant or the equilibrium distribution. This is also indicated by saying that the initial distribution is preserved by the transition probability distribution [119].

Another important requirement is reversibility. A Markov chain is reversible if its transition probability is reversible with respect to its initial distribution. This is the case if the Markov chain Z_1, Z_2, \dots specified by the initial distribution and transition probability distribution has an exchangeable distribution of pairs (Z_i, Z_{i+1}) . Hence, for any i and m the distributions of $(Z_{i+1}, \dots, Z_{i+m})$ and $(Z_{i+m}, \dots, Z_{i+1})$ are the same for a reversible Markov chain. Reversibility is important because all known methods for constructing transition probability mechanisms that preserve a specified equilibrium distribution are reversible [119].

3.3.3.3 MCMC METHODS

The two most common methods for MCMC are the Metropolis-Hastings algorithm and Gibbs sampling. In this thesis, the MCMC method will be performed using the Metropolis-Hastings algorithm.

3.3.3.4 METROPOLIS-HASTINGS UPDATE ALGORITHM

Metropolis-Hastings update algorithm is the original MCMC method and was first applied Metropolis et al. [120] in 1953 to a statistical physics problem. Despite a large variety of new MCMC methods, the original Metropolis-Hastings is still a widely used update algorithm today. In this thesis, the Metropolis-Hastings algorithm is implemented using the *Pymc* library [121].

Metropolis-Hastings update

- For a current state z , propose a move to y which has a conditional probability density denoted $q(y|z)$.
- Calculate the Hastings ratio

$$r(z, y) = \frac{h(y)q(y|z)}{h(z)q(z|y)}. \quad (3.65)$$

- Accept the proposed move y with probability

$$a(z, y) = \min(1, r(z, y)), \quad (3.66)$$

such that the value of the state after the update z_{k+1} , for a current state z_k with a proposed state y_k , is given by

$$z_{k+1} = \begin{cases} y_k, & \min(1, r(z_k, y_k)) \\ z_k, & 1 - \min(1, r(z_k, y_k)). \end{cases} \quad (3.67)$$

Suppose that the wanted stationary distribution of the constructed MCMC sampler has an unnormalized density h , such that h is a positive constant times a probability density. Thus, h is a nonnegative-valued function that integrates or sums to a finite, nonzero value for a continuous or discrete state, respectively.

Here, h gives the probability of some data and is given by Bayes' rule (Eq. 3.60). It will only be necessary to calculate the nominator, here for the proposed state

$$h(y) = p(x|y)p(y) \quad (3.68)$$

where $p(x|y)$ is the likelihood function for x given y and $p(y)$ is the prior distribution of the proposed state. The denominator will be equal for all states and cancel out in the Hastings ratio. Further, an arbitrarily chosen proposal distribution q is used to propose the next state in the update mechanism [119]. A further description of the Metropolis-Hastings update algorithm is given in the text box above.

Note that the Hastings ratio r is undefined if $h(z) = 0$. Thus, it is essential to arrange that $h(z) > 0$ in the initial state. Also, a more justified choice of the proposal distribution q might be beneficial, since it determines how fast the chain converges [119, 122].

3.4 SUMMARY

In this thesis, UQ and SA are used to analyze uncertainty in CT_{FFR} models. In this chapter, the governing theory of UQ and SA is presented. First, we outline the two principal types of uncertainty problems, forward propagation of uncertainty and backward propagation of uncertainty. In forward propagation of uncertainty, we want to quantify the uncertain response of our model given uncertain input parameters. Hence, we introduce relevant tools for UQ and SA. These tools include MC, PC, the RF metamodel, and the EE method. The choice of method for forward propagation of uncertainty depends on the required accuracy, computational complexity and the number of model input parameters.

In backward propagation of uncertainty, the uncertainty of input parameters is inferred using the measured model output. Here, we present the Bayesian framework for backward uncertainty analysis. In particular, we describe the MCMC Metropolis-Hastings algorithm used to infer the posterior distributions of uncertain parameters.

Probability theory is nothing but common sense reduced to calculation.

Pierre-Simon Laplace

4

Application of Uncertainty Quantification and Sensitivity Analysis to CT_{FFR}

In this chapter, we perform uncertainty quantification (UQ) and sensitivity analysis (SA) of CT_{FFR} with respect to physiological parameters. This analysis includes UQ and global variance-based SA of all parameters of interest. Also, we investigate methods for quantitative and qualitative SA in CT_{FFR} models. A major challenge for applications of sensitivity analysis in CT_{FFR} models is the combination of a vast number of input parameters and high computational costs. Thus, we evaluate methods for sensitivity analysis based on criteria for accuracy and computational efficiency. An in-depth presentation of these methods is given in Chapter 3.

4.1 PARAMETER UNCERTAINTY IN SINGLE STENOSIS

In the first experimental case, the effect of parameter uncertainty on FFR over a single stenosis is investigated. The estimation of FFR is based on the single stenosis model proposed by Huo et al. [44] as described in Section 2.1.3.3.

In the Huo model, flow rate, arterial pressure, stenosis diameter, dynamic viscosity, and density are considered uncertain parameters. These parameters are set to clinically relevant values as specified in Section 2.2.3 and modeled with an uncertainty of $\pm 5\%$ (uniformly distributed random variables $\mathcal{U}(0.95\mu, 1.05\mu)$, where μ is the mean value of the uncertain parameter). The aim of the experiment is to investigate relative effects of input uncertainties and compare the performance of different methods for quantitative and qualitative sensitivity analysis, hence, we use the arbitrarily chosen uncertainty of $\pm 5\%$. A full description of model parameters and parameter uncertainty is given in Table 4.1.1.

Variables	Symbol	Unit	Value	Uncertainty
Flow rate	Q	mL/min	350	± 5
Arterial Pressure	P_a	$mmHg$	90	± 5
Dynamic viscosity, blood	μ	$Pa \cdot s$	$3.5 \cdot 10^{-3}$	± 5
Density, blood	ρ	kg/m^3	1050	± 5
Stenosis diameter	d_s	mm	2	± 5
Stenosis length	l_s	mm	3	± 5
Vessel diameter	d_v	mm	4	0
Vessel length	l_v	mm	10	0

Table 4.1.1: Absolute values and relative uncertainty for parameters in simulations using the single stenosis model.

4.1.1 UNCERTAINTY QUANTIFICATION

4.1.1.1 EXPERIMENTAL SETUP

In this experiment, we perform UQ of FFR with respect to the input uncertainties presented in Table 4.1.1. The uncertainty is quantified using MC sampling. To improve convergence and minimize the number of function evaluations, the MC sampling is performed using Latin Hypercube sampling as described in Section 3.2.1. The MC sampling is done using 5000 model evaluations.

4.1.1.2 RESULTS

The result from the UQ shows that the uncertainty in the input parameters results in an FFR with a mean $\mu = 0.818$ and standard deviation $\sigma = 0.0267$. From Figure 4.1.1, we see that the uncertainty has a notable impact on the resulting FFR and that the resulting non-symmetric distribution shows a clear long-tail behavior in the direction of decreasing FFR values.

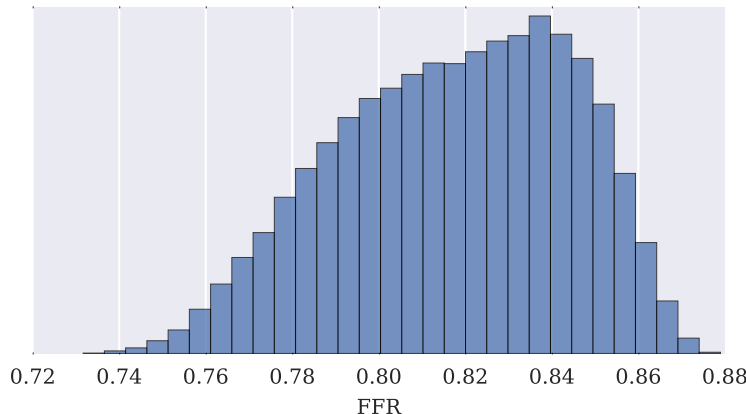


Figure 4.1.1: Histogram showing the distribution of FFR from MC sampling with 5000 model evaluations. The distribution of FFR is a result of uncertainty of input parameters and is characterized by a mean $\mu = 0.818$ and a standard deviation $\sigma = 0.0267$.

4.1.2 VARIANCE-BASED SENSITIVITY ANALYSIS

4.1.2.1 EXPERIMENTAL SETUP

In this experiment, we quantify the sensitivity of FFR with respect to the input parameters using MC, PC, sparse PC and the RF metamodel. The goal of this procedure is to investigate the sensitivity of FFR with respect to input parameters and compare the accuracy of methods for variance-based sensitivity analysis. Also, we do a visual presentation of the relationship between input parameters and FFR using MC sampling.

The MC method for variance-based sensitivity analysis is presented in Section 3.2.1.2. In this experiment, MC with a high number of samples ($N = 10^6$) serves as a ground truth for the Sobol sensitivity indices. We compare the sensitivity indices obtained from MC to the sensitivity indices obtained from PC and the RF metamodel using GMSA, which is described in Section 3.2.2 and Section 3.2.3, respectively. Pseudospectral PC (Section 3.2.2.3) is performed with a Gaussian quadrature- and polynomial order 3. For a fair comparison, the number of samples used to train the RF metamodel is set equal to the number of model evaluations used for PC. As described in Section 3.2.2.3, the number of necessary model evaluations for PC is determined by the order of the Gaussian quadrature. Furthermore, the sensitivity indices obtained from MC are compared to the sensitivity indices obtained from sparse PC as described in Section 3.2.2.3. As PC, sparse PC is performed with a quadrature- and polynomial order 3. The sensitivity indices from the sparse PC analysis are compared to the sensitivity indices obtained from the random forest metamodel using an equivalent number of model evaluations.

4.1.2.2 RESULTS

Figure 4.1.2 shows a scatter plot of the relationship between the input parameters and the resulting FFR. Visually, we see that the stenosis diameter d_s shows a strong correlation with FFR. Moreover, we identify a weak correlation between FFR and the flow rate Q and arterial pressure P_a . Stenosis length, dynamic

viscosity, and density show no clear relationship to the resulting FFR.

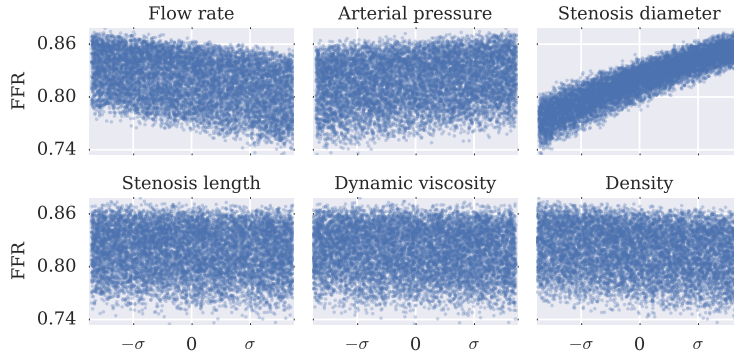


Figure 4.1.2: The relationship between input parameters and FFR from 10^4 MC samples. The graphical presentation of the input variables is normalized with a mean 0 and standard deviation σ .

The result from the variance-based sensitivity analysis can be seen in Figure 4.1.3. The figure shows the Sobol indices for MC, PC, sparse PC and the RF metamodel. In Figure 4.1.3a, the ground truth sensitivity indices are compared to sensitivity indices from PC and the RF metamodel using an equivalent number of model evaluations ($N = 4096$). In Figure 4.1.3b, the ground truth sensitivity indices are compared to the sensitivity indices from sparse PC and the RF metamodel using a lower number of model evaluations, $N = 389$ vs. $N = 4096$ (sparse vs. conventional). The figures show that the diameter of the stenosis d_s is the most vital input parameter. Also, we see that the sensitivity indices from the PC methods, both conventional and sparse, are similar to the ground truth sensitivity indices. The RF metamodel tends to over-estimate the sensitivity indices for the most significant parameters and under-estimate the sensitivity indices for the less critical parameters. Despite this, the RF metamodel gives a good quantitative approximation of the Sobol sensitivity indices.

A quantitative comparison between PC and the RF metamodel is seen in Table 4.1.2. We see that there is an excellent agreement between the methods and

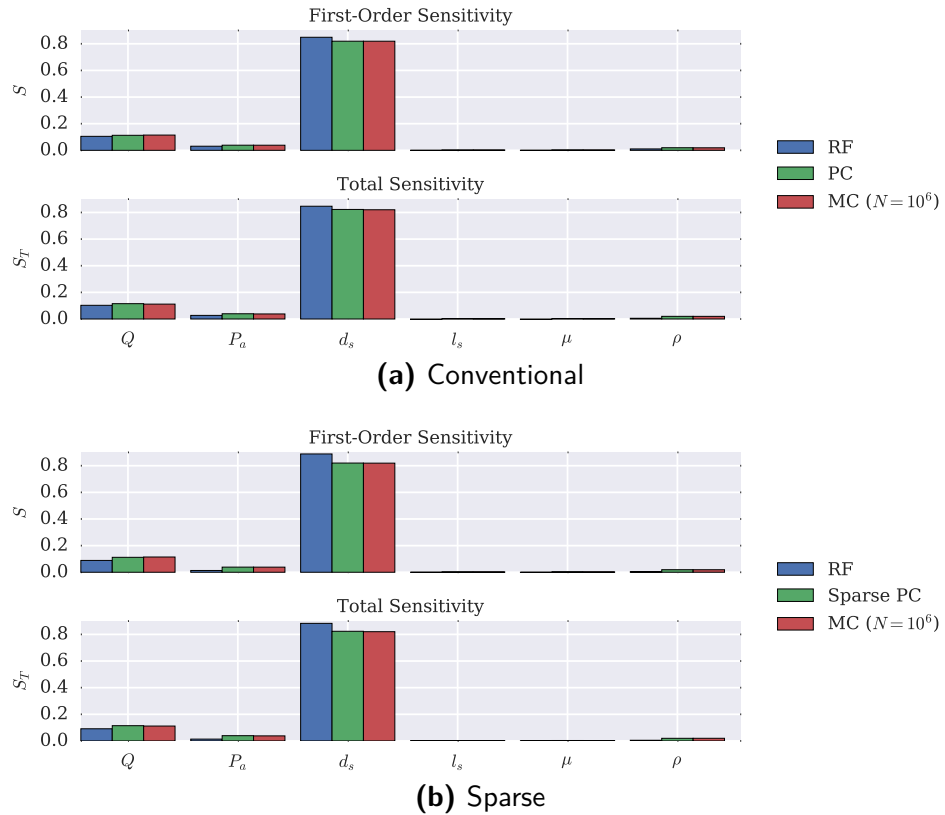


Figure 4.1.3: First order Sobol sensitivity indices S and total Sobol sensitivity indices S_T for the RF metamodel and conventional PC (a) and the RF metamodel and sparse PC (b). In both cases, the Sobol sensitivity indices are calculated using the same number of model evaluations, 4096 and 389 for the conventional and sparse PC method, respectively.

observe a strong correlation between model errors and sensitivity errors. Overall, we see that the PC methods show lower errors compared to the RF metamodel, both regarding the model error and sensitivity error.

Method	N	E_m	E_s
Random Forest Metamodel	4096	$2.31 \cdot 10^{-5}$	$7.55 \cdot 10^{-4}$
Polynomial Chaos	4096	$9.35 \cdot 10^{-8}$	$2.14 \cdot 10^{-5}$
Random Forest Metamodel	389	$2.49 \cdot 10^{-5}$	$8.52 \cdot 10^{-4}$
Sparse Polynomial Chaos	389	$9.77 \cdot 10^{-8}$	$2.14 \cdot 10^{-5}$

Table 4.1.2: Model error E_m and Sobol sensitivity error E_s for conventional PC, sparse PC and the RF metamodel with 4096 and 389 model evaluations (N).

4.1.3 QUALITATIVE SENSITIVITY SCREENING

4.1.3.1 EXPERIMENTAL SETUP

In this experiment, we compare the RF metamodel and the EE method for qualitative sensitivity screening with a low number of model evaluations. An in-depth description of the EE method can be found in Section 3.2.4. The EE method was performed using 25 l -levels and a step size Δ according to the suggestion by Campolongo et al. [111], $\Delta = \frac{l}{2(l-1)}$. The result of this qualitative sensitivity analysis gives a foundation for high-dimensional sensitivity analysis that will be relevant in subsequent chapters.

4.1.3.2 RESULTS

The results of the comparison of the RF metamodel and the EE method can be seen in Figure 4.1.4. Interestingly, the result shows that the sensitivity screening using the RF metamodel shows superior performance compared to the more commonly used EE method. The RF metamodel shows a higher ability to rank input parameters in accordance to their relative influence on FFR.

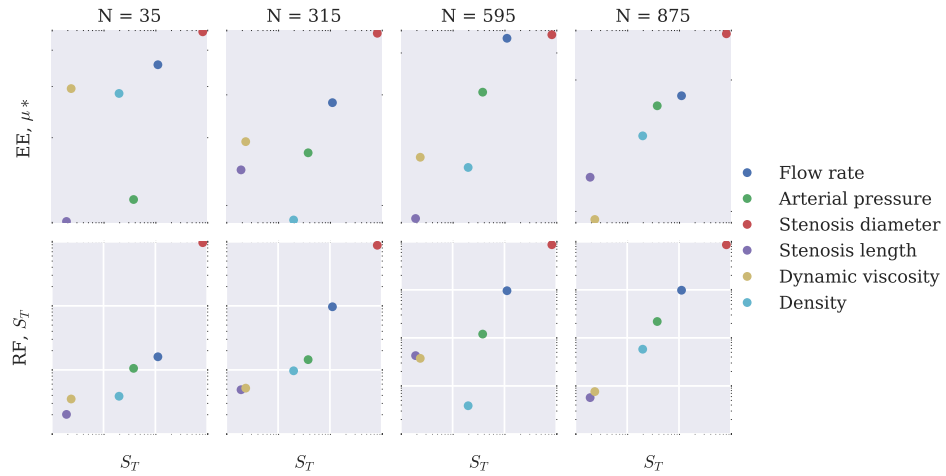


Figure 4.1.4: Quantitative sensitivity screening using the EE method and the RF metamodel (horizontal axis) vs. the ground truth Sobol indices (vertical axis). The comparison is performed with an increasing number of model evaluations.

Parameter	μ	μ^*	σ
Flow rate	-0.0018	0.028	0.037
Arterial pressure	-0.00012	0.024	0.033
Stenosis diameter	-0.0012	0.036	0.049
Stenosis length	0.00066	0.022	0.034
Dynamic viscosity	0.0012	0.022	0.034
Density	0.00065	0.024	0.036

Table 4.1.3: Elementary effects of input parameters to the single stenosis model (Huo model).

The elementary effects obtained from the EE screening can be seen in Table 4.1.3. We see that the values of the elementary effects μ^* are in excellent agreement with the parameter ranking obtained from the variance-based sensitivity analysis. Moreover, we see that the stenosis diameter d_s show the strongest elementary effect μ^* and the strongest non-linear effect σ compared to the other input parameters.

4.2 EFFECT OF UNCERTAINTY IN PHYSIOLOGICAL PARAMETERS ON CT_{FFR}

For this experimental case, we use the CT_{FFR} model and the published coronary geometry by Kassab et al. [29] introduced in Chapter 2. To investigate the effect of stenosed arteries, we induce a clinically relevant 75% area stenosis¹ in the proximal LAD using the stenosis model by Huo et al. [44] as described in Section 2.1.3.3. Using a combination of the CT_{FFR} model and the defined coronary network, we perform several analyses to investigate the influence of uncertainty in physiological parameters on CT_{FFR} .

The uncertainty in physiological model parameters is based on published literature discussed in Section 2.2.3. For this analysis, the physiological parameters are assumed to be independently distributed random variables. For comparison with experiments with geometric uncertainty, we assume an independently normal-distributed noise with a standard deviation of 15% as discussed in Section 2.1.4. A full description of the uncertain random variables can be seen in Figure 4.2.1.

¹Area stenosis: Fractional reduction in cross-sectional area of an artery due to the presence of a stenosis.

Variable	Unit	Distribution
Cardiac output	L/min	$\mathcal{U}(4, 8)$
Mean arterial pressure	$mmHg$	$\mathcal{N}(93.0, 7.6)$
Myocardial Flow Fraction		$\mathcal{U}(0.04, 0.05)$
Murray's coefficient		$\mathcal{U}(2.4, 3.0)$
TCRI		$\mathcal{U}(0.15, 0.30)$
Hematocrit		$\mathcal{N}(0.45, 0.08)$
Blood density	kg/m^3	$\mathcal{U}(1043, 1057)$

Table 4.2.1: Random variables for the uncertain physiological parameters in the CT_{FFR} model. Here, $\mathcal{N}(\mu, \sigma)$ denotes a normal distribution with mean μ and standard deviation σ and $\mathcal{U}(C_1, C_2)$ denotes a uniform distribution with a lower value of C_1 and an upper value of C_2 .

4.2.1 UNCERTAINTY QUANTIFICATION

4.2.1.1 EXPERIMENTAL SETUP

In this experiment, we quantify the effect of uncertainty in physiological input parameters on CT_{FFR} . The uncertainty is quantified using Latin Hypercube MC sampling with 5000 model evaluations as described in Section 3.2.1.

4.2.1.2 RESULTS

The prediction interval from the uncertainty quantification can be seen in Figure 4.2.1. We see that the input uncertainty from the physiological parameters results in a wide prediction interval over the stenosis. For example, we see that the 98% central prediction interval spans from an FFR of 0.6 to 0.9. As expected, the simulation shows a lower uncertainty in the healthy vessels segments, RCA, and CX.

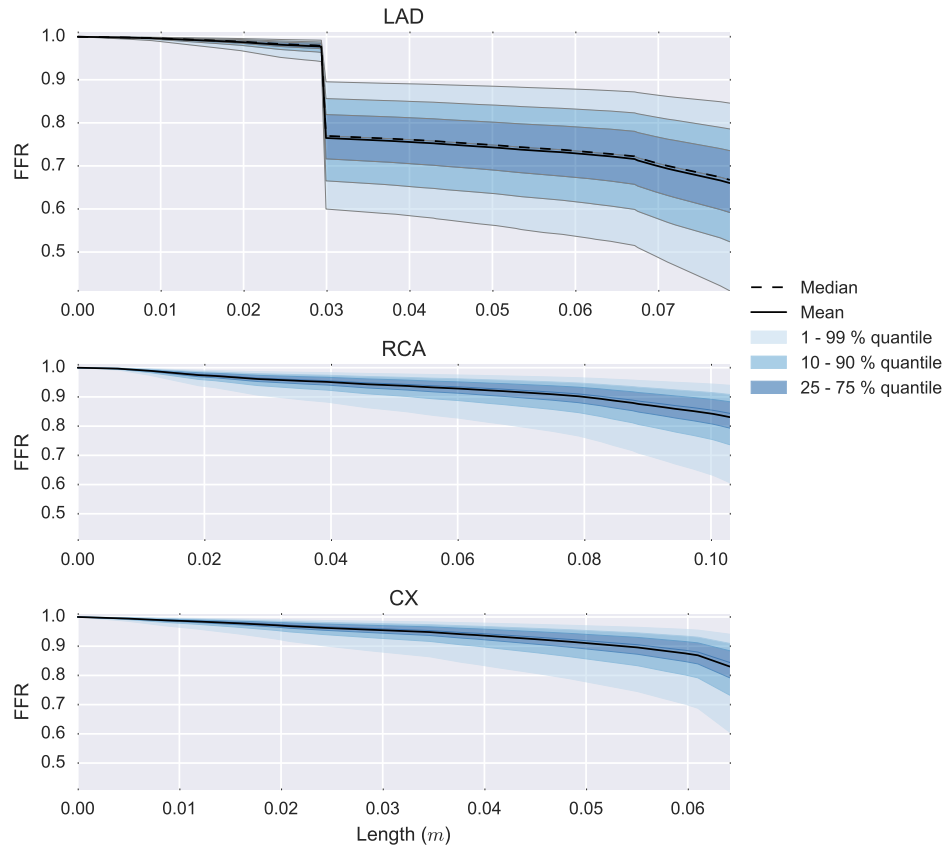


Figure 4.2.1: CT_{FFR} quantile plot for the stenosed artery (LAD) and the healthy arteries (RCA and CX) estimated from MC sampling with 5000 model evaluations. We evaluated the post-stenotic CT_{FFR} with a mean of 0.765 and a 95% prediction interval of [0.619, 0.885].

4.2.2 EFFECT OF UNCERTAINTY IN PHYSIOLOGICAL PARAMETERS AND SEGMENTATION UNCERTAINTY ON CT_{FFR}

4.2.2.1 EXPERIMENTAL SETUP

In this experiment, we want to get a crude approximation of the uncertainty in CT_{FFR} due to physiological parameters vs. lumen segmentation from CTA. The uncertainty in lumen segmentation is imposed by the introduction of an error term that is proportional to the measured radii. Hence, the radius of a vessel segment is given by the observed radius with the addition of a zero-mean normally distributed noise term ε so that

$$R = r_{obs}(1 + \varepsilon), \quad (4.1)$$

where r_{obs} is the observed radius. With no further knowledge about the uncertainty structure, we model ε as an iid random variable for each vessel. As discussed in Section 2.1.4, we assume that the geometric noise has a standard deviation of 15%. The uncertainty is quantified using Latin Hypercube MC sampling with 5000 model evaluations.

4.2.2.2 RESULTS

The comparison of the uncertainty in CT_{FFR} due to uncertainty in physiological parameters and lumen segmentation can be seen in Figure 4.2.2. We observe that the relevant uncertainties are characterized by wide prediction intervals. More precise, we see that the uncertainty in the lumen segmentation results in a slightly wider prediction interval than the uncertainty due to physiological parameters.

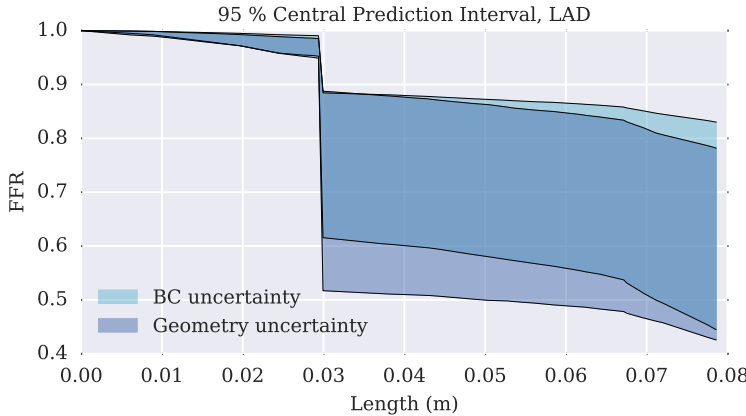


Figure 4.2.2: 95% FFR central prediction interval showing the uncertainty in CT_{FFR} due to uncertainty in physiological parameters and lumen segmentation. The experiment is performed using MC sampling with 5000 model evaluations.

4.2.3 SENSITIVITY ANALYSIS

4.2.3.1 EXPERIMENTAL SETUP

In this experiment, we perform a global sensitivity analysis to quantify the sensitivity of post-stenotic CT_{FFR} with respect to the uncertainty in physiological input parameters. The experiment is conducted to get a proper quantification of the most influential physiological parameters for the estimation of CT_{FFR} . The SA is performed using stochastic collocation PC (Section 3.2.2.4) with a polynomial order 3. Here, stochastic collocation PC is preferred over the pseudospectral PC since it gives us the ability to reuse samples from the UQ in Section 4.2.1. Additionally, SA is performed using the RF metamodel and the GMSA method described in Section 3.2.3. The purpose of using two approaches for global SA is to compare the highly scalable RF metamodel to the more acknowledged PC method on a relevant CT_{FFR} problem.

4.2.3.2 RESULTS

The results of the sensitivity analysis are shown in Figure 4.2.3. We see that the two most important parameters for CT_{FFR} is the cardiac output and the

microvascular vasodilatory response, represented by TCRI (Section 2.2.3.5). Interestingly, the flow distribution model and the Murray's coefficient have limited effect on the CT_{FFR} uncertainty. The figure also shows that the uncertainty in arterial pressure P_a , myocardial flow fraction (MFF), hematocrit and blood density is of less relevance to CT_{FFR} .

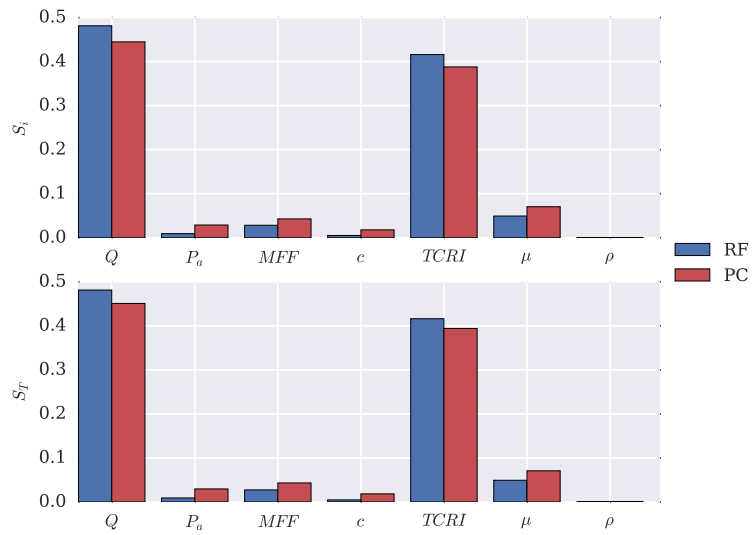


Figure 4.2.3: Sobol sensitivity indices for CT_{FFR} with respect to uncertainty in physiological input parameters using PC and the RF metamodel. Here, the sensitivity indices are estimated using 5000 model evaluations for both the RF metamodel and the stochastic collocation PC method.

4.2.4 EFFECT OF ADDITIONAL CLINICAL MEASUREMENTS ON CT_{FFR}

4.2.4.1 EXPERIMENTAL SETUP

A promising idea for future clinical applications of CT_{FFR} is to reduce the uncertainty in physiological parameters by additional clinical measurements. In theory, some the physiological parameters could be measured with non-invasive or minimally-invasive clinical methods. In particular, cardiac output and myocardial flow fraction can be derived through non-invasive methods e.g.

partial gas rebreathing, thoracic bioimpedance, photoelectric plethysmography, and transthoracic Doppler echocardiography [123, 124]. Moreover, measurements of hematocrit and dynamic blood viscosity can be done using basic clinical procedures [125]. Additionally, arterial blood pressure can be measured in a variety of different ways, most frequently using the standard upper arm blood pressure monitor [126]. Consequently, we are interested in how additional clinical measurements can be used to reduce the uncertainty in CT_{FFR} . In this experiment, we examine the reduction of uncertainty in CT_{FFR} when cardiac output, myocardial flow fraction, and hematocrit are seen as measured parameters with negligible uncertainty. The uncertainty is quantified using Latin Hypercube MC sampling with 5000 model evaluations.

4.2.4.2 RESULTS

The effect of additional measurements of flow rate, arterial blood pressure and hematocrit is seen Figure 4.2.4. Here, we see that the additional measurements give a substantial reduction in CT_{FFR} uncertainty. This is shown by a significant narrowing of the 95% central prediction interval over the length of the LAD.

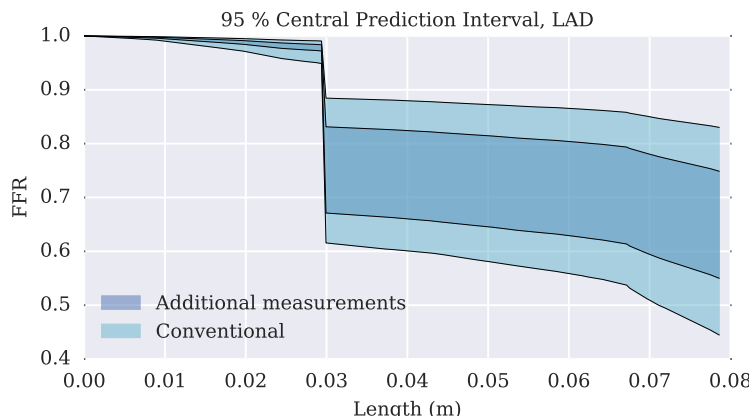


Figure 4.2.4: 95% central prediction interval using population-based physiological parameter (conventional) vs. additional clinical measurements of flow rate, arterial blood pressure, and hematocrit. The uncertainty is estimated using MC sampling with 5000 model evaluations.

4.2.5 THE EFFECT OF FLOW DISTRIBUTION MODEL ON CT_{FFR}

4.2.5.1 EXPERIMENTAL SETUP

An intriguing aspect of our CT_{FFR} model is the calculation of flow distribution and terminal vessel resistances using Murray's law. In our previous experiments, we assumed a global Murray's coefficient. As we will discuss more thoroughly in Chapter 5, this could be a questionable assumption from a physiological standpoint. Here, we argue that it is more likely that Murray's coefficient have a local nature that depends on the hydrodynamic conditions of the vessel. Furthermore, we have assumed that the uncertainty in flow distribution is unaffected by segmentation error. In practical applications of CT_{FFR} , Murray's law will result in a combined uncertainty from segmented vessel radii and local Murray's coefficients. For this system, the terminal resistance of vessel i is given by

$$R_i \sim (r_{obs,i}(1 + \varepsilon_i))^{-C_i}, \quad (4.2)$$

where ε_i is a zero-mean normally distributed variable with a standard deviation of 15%. In the absence of further knowledge about the uncertainty structure, we model ε_i and C_i as iid for all terminal vessels of our system. The governing theory for specification of terminal resistances in the CT_{FFR} model is presented in Section 2.2.1.2.

In this experiment, we compare the resulting uncertainty in CT_{FFR} of a system where the uncertainty in terminal resistances is governed by Equation 4.2, to a system where the uncertainty in terminal resistances is determined by a global uncertain Murray's coefficient. The uncertainty is quantified using Latin Hypercube MC sampling with 5000 model evaluations.

4.2.5.2 RESULTS

In Figure 4.2.5, we compare a model with global Murray's coefficient (model 1), to a model with a local iid Murray's coefficient for each vessel and geometric

uncertainty with standard deviation $\sigma = 15\%$ (model 2). As expected, we see that the result from model 2 shows a significantly broader prediction interval and variance than model 1. Thus, the assumption of local Murray's coefficient and geometric uncertainty is a significant source of uncertainty for flow distribution in CT_{FFR} models.

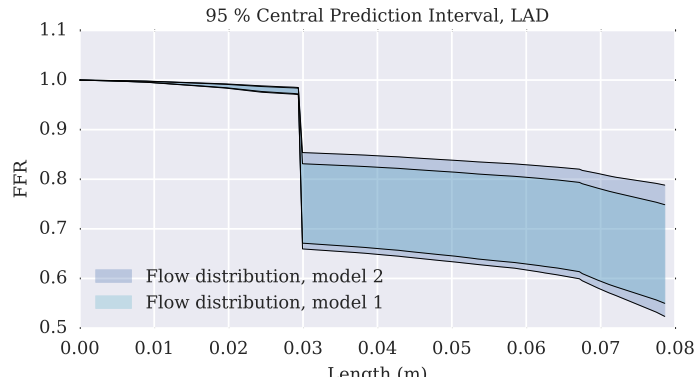


Figure 4.2.5: 95% central prediction interval for the simulation with global Murray's coefficient (Model 1) and the simulation with a local Murray's coefficients for each vessel and geometric uncertainty with standard deviation $\sigma = 15\%$ (model 2). The prediction interval is estimated using MC sampling with 5000 model evaluations.

4.3 DISCUSSION

In this chapter, we have investigated the effect of uncertainty of input parameters on FFR for a single stenosis model and the effect of uncertainty in physiological parameters on FFR in a CT_{FFR} model. Our results show that moderate uncertainty in input parameters can result in a rather dramatic uncertainty on estimated FFR and could have a significant impact on clinical decisions.

For the single stenosis model, we find that the most influential parameter is the stenosis diameter. This is in agreement with findings from Eck et al. [74] which investigated sensitivity to input parameters in a similar stenosis model. Furthermore, the results are in agreement with Sankaran et al. [20] who studied

the sensitivity of FFR to model parameters in several 3D CFD simulations. For the CT_{FFR} model, the most influential physiological parameters are found to be cardiac output and myocardial vasodilatory response, TCRI.

The importance of geometric uncertainty is confirmed by a comparison of the uncertainty in CT_{FFR} due to uncertainty in physiological parameters and lumen segmentation. Here, we find that the uncertainty in lumen segmentation results in a slightly higher uncertainty in CT_{FFR} compared to uncertainty in physiological parameters. However, it must be noted that the quantification of uncertainty from lumen segmentation is based on rough assumptions that could have questionable accuracy. For example, the assumption of iid segmentation errors is likely to be unrealistic for a segmentation process with continuous vessel walls.

Surprisingly, the sensitivity analysis shows that the flow distribution model and Murray's coefficient have a very low influence on the estimated FFR. Nonetheless, we find that the flow distribution model becomes significantly more important by taking into account the effect of geometric uncertainty and by treating Murray's coefficient as a local parameter.

Additionally, we propose methods to decrease the influence of uncertainty in physiological parameters on CT_{FFR} . Interestingly, we show that the uncertainty in CT_{FFR} can be significantly reduced by additional clinical measurements. For example, cardiac output, myocardial flow fraction, and hematocrit could be measured non-invasively with current clinical tools. However, methods to reduce the effect of uncertainty from other critical physiological parameters, e.g. the microvascular vasodilatory response and flow distribution model, are less clear. A discussion of possible methods to reduce the uncertainty from these sources is given in Chapter 7.

Also, our analysis shows promising results for the application of GMSA and the RF metamodel for Sobol sensitivity analysis. Despite lower performance than PC, the RF metamodel shows accurate sensitivity indices for the investigated cases. Furthermore, results from the screening analysis indicate that the RF metamodel exhibit superior performance when compared to the more established EE method on the single stenosis case.

Simplicity is the ultimate sophistication.

Leonardo da Vinci

5

Uncertainty in CT_{FFR} Flow Distribution Model

In this chapter, we perform an in-depth investigation of the flow distribution model used to estimate CT_{FFR} . For this reason, we examine the most commonly applied model for flow distribution in CT_{FFR} models, Murray's law. In particular, we want to investigate the uncertainty in Murray's law using empirical data from Kassab et al. [29] (Section 2.1.4). As described in Section 2.2.1.2, the practical implementation of the flow distribution model is done by a specification of relative terminal resistances.

Using backward uncertainty analysis as outlined in Section 3.3, we aim to establish a model that efficiently captures the uncertainty in Murray's law. Here, we investigate the effect of the uncertainty of Murray's law on CT_{FFR} . Furthermore, we study the sensitivity of CT_{FFR} to individual terminal resistances.

The goal of this procedure is to obtain valuable knowledge that can improve decision-making in practical applications of CT_{FFR} .

5.1 BACKGROUND

5.1.1 OPTIMAL DESIGN PRINCIPLES

The most promising way to specify terminal resistances in CT_{FFR} models is through optimal design principles. There seems to be a widespread consensus that branching morphology of biological systems is subject to optimization principles. This is justified by evolutionary morphogenetic arguments based on natural selection [21–23]. Thus, optimal design patterns play a crucial role in determining radii and branching angles of vessels in the vascular system. Research has shown that blood vessels optimize their size based on flow rate and the wall shear stress sensed by the endothelial cells [127]. Importantly, the optimization of vessel radii continues even in the presence of atherosclerosis [128].

5.1.2 MURRAY'S LAW

As introduced in Section 2.2.1.2, the most prominent and influential branching model based on optimization principles is Murray's law [12, 17, 24, 25], which is derived from assuming minimization of energy consumption of flow systems in living organisms [22, 23]. The essence of Murray's law is that the organism balances the influence of metabolic- and mechanical energy consumption. First, the metabolic energy consumption of the vascular system increases with increasing vessel radius. Second, the mechanical energy required to pump blood through the vascular system is a function of friction and decrease with increasing radius. According to Murray's hypothesis, vessel radius in the vascular system is determined to minimize the energy requirement from these two factors.

Formally, Murray's law is given by

$$q \propto r^c, \quad (5.1)$$

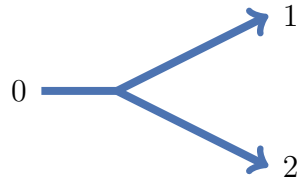


Figure 5.1.1: Arterial bifurcation with mother vessel (0) and the daughter vessels (1 and 2).

where c represents the Murray's coefficient, q is the flow rate, and r is the vessel radius. According to Murray's original work, the metabolic energy consumption is proportional to r^2 , while the mechanical energy consumption for laminar flow is proportional to r^4 , giving an optimization constant of $c = 3$. A full derivation of this argument can be found in Murray's original paper [129].

Assuming the existence of a universal constant of proportionality, Murray's law gives the following power-law relationship for a bifurcation

$$r_0^c = r_1^c + r_2^c, \quad (5.2)$$

where 0 represents the mother vessel and 1 and 2 represents daughter vessels as shown Figure 5.1.1.

The relative outflows obtained from Murray's law can directly specify terminal resistances in CT_{FFR} simulations. The resistance of a terminal vessel i according to Murray's law is given by

$$R_i \propto r_i^{-c}. \quad (5.3)$$

5.1.3 EMPIRICAL VARIATION AND UNCERTAINTY IN MURRAY'S LAW

An important question in practical work is how to deal with empirical variation and uncertainty when establishing terminal resistances from Murray's law. Research has shown a significant variation in the reported value of Murray's coefficient c . To date, most researchers have reported a value of Murray's

Author	Year	Specification	c
Murray [22, 23]	1926	Theoretical/empirical	3.0
Miller [130]	1893	Dog lung arteries	2.61
Fukasawa and Hitoshi [131]	1969	Human coronary arteries	2.66 – 2.82
Hutchins et al. [132]	1976	Human coronary arteries	2.7 – 3.2
Arts et al. [133]	1979	Canine coronary arteries	2.55
Sherman [134]	1981	Dog arteries	≈ 2.9
Changizi and Cherniak [135]	2000	Human coronary arteries	2.60
Wang et al. [136]	2012	Human arteries	2.75
Revellin et al. [138]	2009	Theoretical	2.42 – 3

Table 5.1.1: Theoretical and empirical estimations of Murray's coefficient from the literature.

coefficient between $2.3 – 3.0$ [22, 23, 130–136]. Interestingly, this interval coincides with the optimal values for laminar and turbulent flow, $c = 3$ and $c = 7/3$, respectively [137]. An overview of empirically determined Murray's coefficients from the literature can be found in Table 5.1.1.

Furthermore, the extraction of geometry from CTA is likely to be a significant source of uncertainty in practical applications of Murray's law. Moreover, it is reasonable to assume that the cardiovascular system could show biological deviation from Murray's law, for example in areas of bifurcations, stenosis, and irregularities.

5.2 REGRESSION ANALYSIS

In this section, regression analysis is used to estimate the unknown parameter of Murray's law, Murray's coefficient. In basic regression analysis, a suitable model is used to find relationships among variables of interest. The regression model is fitted by minimization of an appropriate loss function, e.g. using the least squares approach. Here, the minimization is done using the Nelder-Mead algorithm from the *Scipy* library [62], which is a beneficial method for nonlinear optimization problems where the derivatives of the loss function may be unknown [139].

5.2.1 BIFURCATIONS

5.2.1.1 EXPERIMENTAL SETUP

In the first experiment, we want to find the Murray's coefficient that satisfies the equation

$$r_0^c = r_1^c + r_2^c, \quad (5.4)$$

where the mother vessel is represented by subscript 0 and the daughter vessels are represented by subscript 1 and 2. Thus, we want to find the value of c that minimizes the squared error

$$\min_c (r_1^c + r_2^c - r_0^c)^2. \quad (5.5)$$

for each bifurcation in our dataset. For this analysis, a total of 78 bifurcations is evaluated.

5.2.1.2 RESULTS

The result from the regression analysis on single bifurcations can be seen in Figure 5.2.1. We see that the fitted Murray's coefficient shows large variance with a mean value $\mu = 2.24$ and a standard deviation $\sigma = 1.09$. Furthermore, we see that the best-fitted Murray's coefficient tends towards an asymmetric long-tail distribution.

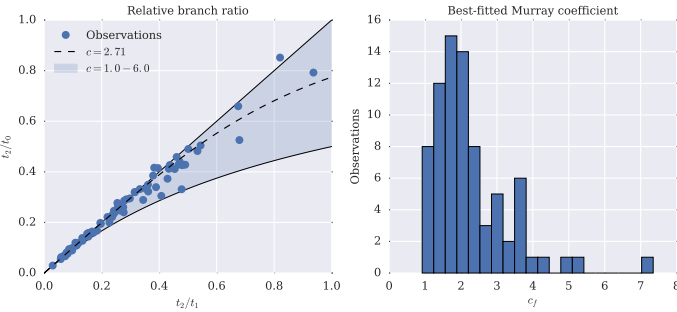


Figure 5.2.1: Branching ratio and best-fitted Murray coefficient for individual branches of the coronary dataset. The results estimate a Murray's coefficient of 2.24 ± 1.09 (mean \pm SD).

5.2.2 CONTROL VOLUMES

5.2.2.1 EXPERIMENTAL SETUP

To take full advantage of the data in the coronary tree, we use a technique we call control volume sampling. In this approach, we analyze Murray's law over all unique control volumes in our system. In Figure 5.2.2, we see an example of control volume sampling over a double bifurcation.

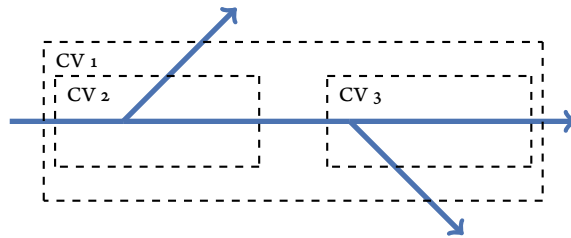


Figure 5.2.2: Control volume sampling over all possible control volumes of a double bifurcation.

Using control volume sampling, we find the Murray's coefficient that satisfies

the equation

$$r_0^c = \sum_{i=1}^{N_i} r_i^c, \quad (5.6)$$

where N_i is the number of flow outlets of the control volume. Thus, we want to find the value of c that minimizes the squared error

$$\min_c \left(\sum_{i=1}^{N_i} r_i^c - r_0^c \right)^2. \quad (5.7)$$

over all possible control volumes in our coronary dataset. In this experiment, we analyze a total of 1489 control volumes.

5.2.2.2 RESULTS

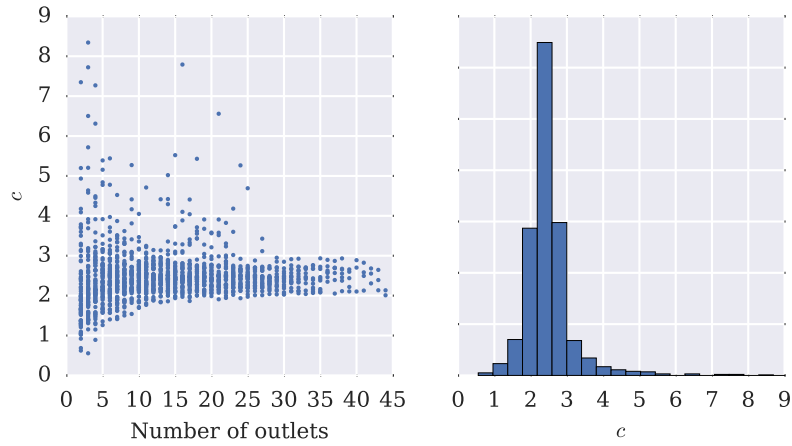


Figure 5.2.3: The distribution of best-fitted Murray's coefficient as a function of control volume outlets (left) and presented as a histogram (right). The Murray's coefficient for control volumes is characterized by a mean value $\mu = 2.49$ and a standard deviation $\sigma = 0.67$.

The result from the control volume analysis can be seen in Figure 5.2.3. The fitted Murray's coefficient shows lower variance compared to the analysis

performed on single bifurcations in Section 5.2.1. The Murray's coefficient for control volumes can be quantified with a mean value $\mu = 2.49$ and standard deviation $\sigma = 0.67$. We see that the variation in the fitted value of c is rapidly decreasing with an increasing number of control volume outlets.

5.3 BACKWARD UNCERTAINTY ANALYSIS

As discussed in Section 5.1.3, there is reason to believe that the total uncertainty of Murray's law is a result of combined contributions of geometric uncertainty and uncertainty in Murray's coefficient. To better capture the structure of the uncertainty of the problem, we introduce a geometric uncertainty term so that the true radius r_{true} is given by the observed radius r_{obs} subject to a proportional noise term ε

$$r_{true} = r_{obs} (1 + \varepsilon), \quad (5.8)$$

where ε is a zero-mean normally distributed random variable with standard deviation σ . Using this model assumption, Murray's law for a control volume is given by

$$(r_0(1 + \varepsilon_0))^C = \sum_{i=1}^{N_i} (r_i(1 + \varepsilon_i))^C, \quad (5.9)$$

where ε_i are iid variables.

Using Equation 5.9, we can infer the uncertainty of ε_i and C using Bayesian inference. The distributions of ε_i and C give us the ability to model the uncertainty in individual outlets. For example, the uncertain resistance of a terminal vessel i can be modeled as

$$R_i \sim (r_i(1 + \varepsilon_i))^{-C}, \quad (5.10)$$

and gives us the ability to estimate the sensitivity of CT_{FFR} with respect to the

individual uncertainty of terminal resistances.

5.3.1 BAYESIAN INFERENCE

5.3.1.1 EXPERIMENTAL SETUP

In this experiment, we analyze the uncertainty structure of Murray's law using Bayesian inference. Thus, we rephrase Equation ?? to a relation where the mother radius is given as a function of the daughter radii

$$r_0(1 + \varepsilon_0) = \left(\sum_i (r_i(1 + \varepsilon_i))^C \right)^{1/C}. \quad (5.11)$$

In the Bayesian framework, we want to find the probability distributions $p(\sigma|\mathbf{r})$ and $p(C|\mathbf{r})$, where \mathbf{r} are the measured radii of the dataset. To do this, we use the following priors and hyperprior

$$p(C) = \mathcal{U}(0, 100), \quad (5.12)$$

$$p(\sigma) = \mathcal{U}(0, 100), \quad (5.13)$$

$$p(\varepsilon_i) = \mathcal{N}(0, \sigma). \quad (5.14)$$

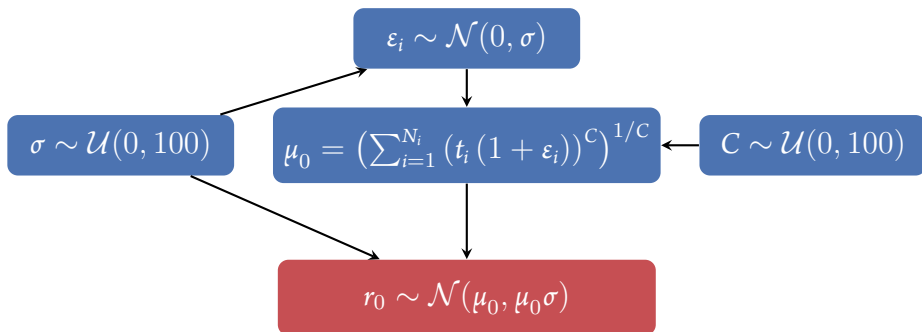


Figure 5.3.1: Graphical representation of hierarchical Bayesian model.

The wide uniformly distributed priors are chosen to cover the entire parameter space and minimize the influence on the posteriors. To test the objectivity of

these priors, we measure the Kullback-Leibler divergence between the priors and the resulting posteriors. A more thorough explanation of priors in Bayesian analysis is presented in Section 3.3.1. A graphical description of our Bayesian hierarchical model can be seen in Figure 5.3.1.

To validate our proposed model, we perform a residual analysis over the control volumes using the maximum a posteriori probability (MAP)¹ estimates. Since ε_i is a zero-mean symmetrical distribution, the MAP estimate of ε_i is equal to zero. Thus, the residual e for a control volume is given by

$$e = \sum_{i=1}^{N_i} r_i^{\hat{C}} - r_0^{\hat{C}}. \quad (5.15)$$

Further, the error of the residual e^* is defined as the absolute value of the residual

$$e^* = |e|. \quad (5.16)$$

5.3.1.2 RESULTS

The resulting posterior distributions for C and σ from the Bayesian inference can be seen in Figure 5.3.2. The posterior of C is characterized by a mean of 2.56 and standard deviation of 0.028, whereas the posterior of σ is characterized by a mean of 0.151 and standard deviation of 0.0028. We see that the posteriors show excellent convergence, which is quantified by a reciprocal of the Kullback-Leibler divergence between the priors and posteriors approximately equal to zero. Thus, we conclude that the priors have limited influence on the posteriors.

To validate our modeling approach, we use the MAP estimate for the posterior of C to plot the residuals for different control volumes. The result from this analysis can be seen in Figure 5.3.3. Here, we visualize the relationship between mother vessel diameter and the calculated residuals as defined in Equation 5.15. Based on these results, we observe a trend of increasing error e^* as a function of

¹Maximum a posteriori probability (MAP): Mode of the posterior distribution.

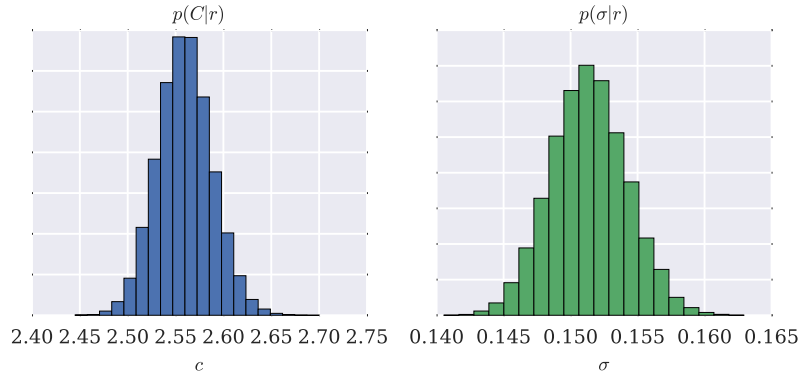


Figure 5.3.2: Posterior distributions of Murray's coefficient $p(C|r)$ and geometric uncertainty $p(\sigma|r)$ inferred using Bayesian analysis. The convergence of the procedure is validated through the Kullback-Leibler divergence between the priors and posteriors.

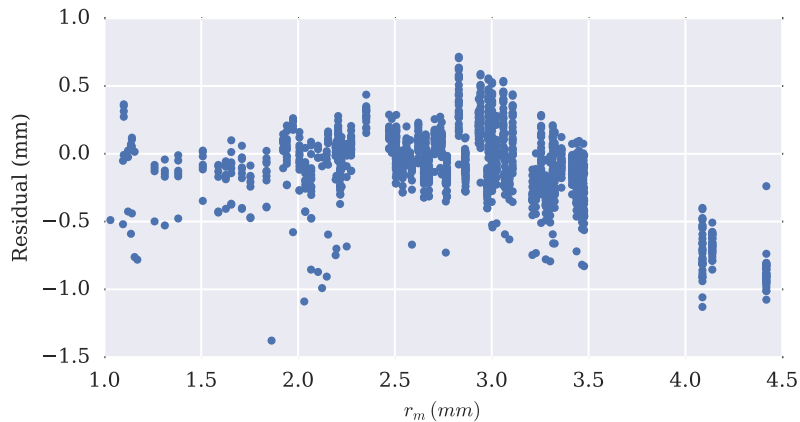


Figure 5.3.3: Residuals for the MAP estimates as a function of observed mother diameter. Note that the residual analysis is done over 1489 control volumes and that the fraction of observations in the region around a residual of $0 - 0.25 \text{ mm}$ is very high.

mother diameter. We observe that the MAP estimate leads to an under-estimation of radius for the largest mother diameters, but are unable to find other meaningful structures in the residuals.

5.3.2 UNCERTAINTY QUANTIFICATION

5.3.2.1 EXPERIMENTAL SETUP

Once the posterior distributions are inferred, the relative resistance $R_{rel,i}$ is given by

$$R_{rel,i} = (r_i (1 + \varepsilon_i | \mathbf{r}))^{-C|\mathbf{r}|} \quad (5.17)$$

where $\varepsilon_i | \mathbf{r}$ and $C | \mathbf{r}$ are the posterior distributions of ε_i and C , respectively.

In this experiment, we investigate the effect of uncertainty in Murray's law on CT_{FFR} by sampling from the distributions of relative outlet resistances. In practice, we quantify the uncertainty of CT_{FFR} in the coronary network introduced in Section 4.2 using Latin Hypercube MC sampling with 5000 model evaluations.

5.3.2.2 RESULTS

Figure 5.3.4 shows that the uncertainty in Murray's law gives a significant post-stenotic uncertainty of CT_{FFR} . Quantitatively, the 95% central prediction interval gives a post-stenotic interval of $[0.728, 0.814]$, where the CT_{FFR} values are measured right after the stenosis.

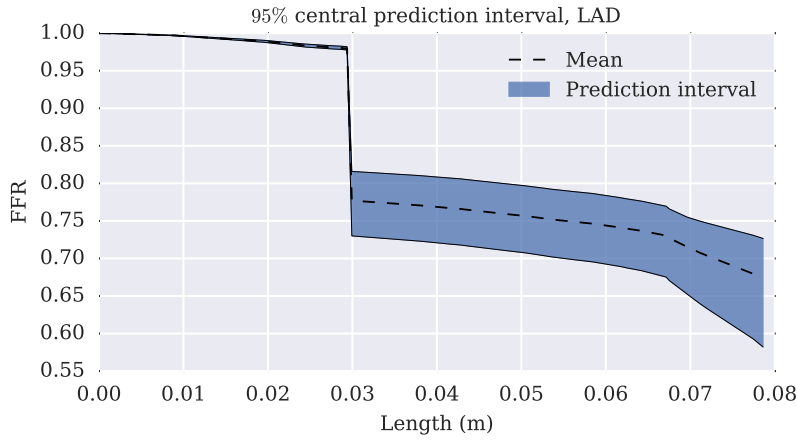


Figure 5.3.4: 95% central prediction interval showing the uncertainty in CT_{FFR} as a result of uncertainty in Murray's law estimated from MC sampling with 5000 model evaluations.

5.3.3 SENSITIVITY ANALYSIS

5.3.3.1 EXPERIMENTAL SETUP

In this experiment, we want to investigate the sensitivity of CT_{FFR} with respect to the uncertainty in individual terminal resistances. First, we examine the sensitivity of $R_{rel,i}$, defined in Equation 5.17, with respect to $\varepsilon|\mathbf{r}$ and $C|\mathbf{r}$ using PC. Thus, we analyze the relative effects of Murray's coefficient and geometric uncertainty on the total uncertainty associated with Murray's law. For efficient evaluation, we approximate the PDFs/CFDs of the posterior distributions using parametric approximations from the *Scipy* library [62].

Second, we evaluate the sensitivity of CT_{FFR} to terminal resistances using the coronary network introduced in Section 4.2. Due to the high number of outlets ($N_i = 114$), the sensitivity analysis is performed using the RF metamodel. A thorough explanation of the RF metamodel is given in Section 3.2.3.

5.3.3.2 RESULTS

The sensitivity of a relative terminal resistance with respect to the geometric uncertainty ε_i and the uncertainty in Murray's coefficient C can be seen in Table 5.3.1. The results show that the uncertainty in the relative terminal resistances is determined almost solely by the geometrical uncertainty term ε_i .

Parameter	$S_{1,i}$	$S_{T,i}$
C	0.01	0.01
ε_i	0.99	0.99

Table 5.3.1: Main and total Sobol sensitivity indices expressing the sensitivity of a relative terminal resistance with respect to the geometric uncertainty term ε_i and the uncertainty in Murray's coefficient C . The sensitivity analysis is performed using PC and the parametrized posterior distributions for ε_i and C .

Based on the findings from the sensitivity analysis of a relative terminal resistance $R_{rel,i}$, we neglect the effect of uncertainty in Murray's coefficient on terminal resistance uncertainty. Thus, we quantify the sensitivity of CT_{FFR} with respect to the geometric uncertainty of the terminal resistances. The result from the sensitivity analysis is shown in Figure 5.3.6 and Figure 5.3.5. We observe that the sensitivity of CT_{FFR} with respect to terminal resistance uncertainty increases with increasing outlet diameter. Relative to outlet diameter, we observe that CT_{FFR} is particularly sensitive to the post-stenotic outlets. No clear differences are observed for vessel outlets in the RCA, pre-stenotic LAD, or CX region.

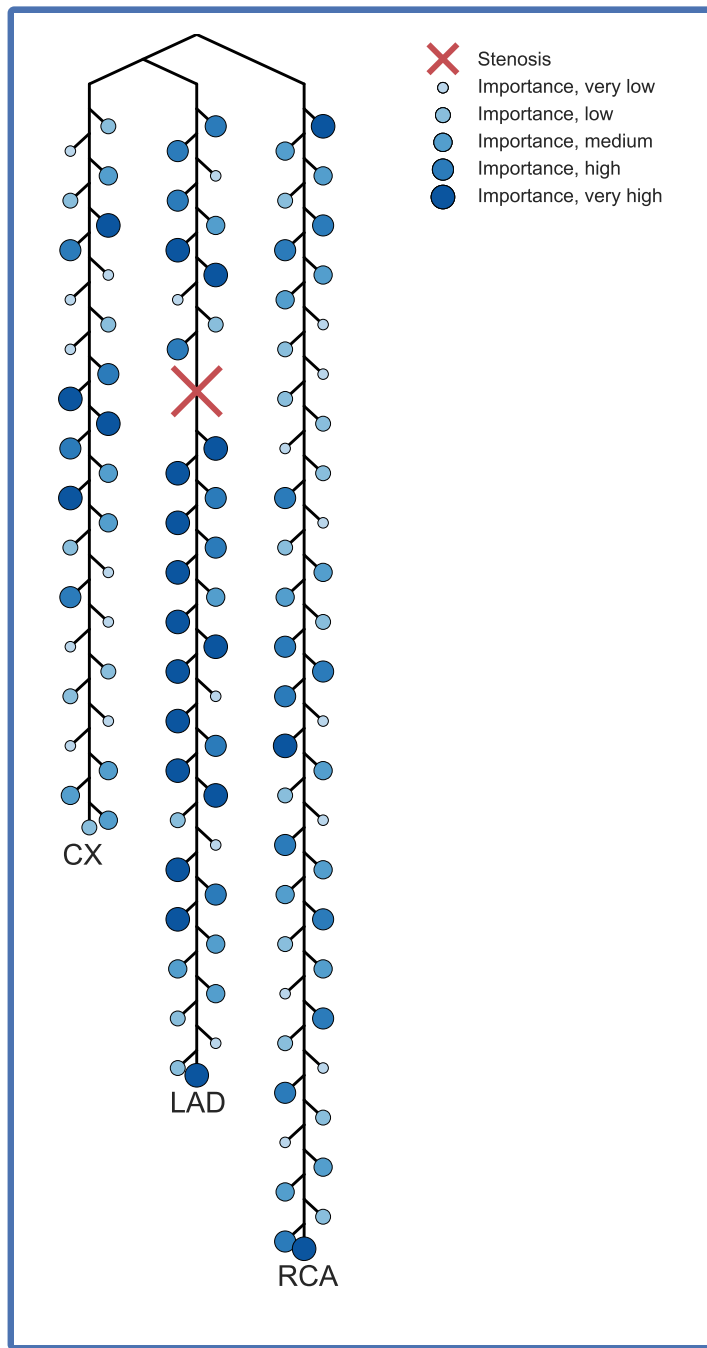


Figure 5.3.5: Coronary tree with a stenosis in the upper LAD and outlets grouped after the relative importance of terminal resistances according to the total Sobol sensitivity indices.

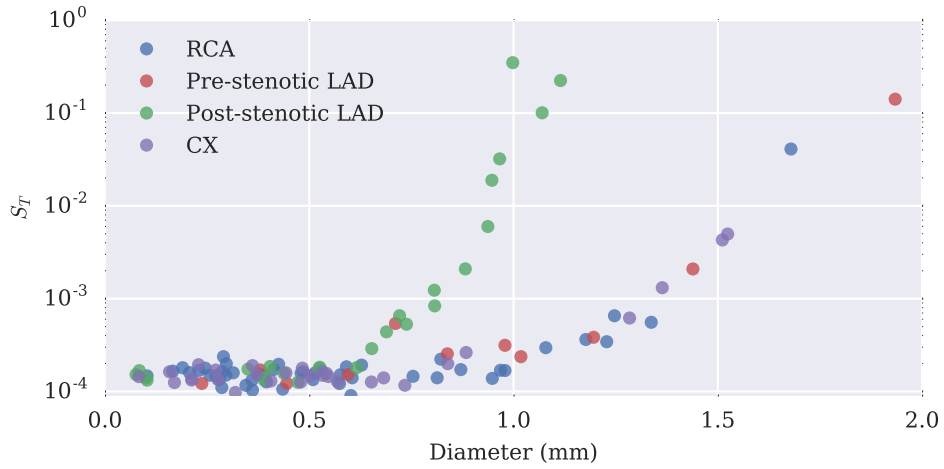


Figure 5.3.6: Total Sobol sensitivity of CT_{FFR} to terminal resistance uncertainty in the coronary tree with a stenosis in the upper LAD. The Sobol sensitivity indices are plotted according to reported vessel diameters of the coronary dataset.

5.4 DISCUSSION

Terminal outlet resistances for CT_{FFR} are typically determined using Murray's law. Here, we analyze Murray's law using the published dataset of coronary artery geometry from Kassab et al. [29]. Our regression analysis shows that Murray's coefficient has high variability when fitted for single bifurcations, but that the variability reduces when Murray's law is evaluated over larger control volumes. The mean fitted value of Murray's coefficient using control volume sampling shows good agreement with the MAP estimate from Bayesian inference, $c = 2.49$ vs. $c = 2.56$, respectively. In contrast, the mean fitted value of Murray's coefficient for bifurcations is $c = 2.24$, which shows that estimates for Murray's coefficient are sensitive to the modeling approach. The residual analysis indicates that the absolute deviation from Murray's law increase with increasing vessel radius. Further, the residuals show a systematic deviating trend for higher vessel radii. It is unclear whether this deviation is a result of noise or uncaptured structures in the dataset.

The results from the Bayesian analysis show that the relationship between vessel radii in the coronary system can be successfully modeled by a power law relationship. Although, with the current modeling approach, we see that relative resistances determined from Murray's law are heavily influenced by geometric uncertainty. In contrast, the uncertainty in Murray's coefficient has a lower influence on the terminal resistance uncertainty.

Further, we evaluate the effect of uncertainty in terminal resistances on CT_{FFR} , and find that larger vessels and vessels downstream from the stenosis are of greater importance to the resulting estimate (see Figure 5.3.6 and 5.3.5). This finding could prove valuable for clinical applications of CT_{FFR} . CTA image data has variable quality depending on factors like angle, slice thickness, patient movement and more. The take-home message from this work is that a proper description of post-stenotic outlets is necessary for an accurate CT_{FFR} estimate. On the other hand, uncertainties in pre-stenotic regions and parallel vessels are of less importance to the CT_{FFR} estimate.

It must be noted that the inferred uncertainty of Murray's law was derived from the coronary dataset of Kassab et al. [29]. In contrast to the geometry in a conventional CT_{FFR} simulation, this geometry was quantified using an elastomer-casting method. Based on the high uncertainty of coronary lumen segmentation, it is reasonable to believe that the uncertainty in CT_{FFR} as a result of uncertainty in Murray's law could be even higher than estimated in this chapter.

Also, the accuracy of the variance-based sensitivity analysis with the RF metamodel is unclear. Results from experiments in previous chapters (Section 4.1.2, 4.2.3 and 4.1.3) show promising results for problems with fewer input parameters. However, the exact accuracy for problems with high-dimensional input spaces is unclear. The main challenge is that a proper validation of the RF metamodel would require a high-dimensional MC analysis, an extremely computationally expensive procedure. Using the current run time, our computational resources and the necessary number of samples based on published literature by Sarrazin et al. [140], our estimates indicate that a full MC validation would require a computational time of between 10 and 45 days.

However, the validation would be feasible using the latest tools in high-performance computing and is an interesting area for future research.

Errors are not in the art but in the artificers.

Sir Isaac Newton

6

Invisible Arteries

Capturing the fluid dynamics of the coronary arteries requires a complete mapping of all branches in the coronary system. However, the current resolution of CTA only enables a mapping of coronary arteries down a vessel diameter of $\approx 1\text{ mm}$ [personal communication, 9/23, 2015]. General practice in applications of CT_{FFR} is to model major arteries and neglect the effect of small branching vessels on pressure and flow characteristics [[26](#)].

There is reason to believe that neglecting minor arteries could have a significant impact on estimated pressure and flow in a coronary simulation. In segmented vessel data from CTA, it is common to observe vessel tapering in the absence of branching. However, research in both healthy and atherosclerotic patients have found no significant tapering in vessel segments without arterial branches [[141](#)]. Thus, observed vessel tapering on CTA indicates that the flow loss to invisible



Figure 6.0.1: A cast of coronary arteries with the right coronary arteries in yellow and the left coronary arteries in red. The figure shows the high density of arteries and branches in the coronary system [142].

branches is of a magnitude that could imply a possible effect on CT_{FFR} estimates.

In this chapter, we estimate the effect of invisible branches on volumetric flow loss and CT_{FFR} using the model presented in Chapter 2. For this purpose, we use the coronary geometry dataset from Kassab et al. [29] where coronary arteries are mapped down to an arterial diameter of $\approx 0.1\text{ mm}$. A more thorough description of this dataset can be found in Section 2.1.4. Also, we propose a mathematical model to reduce the effect of blood loss due to unaccounted branching to invisible arteries on CT_{FFR} .

6.1 LEAKY VESSEL MODEL (LVM)

Here, we propose a mathematical model to investigate the effect of invisible branches on CT_{FFR} which we refer to as the Leaky Vessel Model (LVM). The essence behind the LVM is that we attempt to model the flow to invisible arteries

by introducing a leakage term. In practice, this is done by adding an additional flow outlet and a corresponding resistance for every vessel segment in our CT_{FFR} model.

To estimate the resistance values, we minimize the difference between the model flow and the theoretical flow according to Murray's law. The model flow q_i for a vessel segment i is a function of the microvascular resistance R_{micro} (Section 2.2) and the additional leakage resistances \mathbf{R}_l so that

$$q_i = f(R_{micro}, \mathbf{R}_l), \quad (6.1)$$

where f is the CT_{FFR} model. The theoretical flow for the vessel segment i according to Murray's law is given by

$$q_i = ar_i^c, \quad (6.2)$$

where a is the proportionality constant of Murray's law. Thus, the leakage resistances \mathbf{R}_l are found by solving the optimization problem

$$(\mathbf{R}_l, R_{micro}, a) = \arg \min \sum_i \left(\frac{q_i(R_{micro}, \mathbf{R}_l) - ar_i^c}{ar_i^c} \right)^2. \quad (6.3)$$

where the minimization is performed with respect to the leakage resistances \mathbf{R}_l , the microvascular resistance R_{micro} and the proportionality constant a .

6.2 QUANTIFICATION OF FLOW TO INVISIBLE BRANCHES

6.2.1 EXPERIMENTAL SETUP

In this experiment, we estimate the flow to CTA-invisible coronary arteries based on the coronary geometry dataset. First, we identify invisible and visible outlets for the coronary system with different CTA-visibility thresholds. Second, we estimate the expected flow fraction to invisible arteries using the CT_{FFR} model. The expected flow fractions are based on Murray's law with the empirically

determined value of the Murray's coefficient, $c = 2.56$ as found in Chapter 5. Also, we investigate the flow fraction to invisible arteries for different values of Murray's coefficient.

6.2.2 RESULTS

Figure 6.2.1 shows the number of visible- and invisible flow outlets for three different visibility thresholds, 0.5 mm , 1.0 mm and 1.5 mm . The ratios of visible to total flow outlets are $54/114$, $16/114$ and $4/114$ for the visibility thresholds 0.5 mm , 1.0 mm and 1.5 mm , respectively. This means that only 14.0% of the total flow outlets are visible at the clinically relevant visibility threshold of 1 mm .

Figure 6.2.2 shows the flow fraction to invisible branches as a function of distance from the inlet of the coronary artery tree for three different visibility thresholds, 0.5 mm , 1.0 mm and 1.5 mm . The result suggests that a significant fraction of the coronary flow disappears to invisible branches for all visibility thresholds considered. In particular, the results indicate that up to $\approx 50\%$ of the coronary flow is through invisible branches for the clinically relevant visibility threshold of 1 mm . Importantly, this finding is not heavily influenced by different assumptions of Murray's coefficient, c . Also, we observe that the visibility threshold has a significant effect on the flow fraction to invisible branches, e.g. a visibility threshold of 0.5 mm reduces the maximum flow fraction to invisible branches down to $\approx 10\%$.

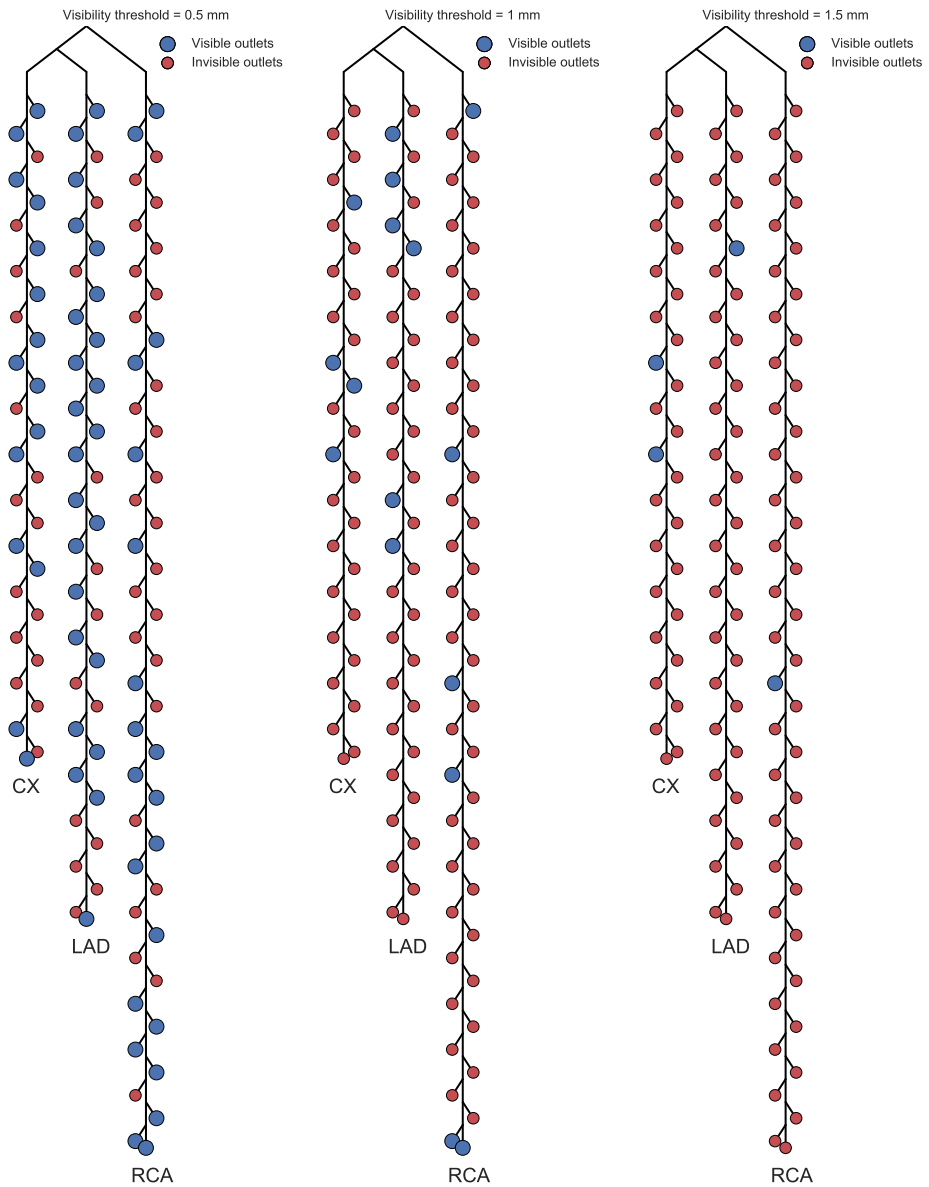


Figure 6.2.1: Figure showing visible and invisible flow outlets of the coronary tree for three different visibility thresholds, 0.5 mm (left), 1.0 mm (middle) and 1.5 mm (right).

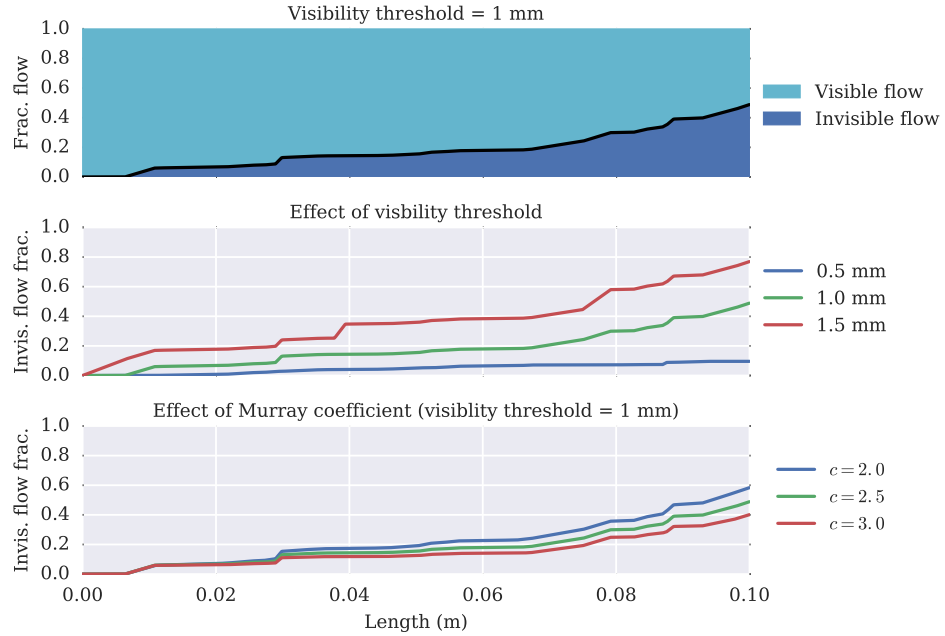


Figure 6.2.2: Fractional flow to invisible branches as a function of length from the inlet of the coronary arteries for a visibility threshold of 1 mm (upper), visibility thresholds of 0.5 mm, 1.0 mm and 1.5 mm (middle) and for three different values of Murray's coefficient (lower).

6.3 EFFECT OF INVISIBLE BRANCHES ON CT_{FFR}

6.3.1 EXPERIMENTAL SETUP

In this experiment, we investigate the expected error in CT_{FFR} due to the presence of invisible branches. The analysis is based on the coronary network from Kassab et al. [29] with clinically relevant a 75% area stenosis in varying positions. Barring the stenoses, the parameters of the CT_{FFR} model are the same as the mean values used in Chapter 4 and Chapter 5. The effect of invisible outlets on CT_{FFR} is quantified by comparing the estimated CT_{FFR} for a model with full visibility to a model with a clinically relevant visibility threshold of 1 mm. This analysis is performed for nine different coronary networks, which each has a uniquely positioned stenosis. Three of the networks have a stenosis in

the RCA, three have a stenosis in the LAD, and three have a stenosis in the CX. For each main coronary artery, the stenoses are allocated in the proximal-, medial- and distal regions.

6.3.2 RESULTS

The effect of invisible branches on CT_{FFR} for three different coronary networks is shown in Figure 6.3.1. The results suggest that invisible branches could have a significant effect on CT_{FFR} . Further, the effect of invisible branches could both increase or decrease the CT_{FFR} value, depending on the position of the stenosis and nature of the invisible flow outlets.

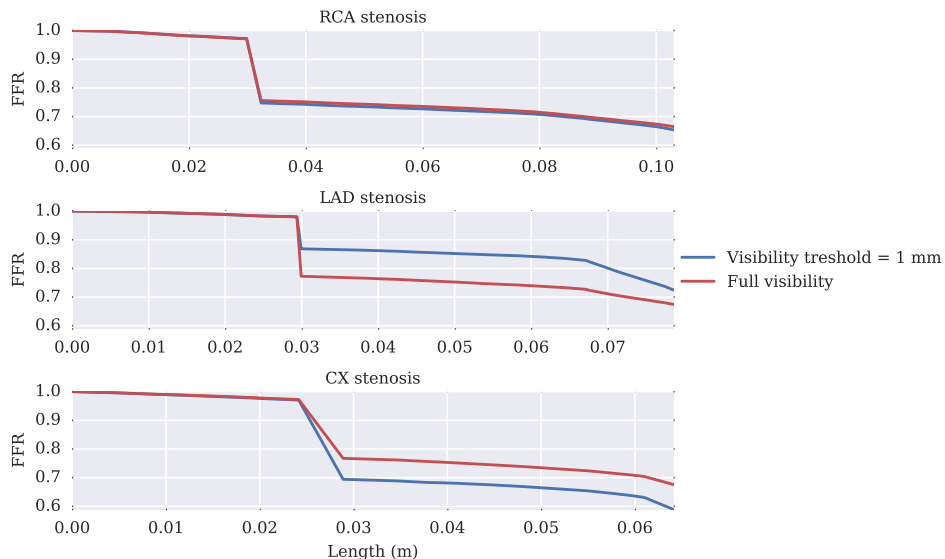


Figure 6.3.1: CT_{FFR} for a 75% area stenosis in one of the following locations: RCA (upper), LAD (middle) and CX (lower). The experiment is performed with full visibility and a visibility threshold of 1 mm.

Quantitative results for the effect of invisible branches on CT_{FFR} is shown in Table 6.3.1. We see that the expected error in CT_{FFR} due to invisible branches is rapidly increasing for increasing visibility thresholds. In particular, the error for the clinically relevant visibility threshold of 1 mm is a mean absolute error of

0.0507 and a mean-squared error of 0.003893.

Visibility threshold	MAE	MSE
0.5 mm	0.0134	0.000553
1 mm	0.0507	0.003893
1.5 mm	0.1207	0.018116

Table 6.3.1: Effect of visibility threshold on Mean Absolute Error (MAE) and Mean Squared Error (MSE) of CT_{FFR} . In this analysis, the expected error from invisible outlets are investigated for nine different coronary networks, each with a uniquely positioned stenosis. The error is calculated from the CT_{FFR} values immediately downstream of the stenosis.

6.4 EFFECT OF LEAKY VESSEL MODEL ON CT_{FFR}

6.4.1 EXPERIMENTAL SETUP

In this experiment, we investigate the performance of the LVM. For this purpose, we compare the expected error in CT_{FFR} using the LVM and the conventional method without correction for flow loss to invisible arteries. The models are compared using the same coronary networks as in Section 6.3. In other words, we compare the methods for nine coronary networks, each with a stenosis in a unique position. The comparison of the models is made for the clinically relevant visibility threshold of 1.0 mm.

6.4.2 RESULTS

Figure 6.4.1 shows the estimated CT_{FFR} for a model with full visibility, a conventional model with limited visibility, and the LVM for three different coronary networks. Here, we see that the newly introduced LVM improves the estimates of CT_{FFR} and closely resembles the CT_{FFR} estimates obtained under full visibility. In contrast, the conventional method with limited visibility results in a

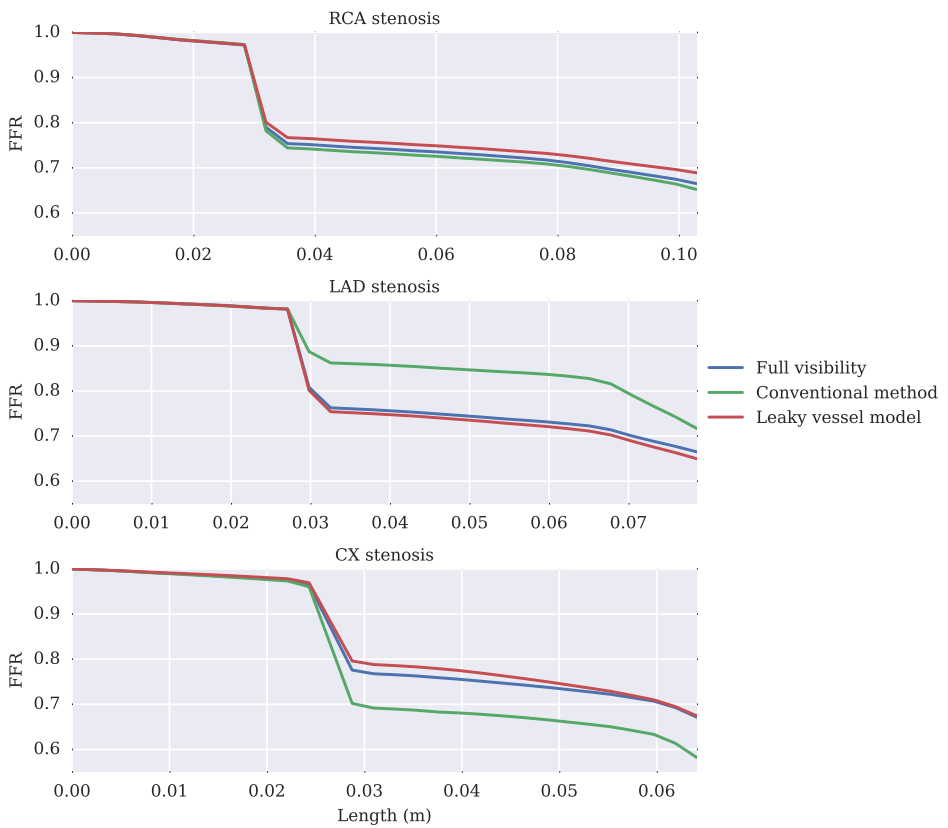


Figure 6.4.1: CT_{FFR} for a 75% area stenosis in one of the following locations: RCA (upper), LAD (middle) and CX (lower). The figure shows the model with full visibility (blue) and the two models with limited visibility: the conventional method (green) and the LVM (red).

Method	MAE	MSE
Conventional Method	0.0507	0.003894
Leaky Vessel Model	0.0208	0.000702

Table 6.4.1: Mean Absolute Error (MAE) and Mean Squared Error (MSE) of CT_{FFR} for the conventional method and the LVM. In this analysis, the expected error from invisible outlets is investigated for nine different coronary networks, each with a uniquely positioned stenosis.

significant discrepancy between the estimated CT_{FFR} for different visibility thresholds.

The results from the quantitative investigation of the performance of the conventional method and the LVM is shown in Table 6.4.1. The table indicates that the LVM significantly reduces the CT_{FFR} error due to invisible branches. In fact, MAE shows a reduction from 0.0507 with the conventional model to 0.0208, corresponding to an error reduction of $\approx 60\%$.

6.5 DISCUSSION

In this chapter, we investigate the influence of CTA-invisible coronary arteries on CT_{FFR} . The problem is investigated using the CT_{FFR} model introduced in Chapter 2. In this work, we find that only a small number of coronary arteries are expected to be visible on CTA. As a result, our analysis shows that a substantial amount of the coronary blood flow is lost to invisible arteries. In fact, we estimate that up to 50% of the blood flow is lost to invisible arteries with a visibility threshold of 1 mm. Further, we compare CT_{FFR} estimates for coronary networks with full visibility to coronary networks with clinically relevant visibility thresholds. The results show that invisible arteries may have a significant effect on CT_{FFR} . In fact, the quantitative investigation shows an expected mean absolute error of CT_{FFR} , $MAE = 0.0507$ for a visibility threshold of 1 mm. This corresponds to a mean error of $\pm 6.3\%$ ($\pm 0.0507/0.8$) for a stenosis at the clinical threshold ($FFR = 0.8$). In other words, the expected error is highly

relevant for clinical applications of CT_{FFR} .

To reduce the error from invisible arteries, we propose a new mathematical model, referred to as the LVM. To our knowledge, this is the first model that incorporates the effect of invisible arteries on CT_{FFR} . The LVM is based on principles of Murray's law and incorporates a leakage term that is shown to significantly reduce the error due to invisible arteries. For a visibility threshold of 1 mm, our quantitative analysis indicates that the LVM reduced the expected model error by $\approx 60\%$.

Note that the coronary geometry from Kassab et al. [29] only incorporates vessels with a diameter above approximately 0.1 mm. It is reasonable to assume that a significant number of smaller coronary arteries exists so that the effect of invisible arteries on CT_{FFR} may be even larger than what we have exhibited in our investigations. Therefore, we believe that better understanding of the effect of invisible vessels is paramount for the future of CT_{FFR} . Also, our analysis shows that the expected flow fraction to invisible branches may be significantly reduced with a decreasing visibility threshold. Accordingly, increasing the resolution of CTA is another direction one might take to improve the accuracy of CT_{FFR} , preferably in combination with a model to account for the effect of invisible arteries.

I'm never going to be in danger of getting the Nobel Prize for literature.

David Eddings

7

Discussion

7.1 SUMMARY

The aim of this thesis is to quantify and reduce the uncertainty of CT_{FFR} . In particular, we focus on uncertainties from the interaction between CFD and the coronary physiology. Our findings suggest several ways to improve the interaction between physiology and fluid dynamics to reduce the uncertainty in CT_{FFR} estimates.

First, we investigate the effect of uncertainty of physiological input parameters on CT_{FFR} . Our results show that moderate uncertainty in physiological input parameters can lead to rather dramatic uncertainties in estimated FFR, which could have a significant impact on clinical decisions. For the CT_{FFR} model, the most influential physiological parameters were found to be cardiac output and myocardial vasodilatory response, TCRI. Also, we compare the expected

uncertainty in CT_{FFR} due to uncertainty in physiological parameters to the uncertainty from lumen segmentation. Despite the approximate nature of this comparison, we find that the uncertainty of lumen segmentation has the greatest effect on CT_{FFR} . However, the uncertainty from lumen segmentation is only slightly higher than the uncertainty from physiological input parameters.

Based on the results of the uncertainty analysis, we propose methods to decrease the uncertainty of CT_{FFR} . One way to approach this is by using additional clinical measurements. For example, cardiac output, myocardial flow fraction, and hematocrit could be measured non-invasively with current clinical tools. Our analysis shows that reducing the uncertainty of the measurable physiological parameters can have a significant effect on CT_{FFR} uncertainty. Also, the uncertainty in these parameters could potentially be reduced by other means, for example with higher accuracy of population-based statistics or by better mathematical modeling.

Terminal outlet resistances and flow distribution in CT_{FFR} models are typically determined using Murray's law. In this thesis, we analyze Murray's law using the published dataset of coronary artery geometry from Kassab et al. [29]. We find that the relationship between vessel radii in the coronary system can be successfully modeled by a power law relationship like Murray's law. Also, we find that relative resistances determined from Murray's law are heavily influenced by geometric uncertainty. In contrast, the uncertainty in Murray's coefficient has a lower influence on the terminal resistance uncertainty. Further, we evaluate the effect of uncertainty in terminal resistances on CT_{FFR} , and find that larger vessels and vessels downstream from the stenosis are of greater importance to the resulting estimate. This finding could prove valuable for clinical applications of CT_{FFR} where CTA image data has variable quality. Thus, a proper description of post-stenotic outlets is necessary for an accurate CT_{FFR} estimate. On the other hand, uncertainties in pre-stenotic regions and parallel vessels are of less importance to CT_{FFR} .

Also, we investigate the influence of CTA-invisible coronary arteries on CT_{FFR} . Here, we find that only a small number of coronary arteries are expected to be

visible on CTA and that the invisible arteries may have a significant effect on CT_{FFR} . To reduce the error from invisible arteries, we propose a new mathematical model, referred to as the LVM. The LVM is based on principles of Murray's law and incorporates a leakage term that is shown to significantly reduce the error due to invisible arteries.

7.2 SUGGESTIONS FOR FUTURE WORK

In this thesis, we have highlighted several challenges in current applications of CT_{FFR} . In particular, we have highlighted challenges in the cross-section between physiology and CFD. In this section, we will present suggestions for future work and areas which we believe have a promising potential for future development of CT_{FFR} .

7.2.1 IMPROVED ANALYSIS USING 3D-CFD MODELS

Even though lumped-parameter models for solving fluid dynamics are well supported, they are not always able to accurately capture the complex characteristics of coronary flow. For this reason, 3D-CFD solvers or hybrid models¹ remain the gold-standard for clinical applications of CT_{FFR} . Therefore, a major assumption in this thesis is that methods to quantify and reduce the uncertainty in lumped-parameter models are relevant for clinical CT_{FFR} algorithms.

Thus, an important task for future work is to test the validity of this assumption. This could be done by performing similar experiments on full 3D-CFD models of CT_{FFR} . Due to the high computational demand of QA and SA, this would require significant computational resources, but could be feasible with a combination of clever algorithms for UQ and SA and the latest technology in high-performance computing.

¹Hybrid model: A combination of CFD solvers of different dimensions, e.g. 0D (lumped) and 3D

7.2.2 MACHINE LEARNING AND BIG DATA

In this work, we present promising results for the use of machine-learning methods for variance-based SA. As pointed out in the thesis, this is an experimental approach that could have tremendous potential for future applications. The substantial increase in computational power over the last years opens up new and exciting possibilities and enables computers to tackle computational problems in higher and higher dimensions. A challenge for classical SA is that many of the most developed and influential methods have poor dimensional scaling and therefore have limited applicability for this new class of SA problems. Thus, efforts to improve current methods and introduce new approaches for SA is paramount to future high-dimensional applications of SA.

Also, machine learning and big data could play a promising role in the development of more accurate physiological input parameters and physiological models for CT_{FFR} applications. The growing commercial and academic interest in the field of CT_{FFR} increases the available datasets and opens up new and promising applications for machine learning and big data.

7.2.3 MYOCARDIAL VIABILITY

A promising area for future research is the concept of myocardial viability. It is likely that the degree of myocardial viability has a significant effect on boundary conditions for CT_{FFR} . It is already well known that only patients with confirmed myocardial viability will benefit from revascularization procedures, and that the amount of viable myocardium evaluated before the procedure is the best indicator of long-term cardiac event-free survival after a cardiac intervention [143–147].

There exist several well-supported clinical imaging techniques for assessment of myocardial viability. Traditional imaging techniques include nuclear imaging by ^{18}F -fluorodeoxyglucose positron emission tomography (PET), nuclear imaging by single-photon emission computed tomography (SPECT), echocardiography with dobutamine, echocardiography with intravenous contrast

agents, magnetic resonance imaging (MRI) with dobutamine or intravenous contrast agents, and CT with intravenous contrast agents [143–155]. For a further description of these methods, we recommend the article *Multimodality Imaging for Assessment of Myocardial Viability: Nuclear, Echocardiography, MR, and CT* by Arrighi and Dilsizian [150].

The assessment of viable myocardium from cardiac CT is particularly interesting to CT_{FFR} and a combined assessment of viable myocardium and CT_{FFR} has a great potential in clinical applications. Currently, assessment of myocardial viability with cardiac CT is mostly investigational, but the results from initial studies are promising [143, 150, 151]. Further work could include investigations of the use of cardiac CT to assess myocardial viability and how to use the measured myocardial viability to increase the accuracy of CT_{FFR} .

7.2.4 IMPROVE LEAKY VESSEL MODELS

To our knowledge, the LVM proposed in this thesis is the first mathematical model that aims to model the effect of CTA-invisible coronary arteries on CT_{FFR} . Thus, it is important to stress that this model is based on simple principles and that there exists a significant potential to increase the accuracy of this model further. Important factors in this development could be more available data and an improved understanding of the presence of invisible arteries in the myocardium.

7.2.5 OTHER METHODS

In the future work presented in this section, we have focused on methods and areas related to the physiological model and physiological input parameters for CT_{FFR} . Thus, other areas for future development of CT_{FFR} exists. Based on our findings, the most critical of these areas is vessel segmentation from CTA. As a result, a continued effort to increase the accuracy of segmentation algorithms should be of utmost importance. On another note, it is likely that improvements in specific fluid-dynamical modeling of the coronary system could have a significant potential to improve the accuracy of CT_{FFR} , e.g. multi-phase flow in

stenosed areas.

References

- [1] Nathan D Wong. Epidemiological studies of chd and the evolution of preventive cardiology. *Nature Reviews Cardiology*, 11(5):276–289, 2014.
- [2] Peter A McCullough. Coronary artery disease. *Clinical Journal of the American Society of Nephrology*, 2(3):611–616, 2007.
- [3] Paul A Heidenreich, Justin G Trogdon, Olga A Khavjou, Javed Butler, Kathleen Dracup, Michael D Ezekowitz, Eric Andrew Finkelstein, Yuling Hong, S Claiborne Johnston, Amit Khera, et al. Forecasting the future of cardiovascular disease in the united states a policy statement from the american heart association. *Circulation*, 123(8):933–944, 2011.
- [4] Takeshi Kimura, Hiroki Shiomi, Sachio Kurabayashi, Takaaki Isshiki, Susumu Kanazawa, Hiroshi Ito, Shunya Ikeda, Ben Forrest, Christopher K Zarins, Mark A Hlatky, et al. Cost analysis of non-invasive fractional flow reserve derived from coronary computed tomographic angiography in japan. *Cardiovascular intervention and therapeutics*, 30(1):38–44, 2014.
- [5] Wikimedia Commons. Coronary circulation, 2010.
- [6] Wikimedia Commons. Coronary artery disease, 2013.
- [7] Fabian Plank, Guy Friedrich, Wolfgang Dichtl, Andrea Klauser, Werner Jaschke, Wolfgang-Michael Franz, and Gudrun Feuchtner. The diagnostic and prognostic value of coronary ct angiography in asymptomatic high-risk patients: a cohort study. *Open Heart*, 1(1):e000096, 2014.
- [8] Steven E Nissen. Limitations of computed tomography coronary angiography. *Journal of the American College of Cardiology*, 52(25):2145–2147, 2008.

- [9] Nico H.J. Pijls, Bernard de Bruyne, Kathinka Peels, Pepijn H. van der Voort, Hans J.R.M. Bonnier, Jozef Bartunek, and Jacques J. Koolen. Measurement of fractional flow reserve to assess the functional severity of coronary-artery stenoses. *New England Journal of Medicine*, 334(26):1703–1708, 1996. PMID: 8637515.
- [10] NH Pijls, JA Van Son, RL Kirkeeide, BLGK De Bruyne, and KL Gould. Experimental basis of determining maximum coronary, myocardial, and collateral blood flow by pressure measurements for assessing functional stenosis severity before and after percutaneous transluminal coronary angioplasty. *Circulation*, 87(4):1354–1367, 1993.
- [11] Miguel Borges Santos, António Miguel Ferreira, Pedro de Araújo Goncalves, Luís Raposo, Rui Campante Teles, Manuel Almeida, and Miguel Mendes. Diagnostic yield of current referral strategies for elective coronary angiography in suspected coronary artery disease—an analysis of the across registry. *Revista Portuguesa de Cardiologia (English Edition)*, 32(6):483–488, 2013.
- [12] Charles A Taylor, Timothy A Fonte, and James K Min. Computational fluid dynamics applied to cardiac computed tomography for noninvasive quantification of fractional flow reserve: scientific basis. *Journal of the American College of Cardiology*, 61(22):2233–2241, 2013.
- [13] Shun Kohsaka and Amgad N Makaryus. Coronary angiography using noninvasive imaging techniques of cardiac ct and mri. *Current cardiology reviews*, 4(4):323, 2008.
- [14] Byoung-Kwon Lee. Computational fluid dynamics in cardiovascular disease. *Korean circulation journal*, 41(8):423–430, 2011.
- [15] Mark A Hlatky, Bernard De Bruyne, Gianluca Pontone, Manesh R Patel, Bjarne L Norgaard, Robert A Byrne, Nick Curzen, Ian Purcell, Matthias Gutberlet, Gilles Rioufol, et al. Quality-of-life and economic outcomes of assessing fractional flow reserve with computed tomography angiography: Platform. *Journal of the American College of Cardiology*, 66(21):2315–2323, 2015.
- [16] James K Min, Daniel S Berman, Matthew J Budoff, Farouc A Jaffer, Jonathon Leipsic, Martin B Leon, GB John Mancini, Laura Mauri, Robert S Schwartz, and Leslee J Shaw. Rationale and design of the defacto

(determination of fractional flow reserve by anatomic computed tomographic angiography) study. *Journal of cardiovascular computed tomography*, 5(5):301–309, 2011.

- [17] Bon-Kwon Koo, Andrejs Erglis, Joon-Hyung Doh, David V Daniels, Sandra Jegere, Hyo-Soo Kim, Allison Dunning, Tony DeFrance, Alexandra Lansky, Jonathan Leipsic, et al. Diagnosis of ischemia-causing coronary stenoses by noninvasive fractional flow reserve computed from coronary computed tomographic angiograms: results from the prospective multicenter discover-flow (diagnosis of ischemia-causing stenoses obtained via noninvasive fractional flow reserve) study. *Journal of the American College of Cardiology*, 58(19):1989–1997, 2011.
- [18] Sethuraman Sankaran, Leo J Grady, and Charles A Taylor. Real-time sensitivity analysis of blood flow simulations to lumen segmentation uncertainty. In *Medical Image Computing and Computer-Assisted Intervention–MICCAI 2014*, pages 1–8. Springer, 2014.
- [19] Sethuraman Sankaran, Leo Grady, and Charles A Taylor. Fast computation of hemodynamic sensitivity to lumen segmentation uncertainty. *Medical Imaging, IEEE Transactions on*, 34(12):2562–2571, 2015.
- [20] Sethuraman Sankaran, Hyun Jin Kim, Gilwoo Choi, and Charles A Taylor. Uncertainty quantification in coronary blood flow simulations: impact of geometry, boundary conditions and blood viscosity. *Journal of Biomechanics*, 2016.
- [21] Taha Sochi. Fluid flow at branching junctions. *International Journal of Fluid Mechanics Research*, 42(1), 2015.
- [22] Cecil D Murray. The physiological principle of minimum work i. the vascular system and the cost of blood volume. *Proceedings of the National Academy of Sciences*, 12(3):207–214, 1926.
- [23] Cecil D Murray. The physiological principle of minimum work ii. oxygen exchange in capillaries. *Proceedings of the National Academy of Sciences*, 12(5):299–304, 1926.
- [24] Adriaan Coenen, Marisa M Lubbers, Akira Kurata, Atsushi Kono, Admir Dedic, Raluca G Chelu, Marcel L Dijkshoorn, Frank J Gijsen, Mohamed

Ouhlous, Robert-Jan M van Geuns, et al. Fractional flow reserve computed from noninvasive ct angiography data: diagnostic performance of an on-site clinician-operated computational fluid dynamics algorithm. *Radiology*, 274(3):674–683, 2014.

- [25] Jun-Mei Zhang, Liang Zhong, Tong Luo, Yunlong Huo, Swee Yaw Tan, Aaron Sung Lung Wong, Boyang Su, Min Wan, Xiaodan Zhao, Ghassan S Kassab, et al. Numerical simulation and clinical implications of stenosis in coronary blood flow. *BioMed research international*, 2014, 2014.
- [26] Johannes V Soulis, Thomas M Farmakis, George D Giannoglou, and George E Louridas. Wall shear stress in normal left coronary artery tree. *Journal of Biomechanics*, 39(4):742–749, 2006.
- [27] Lucian Mihai Itu, Puneet Sharma, Xudong Zheng, Ali Kamen, Constantin Suciu, and Dorin Comaniciu. Framework for personalization of coronary flow computations during rest and hyperemia, March 13 2013. US Patent App. 14/384,547.
- [28] U Joseph Schoepf. *Coronary Artery Disease and the Myocardial Ischemic Cascade, An Issue of Radiologic Clinics of North America*, volume 53. Elsevier Health Sciences, 2015.
- [29] Ghassan S Kassab, Carmela A Rider, Nina J Tang, and Yuan-Cheng Fung. Morphometry of pig coronary arterial trees. *American Journal of Physiology-Heart and Circulatory Physiology*, 265(1):H350–H365, 1993.
- [30] M Freiman, Y Lamash, G Gilboa, H Nickisch, S Prevrhal, H Schmitt, M Vembar, and L Goshen. Automatic coronary lumen segmentation with partial volume modeling improves lesions' hemodynamic significance assessment. In *SPIE Medical Imaging*, pages 978403–978403. International Society for Optics and Photonics, 2016.
- [31] Thomas Kenner. *Cardiovascular System Dynamics: Models and Measurements*. Springer, 2013.
- [32] Carlos Moreno and Kiran Bhaganagar. Modeling of stenotic coronary artery and implications of plaque morphology on blood flow. *Modelling and Simulation in Engineering*, 2013:14, 2013.

- [33] Damien Garcia, Paolo G Camici, Louis-Gilles Durand, Kim Rajappan, Emmanuel Gaillard, Ornella E Rimoldi, and Philippe Pibarot. Impairment of coronary flow reserve in aortic stenosis. *Journal of Applied Physiology*, 106(1):113–121, 2009.
- [34] Markus Ferrari, Gerald S Werner, Philipp Bahrmann, Barbara M Richartz, and Hans R Figulla. Turbulent flow as a cause for underestimating coronary flow reserve measured by doppler guide wire. *Cardiovascular ultrasound*, 4(1):14, 2006.
- [35] RA Cassanova and DP Giddens. Disorder distal to modeled stenoses in steady and pulsatile flow. *Journal of biomechanics*, 11(10):441–453, 1978.
- [36] Taha Sochi. Non-newtonian rheology in blood circulation. *arXiv preprint arXiv:1306.2067*, 2013.
- [37] Walter F Boron and Emile L Boulpaep. *Medical Physiology, 2e Updated Edition: with STUDENT CONSULT Online Access*. Elsevier Health Sciences, 2012.
- [38] Barbara M Johnston, Peter R Johnston, Stuart Corney, and David Kilpatrick. Non-newtonian blood flow in human right coronary arteries: steady state simulations. *Journal of biomechanics*, 37(5):709–720, 2004.
- [39] K Haldar. Effects of the shape of stenosis on the resistance to blood flow through an artery. *Bulletin of mathematical biology*, 47(4):545–550, 1985.
- [40] Gan Chen, Lian Zhao, YaoWen Liu, FuLong Liao, Dong Han, and Hong Zhou. Regulation of blood viscosity in disease prevention and treatment. *Chinese Science Bulletin*, 57(16):1946–1952, 2012.
- [41] Ryo Torii, Nigel B Wood, Nearchos Hadjiloizou, Andrew W Dowsey, Andrew R Wright, Alun D Hughes, Justin Davies, Darrel P Francis, Jamil Mayet, Guang-Zhong Yang, et al. Fluid–structure interaction analysis of a patient-specific right coronary artery with physiological velocity and pressure waveforms. *Communications in numerical methods in engineering*, 25(5):565–580, 2009.
- [42] Dehong Zeng, Evangelos Boutsianis, Marc Ammann, Kevin Boomsma, Simon Wildermuth, and Dimos Poulikakos. A study on the compliance of a right coronary artery and its impact on wall shear stress. *Journal of biomechanical engineering*, 130(4):041014, 2008.

- [43] Ernst Wellnhofer, Jan Osman, Ulrich Kertzscher, Klaus Affeld, Eckart Fleck, and Leonid Goubergrits. Flow simulation studies in coronary arteries—impact of side-branches. *Atherosclerosis*, 213(2):475–481, 2010.
- [44] Yunlong Huo, Mark Svendsen, Jenny Susana Choy, Z-D Zhang, and Ghassan S Kassab. A validated predictive model of coronary fractional flow reserve. *Journal of The Royal Society Interface*, 9(71):1325–1338, 2012.
- [45] HG Cuming. *The secondary flow in curved pipes*. HM Stationery Office, 1955.
- [46] Liza Shrestha. Cfd study on effect of branch sizes in human coronary artery. Master’s thesis, University of Iowa, 2010.
- [47] Xiaofei Wang. *1D modeling of blood flow in networks: numerical computing and applications*. PhD thesis, Université Pierre et Marie Curie-Paris VI, 2014.
- [48] Mårten T Landahl and E Mollo-Christensen. *Turbulence and random processes in fluid mechanics*. Cambridge University Press, 1992.
- [49] Sally Epstein, Marie Willemet, Phil J Chowienczyk, and Jordi Alastrauey. Reducing the number of parameters in 1d arterial blood flow modeling: less is more for patient-specific simulations. *American Journal of Physiology-Heart and Circulatory Physiology*, 309(1):H222–H234, 2015.
- [50] Yubing Shi, Patricia Lawford, Rodney Hose, et al. Review of zero-d and 1-d models of blood flow in the cardiovascular system. *Biomed. Eng. Online*, 10(1):33, 2011.
- [51] Arjen van der Horst, Frits L Boogaard, Marcel van’t Veer, Marcel Rutten, Nico HJ Pijls, and Frans N van de Vosse. Towards patient-specific modeling of coronary hemodynamics in healthy and diseased state. *Computational and mathematical methods in medicine*, 2013, 2013.
- [52] Nico Westerhof, Jan-Willem Lankhaar, and Berend E Westerhof. The arterial windkessel. *Medical & biological engineering & computing*, 47(2):131–141, 2009.

- [53] Yifang Zhou, Ghassan S Kassab, and Sabee Molloi. On the design of the coronary arterial tree: a generalization of murray's law. *Physics in medicine and biology*, 44(12):2929, 1999.
- [54] Donald F Young and Frank Y Tsai. Flow characteristics in models of arterial stenoses—i. steady flow. *Journal of biomechanics*, 6(4):395–410, 1973.
- [55] Donald F Young and Frank Y Tsai. Flow characteristics in models of arterial stenoses—ii. unsteady flow. *Journal of biomechanics*, 6(5):547–559, 1973.
- [56] Daisy Sahni, GD Kaur, Harjeet Jit, and Indar Jit. Anatomy & distribution of coronary arteries in pig in comparison with man. *Indian Journal of Medical Research*, 127(6):564, 2008.
- [57] Mahdi Mazinani, SD Qanadli, Rahil Hosseini, Tim Ellis, and Jamshid Dehmehki. A 3d approach for extraction of the coronary artery and quantification of the stenosis. *World Academy of Science, Engineering and Technology*, 59, 2011.
- [58] Bogdan Ene Iordache and Andrea Remuzzi. Numerical analysis of blood flow in reconstructed glomerular capillary segments. *Microvascular research*, 49(1):1–11, 1995.
- [59] AR Pries, TW Secomb, and P Gaehtgens. Biophysical aspects of blood flow in the microvasculature. *Cardiovascular research*, 32(4):654–667, 1996.
- [60] RF Wilson, K Wyche, BV Christensen, S Zimmer, and DD Laxson. Effects of adenosine on human coronary arterial circulation. *Circulation*, 82(5):1595–1606, 1990.
- [61] Heinrich R Schelbert. Ffr and coronary flow reserve: friends or foes? *JACC: Cardiovascular Imaging*, 5(2):203–206, 2012.
- [62] Eric Jones, Travis Oliphant, Pearu Peterson, et al. SciPy: Open source scientific tools for Python, 2001–. [Online; accessed 2016-05-14].
- [63] Jorge J Moré, Burton S Garbow, and Kenneth E Hillstrom. User guide for minpack-1. Technical report, CM-Pooo68642, 1980.

- [64] Michael LaBarbera. Principles of design of fluid transport systems in zoology. *Science*, 249(4972):992–1000, 1990.
- [65] W Jegier, P Sekelj, HT Davenport, and M McGregor. Cardiac output and related hemodynamic data in normal children and adults. *Canadian journal of biochemistry and physiology*, 39(11):1747–1753, 1961.
- [66] Howard D Sesso, Meir J Stampfer, Bernard Rosner, Charles H Hennekens, J Michael Gaziano, JoAnn E Manson, and Robert J Glynn. Systolic and diastolic blood pressure, pulse pressure, and mean arterial pressure as predictors of cardiovascular disease risk in men. *Hypertension*, 36(5):801–807, 2000.
- [67] Kevin Wei and Sanjiv Kaul. The coronary microcirculation in health and disease. *Cardiology clinics*, 22(2):221–231, 2004.
- [68] N.H. Pijls and B. de Bruyne. *Coronary Pressure*. Developments in Cardiovascular Medicine. Springer Netherlands, 2013.
- [69] AL McGinn, CW White, and RF Wilson. Interstudy variability of coronary flow reserve. influence of heart rate, arterial pressure, and ventricular preload. *Circulation*, 81(4):1319–1330, 1990.
- [70] James K Min, Jonathon Leipsic, Michael J Pencina, Daniel S Berman, Bon-Kwon Koo, Carlos van Mieghem, Andrejs Erglis, Fay Y Lin, Allison M Dunning, Patricia Apruzzese, et al. Diagnostic accuracy of fractional flow reserve from anatomic ct angiography. *Jama*, 308(12):1237–1245, 2012.
- [71] H Hinghofer-Szalkay and JE Greenleaf. Continuous monitoring of blood volume changes in humans. *Journal of Applied Physiology*, 63(3):1003–1007, 1987.
- [72] Ralph C Smith. *Uncertainty quantification: theory, implementation, and applications*, volume 12. SIAM, 2013.
- [73] Jonathan Feinberg and Hans Petter Langtangen. Chaospy: An open source tool for designing methods of uncertainty quantification. *Journal of Computational Science*, 11:46–57, 2015.
- [74] Vinzenz Gregor Eck, Wouter Paulus Donders, Jacob Sturdy, Jonathan Feinberg, Tammo Delhaas, Leif Rune Hellevik, and Wouter Huberts. A

guide to uncertainty quantification and sensitivity analysis for cardiovascular applications. *International journal for numerical methods in biomedical engineering*, 2015.

- [75] Sang Hoon Lee and Wei Chen. A comparative study of uncertainty propagation methods for black-box-type problems. *Structural and Multidisciplinary Optimization*, 37(3):239–253, 2009.
- [76] Zhendan Xue, Mariapia Marchi, Sumeet Parashar, and Guosong Li. Comparing uncertainty quantification with polynomial chaos and metamodel-based strategies for computationally expensive cae simulations and optimization applications. Technical report, SAE Technical Paper, 2015.
- [77] Ali Mohammad-Djafari. From deterministic to probabilistic approaches to solve inverse problems. In *SPIE's International Symposium on Optical Science, Engineering, and Instrumentation*, pages 2–11. International Society for Optics and Photonics, 1998.
- [78] Joseph B. Nagel and Bruno Sudret. A unified framework for multilevel uncertainty quantification in bayesian inverse problems. *Probabilistic Engineering Mechanics*, 43:68 – 84, 2016.
- [79] Andrea Saltelli, Karen Chan, E Marian Scott, et al. *Sensitivity analysis*, volume 1. Wiley New York, 2000.
- [80] Bruno Sudret. Global sensitivity analysis using polynomial chaos expansions. *Reliability Engineering & System Safety*, 93(7):964–979, 2008.
- [81] Bertrand Iooss and Paul Lemaître. A review on global sensitivity analysis methods. In *Uncertainty Management in Simulation-Optimization of Complex Systems*, pages 101–122. Springer, 2015.
- [82] Patrick Billingsley. *Probability and measure*. John Wiley & Sons, 2008.
- [83] Warren Gilchrist. *Statistical modelling with quantile functions*. CRC Press, 2000.
- [84] Dongbin Xiu. *Numerical methods for stochastic computations: a spectral method approach*. Princeton University Press, 2010.

- [85] Juan M Morales, Antonio J Conejo, Henrik Madsen, Pierre Pinson, and Marco Zugno. *Integrating renewables in electricity markets: Operational problems*, volume 205. Springer Science & Business Media, 2013.
- [86] Ilya M Sobol. Global sensitivity indices for nonlinear mathematical models and their monte carlo estimates. *Mathematics and computers in simulation*, 55(1):271–280, 2001.
- [87] Toshimitsu Homma and Andrea Saltelli. Importance measures in global sensitivity analysis of nonlinear models. *Reliability Engineering & System Safety*, 52(1):1–17, 1996.
- [88] Michael D McKay, Richard J Beckman, and William J Conover. A comparison of three methods for selecting values of input variables in the analysis of output from a computer code. *Technometrics*, 42(1):55–61, 2000.
- [89] Il'ya Meerovich Sobol'. On the distribution of points in a cube and the approximate evaluation of integrals. *Zhurnal Vychislitel'noi Matematiki i Matematicheskoi Fiziki*, 7(4):784–802, 1967.
- [90] John H Halton. Algorithm 247: Radical-inverse quasi-random point sequence. *Communications of the ACM*, 7(12):701–702, 1964.
- [91] George Fishman. *Monte Carlo: concepts, algorithms, and applications*. Springer Science & Business Media, 2013.
- [92] Russel E Caflisch. Monte carlo and quasi-monte carlo methods. *Acta numerica*, 7:1–49, 1998.
- [93] Andrea Saltelli. Making best use of model evaluations to compute sensitivity indices. *Computer Physics Communications*, 145(2):280–297, 2002.
- [94] Norbert Wiener. The homogeneous chaos. *American Journal of Mathematics*, 60(4):897–936, 1938.
- [95] Gaurav Kewlani, Justin Crawford, and Karl Iagnemma. A polynomial chaos approach to the analysis of vehicle dynamics under uncertainty. *Vehicle System Dynamics*, 50(5):749–774, 2012.

- [96] Dongbin Xiu and George Em Karniadakis. The wiener–askey polynomial chaos for stochastic differential equations. *SIAM journal on scientific computing*, 24(2):619–644, 2002.
- [97] Thierry Crestaux, Olivier Le Maître, and Jean-Marc Martinez. Polynomial chaos expansion for sensitivity analysis. *Reliability Engineering & System Safety*, 94(7):1161–1172, 2009.
- [98] Sergey A Smolyak. Quadrature and interpolation formulas for tensor products of certain classes of functions. In *Dokl. Akad. Nauk SSSR*, volume 4, page 123, 1963.
- [99] L Le Gratiet, S. Marelli, and B. Sudret. *Metamodel-based sensitivity analysis: polynomial chaos expansions and Gaussian processes*. Springer, 2016.
- [100] Shuang Li, Bin Yang, and Fei Qi. Accelerate global sensitivity analysis using artificial neural network algorithm: Case studies for combustion kinetic model. *Combustion and Flame*, 168:53–64, 2016.
- [101] Hemalatha Sathyaranayananurthy and Ratna Babu Chinnam. Metamodels for variable importance decomposition with applications to probabilistic engineering design. *Computers & Industrial Engineering*, 57(3):996–1007, 2009.
- [102] Curtis B Storlie, Laura P Swiler, Jon C Helton, and Cedric J Sallaberry. Implementation and evaluation of nonparametric regression procedures for sensitivity analysis of computationally demanding models. *Reliability Engineering & System Safety*, 94(11):1735–1763, 2009.
- [103] Tin Kam Ho. Random decision forests. In *Document Analysis and Recognition, 1995., Proceedings of the Third International Conference on*, volume 1, pages 278–282. IEEE, 1995.
- [104] Tin Kam Ho. The random subspace method for constructing decision forests. *Pattern Analysis and Machine Intelligence, IEEE Transactions on*, 20(8):832–844, 1998.
- [105] Robi Polikar. Ensemble based systems in decision making. *Circuits and systems magazine, IEEE*, 6(3):21–45, 2006.
- [106] Leo Breiman. Random forests. *Machine learning*, 45(1):5–32, 2001.

- [107] Trevor Hastie, Robert Tibshirani, Jerome Friedman, and James Franklin. The elements of statistical learning: data mining, inference and prediction. *The Mathematical Intelligencer*, 27(2):83–85, 2005.
- [108] Gérard Biau and Erwan Scornet. A random forest guided tour. *arXiv preprint arXiv:1511.05741*, 2015.
- [109] AlpeshKumar Ranchordas, João Madeiras Pereira, Hélder J Araújo, and João Manuel RS Tavares. Computer vision, imaging and computer graphics. 2010.
- [110] Max D Morris. Factorial sampling plans for preliminary computational experiments. *Technometrics*, 33(2):161–174, 1991.
- [111] Francesca Campolongo, Jessica Cariboni, and Andrea Saltelli. An effective screening design for sensitivity analysis of large models. *Environmental modelling & software*, 22(10):1509–1518, 2007.
- [112] Cameron Davidson-Pilon. *Bayesian Methods for Hackers: Probabilistic Programming and Bayesian Inference*. Addison-Wesley Professional, 2015.
- [113] Christopher M Bishop. Pattern recognition. *Machine Learning*, 2006.
- [114] Andrew Gelman et al. Prior distributions for variance parameters in hierarchical models (comment on article by browne and draper). *Bayesian analysis*, 1(3):515–534, 2006.
- [115] Harold Jeffreys. An invariant form for the prior probability in estimation problems. In *Proceedings of the Royal Society of London A: Mathematical, Physical and Engineering Sciences*, volume 186, pages 453–461. The Royal Society, 1946.
- [116] James O Berger and José M Bernardo. On the development of reference priors. *Bayesian statistics*, 4(4):35–60, 1992.
- [117] Solomon Kullback and Richard A Leibler. On information and sufficiency. *The annals of mathematical statistics*, 22(1):79–86, 1951.
- [118] Andrew Gelman, John B Carlin, Hal S Stern, and Donald B Rubin. *Bayesian data analysis*, volume 2. Taylor & Francis, 2014.
- [119] Charles Geyer. Introduction to markov chain monte carlo. *Handbook of Markov Chain Monte Carlo*, pages 3–48, 2011.

- [120] Nicholas Metropolis, Arianna W Rosenbluth, Marshall N Rosenbluth, Augusta H Teller, and Edward Teller. Equation of state calculations by fast computing machines. *The journal of chemical physics*, 21(6):1087–1092, 1953.
- [121] Anand Patil, David Huard, and Christopher J Fonnesbeck. Pymc: Bayesian stochastic modelling in python. *Journal of statistical software*, 35(4):1, 2010.
- [122] CJ Fonnesbeck. Pymc user’s guide. version 2.3.6, 2015.
- [123] Yatin Mehta and Dheeraj Arora. Newer methods of cardiac output monitoring. *World journal of cardiology*, 6(9):1022, 2014.
- [124] Paweł Petkow Dimitrow. Transthoracic doppler echocardiography—noninvasive diagnostic window for coronary flow reserve assessment. *Cardiovascular ultrasound*, 1(1):1, 2003.
- [125] Vivian L Clark and James A Kruse. Clinical methods: the history, physical, and laboratory examinations. *JAMA*, 264(21):2808–2809, 1990.
- [126] Thomas G Pickering, John E Hall, Lawrence J Appel, Bonita E Falkner, John Graves, Martha N Hill, Daniel W Jones, Theodore Kurtz, Sheldon G Sheps, and Edward J Roccella. Recommendations for blood pressure measurement in humans and experimental animals part 1: blood pressure measurement in humans: a statement for professionals from the subcommittee of professional and public education of the american heart association council on high blood pressure research. *Hypertension*, 45(1):142–161, 2005.
- [127] AKIRA Kamiya and TATSUO Togawa. Adaptive regulation of wall shear stress to flow change in the canine carotid artery. *American Journal of Physiology-Heart and Circulatory Physiology*, 239(1):H14–H21, 1980.
- [128] Seymour Glagov, Elliot Weisenberg, Christopher K Zarins, Regina Stankunavicius, and George J Kolettis. Compensatory enlargement of human atherosclerotic coronary arteries. *New England Journal of Medicine*, 316(22):1371–1375, 1987.
- [129] Cecil D Murray. The physiological principle of minimum work: I. the vascular system and the cost of blood volume. *Proceedings of the National Academy of Sciences of the United States of America*, 12(3):207, 1926.

- [130] W Sn Miller. The structure of the lung. *Journal of Morphology*, 8(1):165–188, 1893.
- [131] Hitoshi Fukasawa. Hemodynamical studies of cerebral arteries by means of mathematical analysis of arterial casts. *The Tohoku journal of experimental medicine*, 99(3):255–268, 1969.
- [132] GROVER M Hutchins, MARTIN M Miner, and JOHN K Boitnott. Vessel caliber and branch-angle of human coronary artery branch-points. *Circulation Research*, 38(6):572–576, 1976.
- [133] T Arts, RT Kruger, W Van Gerven, JA Lambregts, and RS Reneman. Propagation velocity and reflection of pressure waves in the canine coronary artery. *American Journal of Physiology-Heart and Circulatory Physiology*, 237(4):H469–H474, 1979.
- [134] Thomas F Sherman. On connecting large vessels to small. the meaning of murray's law. *The Journal of general physiology*, 78(4):431–453, 1981.
- [135] Mark A Changizi and Christopher Cherniak. Modeling the large-scale geometry of human coronary arteries. *Canadian journal of physiology and pharmacology*, 78(8):603–611, 2000.
- [136] Aaron S Wang, David H Liang, Fritz Bech, Jason T Lee, Christopher K Zarins, Wei Zhou, and Charles A Taylor. Validation of a power law model in upper extremity vessels: Potential application in ultrasound bleed detection. *Ultrasound in medicine & biology*, 38(4):692–701, 2012.
- [137] HBM Uylings. Optimization of diameters and bifurcation angles in lung and vascular tree structures. *Bulletin of mathematical biology*, 39(5):509–520, 1977.
- [138] Rémi Revellin, François Rousset, David Baud, and Jocelyn Bonjour. Theoretical biology and medical modelling. *Theoretical Biology and Medical Modelling*, 6:7, 2009.
- [139] John A Nelder and Roger Mead. A simplex method for function minimization. *The computer journal*, 7(4):308–313, 1965.
- [140] Fanny Sarrazin, Francesca Pianosi, and Thorsten Wagener. Global sensitivity analysis of environmental models: Convergence and validation. *Environmental Modelling & Software*, 79:135–152, 2016.

- [141] SD Filardo, M Chan, DP Lee, P Hon, C Kim, A Schwarzkopf, and AC Yeung. Normal coronary arteries do not taper in between branch vessels: an in vivo study. *Journal of the American College of Cardiology*, 31:276–277, 1998.
- [142] Wikimedia Commons. Cast of coronary arteries, 2006.
- [143] Małgorzata Kobylecka, Joanna Mączewska, Katarzyna Fronczewska-Wieniawska, Tomasz Mazurek, Maria Teresa Płazińska, and Leszek Królicki. Myocardial viability assessment in ¹⁸fdg pet/ct study (¹⁸fdg pet myocardial viability assessment). *Nuclear Medicine Review*, 15(1):52–60, 2012.
- [144] Adel Shabana and Ayman El-Menyar. Myocardial viability: what we knew and what is new. *Cardiology research and practice*, 2012, 2012.
- [145] Sara L Partington, Raymond Y Kwong, and Sharmila Dorbala. Multimodality imaging in the assessment of myocardial viability. *Heart failure reviews*, 16(4):381–395, 2011.
- [146] Kevin C Allman, Leslee J Shaw, Rory Hachamovitch, and James E Udelson. Myocardial viability testing and impact of revascularization on prognosis in patients with coronary artery disease and left ventricular dysfunction: a meta-analysis. *Journal of the American College of Cardiology*, 39(7):1151–1158, 2002.
- [147] Paolo G Camici, Sanjay Kumak Prasad, and Ornella E Rimoldi. Stunning, hibernation, and assessment of myocardial viability. *Circulation*, 117(1):103–114, 2008.
- [148] Andreas H Mahnken, Georg Mühlenbruch, Rolf W Günther, and Joachim E Wildberger. Ct imaging of myocardial viability: experimental and clinical evidence. *Cardiovascular journal of Africa*, 18(3):169, 2007.
- [149] MJ Kern. Assessment of myocardial viability: using coronary pressure and flow after acute myocardial infarction. *Heart*, 89(1):9–10, 2003.
- [150] James A Arrighi and Vasken Dilsizian. Multimodality imaging for assessment of myocardial viability: nuclear, echocardiography, mr, and ct. *Current cardiology reports*, 14(2):234–243, 2012.

- [151] Arend FL Schinkel, Don Poldermans, Abdou Elhendy, and Jeroen J Bax. Assessment of myocardial viability in patients with heart failure. *Journal of Nuclear Medicine*, 48(7):1135–1146, 2007.
- [152] Dorinna D Mendoza and Wm Guy Weigold. Evaluation of myocardial viability by multidetector ct. *Journal of cardiovascular computed tomography*, 3(1):S2–S12, 2009.
- [153] Mansour Al Moudi and Zhong-Hua Sun. Diagnostic value of (¹⁸) f-fdg pet in the assessment of myocardial viability in coronary artery disease: A comparative study with (^{99m}) tc spect and echocardiography. *J Geriatr Cardiol*, 11(3):229–36, 2014.
- [154] H Brodoefel, B Klumpp, A Reimann, M Fenchel, M Heuschmid, S Miller, S Schroeder, C Claussen, AM Scheule, and AF Kopp. Sixty-four-msct in the characterization of porcine acute and subacute myocardial infarction: determination of transmurality in comparison to magnetic resonance imaging and histopathology. *European journal of radiology*, 62(2):235–246, 2007.
- [155] Anja Wagner, Heiko Mahrholdt, Thomas A Holly, Michael D Elliott, Matthias Regenfus, Michele Parker, Francis J Klocke, Robert O Bonow, Raymond J Kim, and Robert M Judd. Contrast-enhanced mri and routine single photon emission computed tomography (spect) perfusion imaging for detection of subendocardial myocardial infarcts: an imaging study. *The Lancet*, 361(9355):374–379, 2003.

